Bendix Instruments & Life Support Division



The
Bendix
Corporation

Instruments & Life
Support Division
Davenport, Iowa 52808

# Design, Development And Manufacture of a Breadboard Radio Frequency Mass Gauging System

## VOLUME I

Phase B Final Report

Contract NAS 8-30160

Prepared For

National Aeronautics And Space
Administration
George C. Marshall
Space Flight Center
Huntsville, Alabama

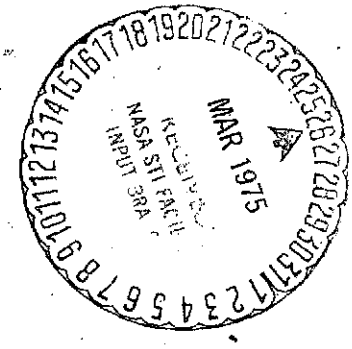


Pub. No. 7246
November 15, 1974
Printed in U.S.A.

Bendix Instruments & Life Support Division

## FOREWORD

This report covers the work performed under Phase B of Contract NAS 8-30160. It reports all RF Gauging work performed by the Instruments & Life Support Division of The Bendix Corporation for the NASA Marshall Space Flight Center during the contract period.

APPROVED:

The Bendix Corporation
Instruments & Life Support Division

Harold E. Thompson

NASA/MSFC

## TABLE OF CONTENTS

## ABSTRACT

The applicability of the RF Mode Counting technique for gauging liquid oxygen and liquid hydrogen under all attitude conditions was demonstrated using a vacuum jacketed test tank mounted on a remotely controlled gimbaling mechanism. In addition, the technique was successfully tested using liquid oxygen in a large NASA test tank as the tank was filled and emptied.

To further substantiate the capabilities of the RF Mode Counting technique as applied to applications involving zero gravity conditions, a test system using benzene as a test fluid was flight tested in a KC-135 test aircraft. This testing involved a number of zero 'G' maneuvers with various quantities of the test fluid.

A series of tests were also performed to evaluate the relative effects of the presence of capillary liquid retention screens on the RF Gauging technique. These tests involved considerations of system Q reductions, RF leakage through retention screens, and surface wetting effects.

## 1.0 INTRODUCTION

The Instruments & Life Support Division of The Bendix Corporation submits herewith Volume I of a two volume report to George C. Marshall Space Flight Center (MSFC) to document the progress made during Phase B of NASA Contract NAS 8-30160 for "Design, Development and Manufacture of a Breadboard Radio Frequency Mass Gauging System". Work performed under Phase A was previously reported in Bendix Pub. No. 4879A-71 dated January 21, 1972.

This volume, Volume I, documents the evaluation of hardware and test programs involving the following areas:

- The interaction of capillary liquid retention screens on the RF gauging technique.
- Zero gravity flight testing in KC-135 aircraft.
- Liquid oxygen loading tests in a large NASA tank (Test Cell 100).
- Liquid oxygen orientation tests in vacuum jacketed test tank.
- Liquid hydrogen orientation tests in vacuum jacketed test tank.

Volume II documents the bulk of test data acquired during the liquid oxygen loading tests in the Test Cell 100 tank and the data from both the liquid oxygen and liquid hydrogen orientation testing with the vacuum jacketed Phase B cryogenic test tank.

## 2.0 EFFECTS OF CAPILLARY RETENTION SCREENS ON RF GAUGING

The effects of capillary retention screens contained within tanks that are to be gauged utilizing RF Gauging technique were examined in three specific areas. The first area of concern relates to the magnitude of microwave leakage through various types of meshes formed by wire grids. The second area relates to the effects of capillary screen materials on the empty cavity parameters which specify the characteristics of the particular tank to be gauged. The final area of concern relates to the presence of a small quantity of the test liquid trapped in the small openings of the capillary screen mesh in an essentially empty cavity, and its effect on empty tank parameters.

## 2.1 MICROWAVE LEAKAGE THROUGH CAPILLARY RETENTION SCREENS

The subject of microwave leakage through antenna mesh materials has been of great interest to those involved with the development of low-noise antennas for deep space communications and radio astronomy. The subject is also of particular interest to those involved with the prevention of microwave radiation hazards. Other areas where meshes are utilized are reflective surfaces on antennas, Fabry-Perot interferometers, microwave oven doors, and RF screen rooms. A search of available literature concerning the application of mesh materials to such applications reveals that a significant amount of experimental and theoretical work has been done on microwave reflectivity and transmission properties of wire grid type meshes. In all cases it can dramatically be shown that when the mesh diameter, d, is much less than the wavelength of the incident RF energy, the transmission loss through the mesh is extremely high. In effect, this means that fine mesh capillary screens will act as a barrier or wall to incident RF energy.

In a paper by Otoshi [1], a comparison of theoretical and experimental data on transmission of RF energy through meshes formed by round holes in a flat metallic plate was presented which indicated minimum transmission losses of 19 db. His results were obtained using mesh samples with $d/\lambda_0$ ratios ranging from .025 to .134. The greatest difference between theoretical and measured results was 10%.

With a 50 x 50 mesh capillary liquid retention screen material, mesh dimensions would be

$$a = \frac{1 \text{ inch}}{50} \times \frac{2.54 \times 10^{-2} \text{ meter}}{1 \text{ inch}} = 5.08 \times 10^{-4} \text{ meter}$$

By considering this dimension to be an effective distance between mesh centers and assuming microwave wavelengths for typical RF gauging operational frequencies, the approximate expression for transmission loss presented by Otoshi and shown below can be applied.

$$T_{bd} = 20 \log_{10} \frac{3ab\lambda_o}{2\pi d^3 \cos\theta_i} + \frac{32t}{d}$$

$T_{bd}$ = transmission loss in db (voltage transmission loss)

a = horizontal distance between mesh centers

b = vertical distance between mesh centers

$\lambda_o$ = wavelength of operating frequency

d = effective diameter of mesh

$\theta_i$ = angle of incidence

t = thickness of mesh

The following analysis considers obliquely incident plane wave angles of 0°, 35.1°, and 38.5° as did Otoshi in his tests. In considering the 50 x 50 mesh screen, the following approximate worst case mesh dimensions are assumed.

$a = b = 5.08 \times 10^{-4}$ meter

$d = 4.06 \times 10^{-4}$ meter

$t = 1.016 \times 10^{-4}$ meter (approximate diameter of screen wire)

These assumed dimensions are very rough approximations based on maximum dimensions for spacing in the 50 x 50 mesh, whose mesh openings would be shaped somewhat like a narrow slit rather than a circle. Nonetheless, using these assumed dimensions, a rough figure of merit for transmission loss through a 50 x 50 mesh capillary screen can be determined for various wavelengths which are typically encountered in RF gauging systems. These results are shown in Table I. Note that in this case the $d/\lambda_o$ ratios vary as a function of frequency from 0.00067 to .0067, as compared to the $d/\lambda_o$ ratios considered by Otoshi which range from 0.025 to 0.134.

TABLE I

CALCULATED TRANSMISSION LOSS DATA FOR
50 x 50 MESH CAPILLARY SCREEN

| Frequency GHz | $\theta_i$ deg. | $\frac{d}{\lambda_o}$ | $\frac{t}{d}$ | Theoretical Transmission Loss db |
|---|---|---|---|---|
| 0.5 | 0° | $0.67 \times 10^{-3}$ | .25 | 68.9 |
| | 35.1 | " | .25 | 70.6 |
| | 38.5 | " | .25 | 71.0 |
| 2.0 | 0° | $2.7 \times 10^{-3}$ | .25 | 56.8 |
| | 35.1 | " | .25 | 58.6 |
| | 38.5 | " | .25 | 59.0 |
| 3.0 | 0° | $4.06 \times 10^{-3}$ | .25 | 53.4 |
| | 35.1 | " | .25 | 55.0 |
| | 38.5 | " | .25 | 55.6 |
| 5.0 | 0° | $6.7 \times 10^{-3}$ | .25 | 48.1 |
| | 35.1 | " | .25 | 50.6 |
| | 38.5 | " | .25 | 51.0 |

In a paper by W. W. Mumford[2] an empircal formula expressing transmission through a grid of wires as applied to RF shielding is presented, and is shown here

$$\frac{P_o}{P_L} = \frac{B_2}{4}$$

where

$$|B| = \frac{\lambda}{a} \ln \left[ \frac{1}{.83 \exp \frac{2\pi r}{a}} \right]$$

$P_o$ = Incident power,

$P_L$ = Transmitted power

r = radius of screen wires

a = spacing between centers (mesh dimension)

The electric vector is assumed to be parallel to the mesh wires. According to Mumford this formula applies equally well to a screen of perpendicular wires by ignoring one or the other set of parallel wires forming the mesh. In considering the 50 x 50 mesh capillary screen, when this formula is applied it is seen that for small a/r ratios, RF transmission through the screen is entirely negligible (i.e. very high transmission loss). Table II shows the calculated results where

$$r = \frac{1.016 \times 10^{-4}}{2} = .508 \times 10^{-4} \text{ meter}$$

$$a = 5.08 \times 10^{-4} \text{ meter}$$

TABLE II

TRANSMISSION THROUGH A GRID OF WIRES

(50 X 50 MESH CAPILLARY SCREEN)

| Frequency (GHz) | $d/\lambda_o$ | $\|B\|$ | $P_o/P_L$ | Power Transmission Loss ( db) |
|---|---|---|---|---|
| 0.5 | $0.67 \times 10^{-3}$ | 514 | $6.6 \times 10^{4}$ | 48 |
| 2.0 | $2.7 \times 10^{-3}$ | 128 | $0.41 \times 10^{4}$ | 36 |
| 3.0 | $4.06 \times 10^{-3}$ | 86 | $0.18 \times 10^{4}$ | 33 |
| 5.0 | $6.7 \times 10^{-3}$ | 51.4 | 0.066 | 28 |

Note that the transmission loss calculations in Table I relate to voltage losses and those in Table II relate to power loss. In both sets of calculations 50 x 50 mesh screen with a plain square weave was assumed.

Calculations indicating that essentially no RF energy will pass through capillary screens of the type used for liquid retention and that such screen materials will in effect act as a wall or barrier to the RF energy have just been presented. To verify these results a series of RF transmission loss measurements were made using a test cavity in which a capillary screen partition was used to divide the cavity into two sections.

Figure 2-1 contains a block diagram of the test setup. Figure 2-2 shows the actual test tank as configured for the tests.

A transmitting probe was positioned in the larger section of the tank and a receiving probe was positioned in the smaller section just opposite the capillary screen partition sample. A reference probe was also placed in the larger section of the tank in front of the capillary screen partition. The RF energy source was tuned manually to frequencies corresponding to various modes which were established

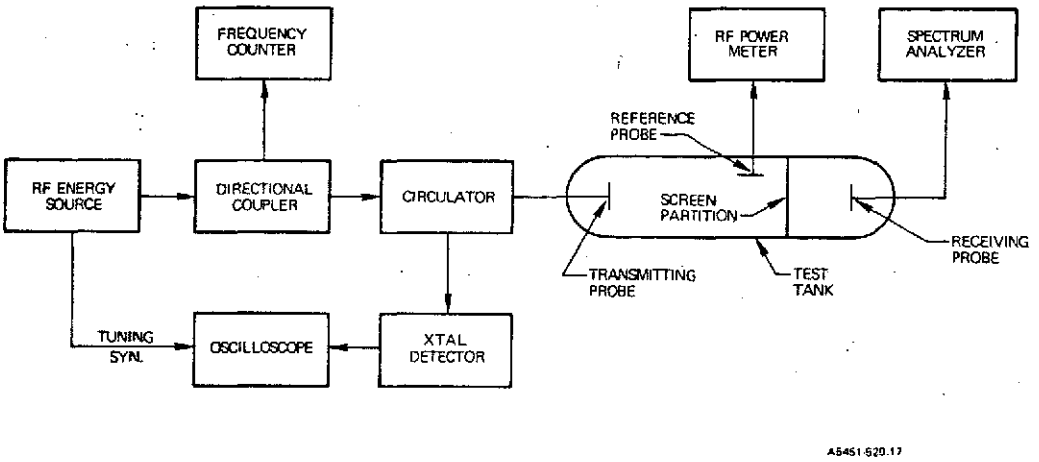


BLOCK DIAGRAM OF TRANSMISSION LOSS MEASUREMENT TEST SETUP

Figure 2-1

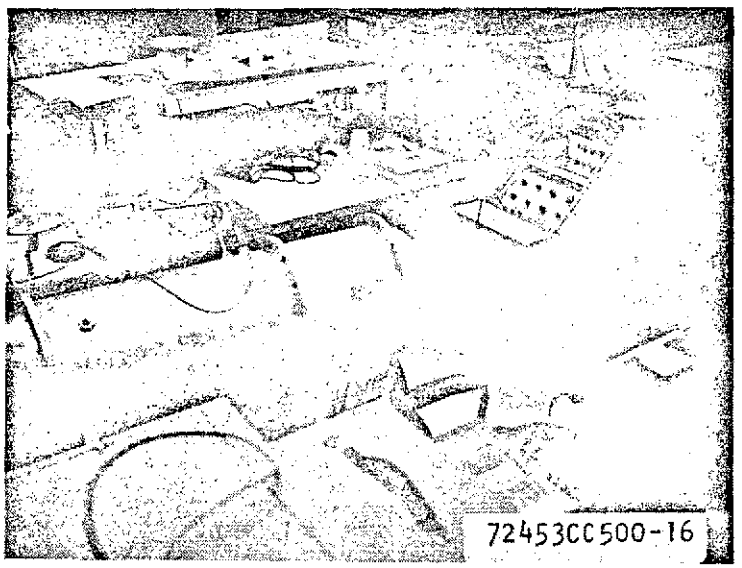


TEST TANK USED IN TRANSMISSION LOSS MEASUREMENTS

Figure 2-2

in the larger section of the test tank. The RF energy source was tuned to the center frequency, $f_o$, of each respective resonant mode by noting the maximum power dip in the RF energy reflected from the tank as detected by the oscilloscope. At each resonant frequency, measurements of RF power levels as detected at both the reference probe port and the receiving probe port were recorded. Several measurements were also taken for RF frequencies between resonant modes (i.e., off-resonance conditions). It should be noted that in these RF transmission loss measurement tests, the capillary screen samples formed a complete partition across the tank diameter. No gaps or openings were present to permit RF surface currents to leak around the capillary screen samples. In the event that such electrical surface currents were permitted to leak around the capillary screen samples, the RF power levels detected at the receiving probe would have been higher; and hence, valid transmission loss measurements relating to the capillary screen mesh dimensions could not have been made.

Tables III and IV, respectively, show the results of these tests for 50 x 250 mesh and 200 x 1400 mesh capillary screen partition samples. For both resonant and off-resonant conditions, the amount of RF energy transmitted through the screen samples is insignificant. For the screen sample with the larger mesh dimensions (50 x 250) the average detected power level behind the screen partition in the on-resonant frequency conditions was only -25.36 dbm, as compared to an average detected power level at the reference probe of +3.2 dbm. Such high transmission loss characteristics prevent detection of resonances in the cavity or area behind the capillary screen partition. As a consequence, it can be concluded that a quantity of mass behind such a capillary screen partition would not be sensed by the RF gauging system from a signal probe in front of the partition, where it is assumed that the capillary screen is so arranged as to form a total partition separating the test tank into two (or more) sections. If capillary screen channel propellant acquisition systems are used in an otherwise arbitrary test tank, an RF gauging system applied to such a tank would provide mass gauging only for the propellant mass in the principal volume of the tank, and would be insensitive to the propellant mass retained in the propellant acquisition channels.

## 2.2 EFFECTS OF CAPILLARY SCREENS ON TANK PARAMETERS

The area relating to the relative effects of metallic capillary screen materials on the cavity characteristics $Q_u$, $Q_L$, $Q_{ext}$, the unloaded, the loaded and the external Q values, respectively, is very important to understand since these tank parameters, along with the quality factor of the particular liquid to be gauged, $Q_d$, establish the overall

TABLE III

TRANSMISSION LOSS DATA FOR 50 x 250 MESH
CAPILLARY SCREEN PARTITION

| ON RESONANCE | | | OFF RESONANCE | | |
|---|---|---|---|---|---|
| Frequency (GHz) | Power at Reference Probe (dbm) | Power at Receiving Probe (dbm) | Frequency (GHz) | Power at Reference Probe (dbm) | Power at Receiving Probe (dbm) |
| 2.132 | 13.0 | -31 | 2.110 | 0.5 | -44 |
| 2.17 | 4.0 | -34 | 2.214 | 6.0 | -35 |
| 2.28 | 5.6 | -41 | 2.318 | 7.0 | -39 |
| 2.335 | 1.0 | -37 | 2.418 | -0.5 | -39 |
| 2.381 | -12.0 | -24 | 2.521 | -3.8 | -48 |
| 2.433 | 1.0 | -36 | 2.625 | 8.7 | -46 |
| 2.444 | 6.4 | -27 | 2.722 | 4.6 | -24 |
| 2.482 | 6.0 | -24 | 2.821 | 4.4 | -19 |
| 2.532 | 10.5 | -17 | 2.919 | 0.9 | -25 |
| 2.586 | 3.5 | -28 | 3.017 | -6.9 | -41 |
| 2.635 | 5.5 | -33 | 3.119 | -2.3 | -34 |
| 2.685 | 6.5 | -28 | 3.211 | 7.1 | -32 |
| 2.736 | 8.0 | -16 | 3.312 | -2.5 | -34 |
| 2.782 | 6.5 | -26 | 3.417 | 3.5 | -42 |
| 2.829 | 4.7 | -24 | 3.511 | -3.2 | -34 |
| 2.886 | 1.5 | -20 | 3.609 | -1.8 | -44 |
| 2.925 | 7.6 | -17 | 3.710 | -0.8 | -35 |
| 2.976 | 9.6 | -31 | 3.817 | -0.8 | -33 |
| 3.033 | -4.5 | -15 | | | |
| 3.071 | -2.5 | -18 | Averages | +1.11 dbm | -35.94 dbm |
| 3.116 | 5.0 | -16 | | | |
| 3.175 | 10.5 | -32 | | | |
| 3.227 | -2.0 | -30 | | | |
| 3.274 | 9.5 | -30 | | | |
| 3.323 | 6.5 | -27 | | | |
| 3.375 | 4.5 | -20 | | | |
| 3.424 | -1.3 | -21 | | | |
| 3.560 | -5.8 | -14 | | | |
| 3.610 | 8.0 | -36 | | | |
| 3.662 | -3.0 | -21 | | | |
| 3.706 | -8.2 | -21 | | | |
| 3.766 | 3.0 | -14 | | | |
| 3.814 | 0.5 | -30 | | | |
| 3.864 | 7.7 | -23 | | | |
| 3.911 | -0.9 | -28 | | | |
| 3.958 | 5.7 | -23 | | | |
| Averages | +3.21 dbm | -25.36 dbm | | | |

TABLE IV

TRANSMISSION LOSS DATA FOR 200 x 1400 MESH CAPILLARY SCREEN PARTITION

| ON RESONANCE | | | OFF RESONANCE | | |
|---|---|---|---|---|---|
| Frequency (GHz) | Power at Reference Probe (dbm) | Power at Receiving Probe (dbm) | Frequency (GHz) | Power at Reference Probe (dbm) | Power at Receiving Probe (dbm) |
| 2.149 | 6.8 | -33 | 2.135 | 8.4 | -48 |
| 2.267 | -15.0 | -52 | 2.315 | 0.5 | -42 |
| 2.363 | 7.8 | -37 | 2.338 | 3.0 | -40 |
| 2.469 | 7.0 | -42 | 2.441 | 1.0 | -38 |
| 2.559 | 2.5 | -35 | 2.542 | 2.0 | -43 |
| 2.669 | 11.8 | -40 | 2.645 | 6.3 | -35 |
| 2.759 | 1.5 | -37 | 2.742 | 11.5 | -40 |
| 2.957 | 9.8 | -35 | 2.844 | 2.5 | -53 |
| 3.070 | 0.25 | -43 | 2.947 | 7.7 | -52 |
| 3.156 | 8.9 | -38 | 2.997 | -1.5 | -33 |
| 3.257 | -13.0 | -36 | 3.045 | 0.0 | -32 |
| 3.357 | 11.0 | -35 | 3.094 | 3.6 | -34 |
| 3.465 | -4.0 | -36 | 3.141 | 10.5 | -42 |
| 3.553 | -6.0 | -34 | 3.241 | -7.5 | -47 |
| 3.653 | 4.5 | -38 | 3.349 | -13.0 | -50 |
| 3.753 | -14.0 | -36 | 3.444 | 6.1 | -29 |
| 3.848 | 10.5 | -39 | 3.541 | -7.0 | -31 |
| 3.941 | 2.5 | -32 | 3.639 | 5.3 | -40 |
| 2.201 | 5.0 | -42 | | | |
| 2.299 | 7.5 | -38 | Averages | +2.18 dbm | -40.50 dbm |
| 2.398 | -6.0 | -56 | | | |
| 2.501 | 7.5 | -56 | | | |
| 2.601 | 4.5 | -44 | | | |
| 2.604 | 0. | -34 | | | |
| 2.703 | 3.75 | -33 | | | |
| 2.798 | 1.0 | -46 | | | |
| 2.899 | 6.3 | -36 | | | |
| 3.002 | 4.0 | -44 | | | |
| 3.098 | 9.5 | -35 | | | |
| 3.194 | 7.2 | -46 | | | |
| 3.295 | 6.0 | -25 | | | |
| 3.391 | 5.0 | -41 | | | |
| 3.490 | -11.5 | -24 | | | |
| 3.685 | 2.5 | -38 | | | |
| 3.792 | -17.5 | -27 | | | |
| 3.886 | 1.5 | -43 | | | |
| Averages | +1.78 dbm | -38.5 dbm | | | |

system quality factor, $Q_L$. Through the relationship established by the deterministic formula representing the RF Gauging Scaling Model, $Q_L$ is a predominant factor which determines the characteristic loading response. (Reference Appendix A, Phase A Final Report, "Design, Development and Manufacture of a Breadboard Radio Frequency Mass Gauging System", Contract NAS 8-30160). By measuring the input impedance of a cavity as a function of frequency, the cavity characteristics $Q_u$, $Q_L$, and $Q_{ext}$ can be determined, since the impedance seen looking into a cavity is different at a resonant frequency than at frequencies either side of resonance. This impedance measurement method as depicted by Ginzton[3] was used to establish cavity parameters $Q_u$, $Q_L$, and $Q_{ext}$ in a small cylindrically-shaped cavity called an Echo Box, for each of the detected modes between 2.0 and 3.0 GHz. Figure 2-3 shows the test cavity and set-up used for these measurements. Figure 2-4 shows the test cavity and two circular screen samples.

Impedance measurements were made for each of the following cavity configurations:

1. Empty cavity.
2. Stainless steel circular plate positioned on bottom of test cavity.
3. 30 x 30 mesh stainless steel screen sample positioned on bottom of test cavity. (Plain square weave).
4. 50 x 250 mesh stainless steel capillary screen sample positioned on bottom of test cavity. (Twilled dutch weave).

Table V contains the average measured values for $Q_u$, $Q_L$, and $Q_{ext}$ for the resonant modes of the above cavity configurations where for each case the test cavity contained no liquid. Note, just as theory predicts, $Q_L$ is approximately equal to the parallel combination of $Q_u$ and $Q_e$ in the empty cavity case, as defined by

$$\frac{1}{Q_L} = \frac{1}{Q_u} + \frac{1}{Q_e}$$

From these first tests it is evident that:

- The presence of stainless steel in a normally high Q cavity (one consisting of silver plated, aluminum, or titanium walls) tends

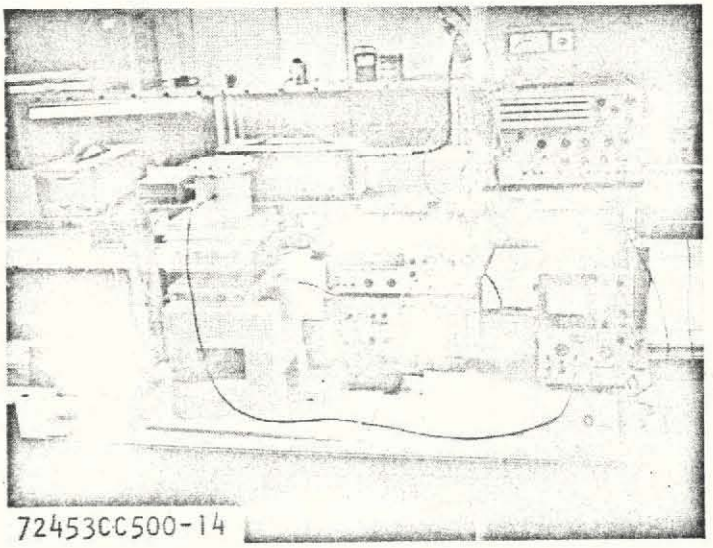


Q MEASUREMENT TEST SETUP

Figure 2-3

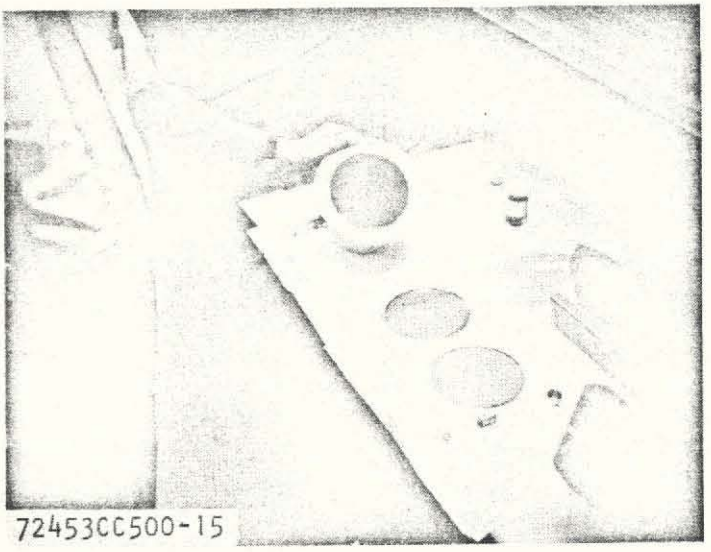


SMALL CYLINDRICAL CAVITY WITH SCREEN SAMPLES

Figure 2-4

to lower the loaded Q, $Q_L$. This lower value for $Q_L$ is in part due to the fact that the stainless steel is a poor electrical conductor, and consequently tends to dissipate energy.

- The presence of a stainless steel screen of a comparable overall diameter in the same nominally high Q cavity results in an even lower average $Q_L$ value. This lower value for $Q_L$ may be attributed in part to the extremely rough surface condition formed by the screen mesh, which provides for a large effective increase in the exposed surface area of the stainless steel. Also, the electrical contact between individual wires forming the mesh depends only on surface contact, and hence may cause a reduced surface current carrying capability.

- The resultant quality factor of a cavity containing a given quantity of stainless steel capillary screen material is dependent upon the mesh dimensions of that screen material.

TABLE V

TANK Q MEASUREMENTS - SMALL CYLINDRICAL CAVITY

| Cavity Configuration | Characteristic Q Values (Averages) | | |
|---|---|---|---|
| | $Q_u$ | $Q_e$ | $Q_L$ |
| Empty | 9,475 | 9,403 | 3,167 |
| Stainless Plate | 1,577 | 6,599 | 1,163 |
| 30 x 30 Mesh Screen | 1,618 | 3,497 | 957 |
| 50 x 250 Mesh Screen | 737 | 2,818 | 499 |

It should be noted that the magnitude of the reduction in the overall system quality factor, $Q_L$ would of course be dependent upon the percent of the total internal surface area comprised of the capillary screen; and also, the material from which the screen is fabricated.

## 2.3 EFFECTS OF LIQUID TRAPPED ON CAPILLARY SCREEN MESH

To determine how the presence of a small quantity of the test liquid trapped in the small openings of the capillary screen mesh would affect the essentially empty cavity parameters, measurements of the $Q_u$, $Q_e$ and $Q_L$ factors were made for several modes in the small cylindrical test cavity (Figure 2-4) with the capillary screen samples, where under each test configuration the measurements were made both with and without a sample of RP-1 in the test cavity. In each case 5 ml of RP-1 was poured over the screen samples in the bottom of the test cavity so as to fill the screen mesh openings. The same test was performed with the test cavity in which no screen samples were used. Table VI identifies the test cavity configuration, the examined nodal frequency, and the respective cavity parameters $Q_u$, $Q_e$ and $Q_L$. For each cavity configuration it is apparent that the loaded Q, $Q_L$ increases as the small quantity of RP-1 is added to the test cavity. The point to note here is that the same relative increase in $Q_L$ with the addition of the RP-1 occurred for each cavity configuration; i.e., both with and without the capillary screen samples. This suggests that the wetting action on capillary screens will not be detrimental to gauging system performance.

## TABLE VI

### TANK Q MEASUREMENTS - SMALL CYLINDRICAL CAVITY/CAPILLARY SCREEN WETTING EFFECTS

| Cavity Configuration | Nodal Freq (GHz) | RP-1 Quantity | $Q_u$ | $Q_e$ | $Q_L$ |
|---|---|---|---|---|---|
| No Screen or Plate in Cavity | 2.64025 | Dry-Empty | 3,616 | 11,001 | 2,838 |
| | | 5 ml | | | |
| | 2.72651 | Dry-Empty | 10,486 | 4,260 | 3,495 |
| | | 5 ml | 14,342 | 5,240 | 3,893 |
| | 2.95338 | Dry-Empty | 3,691 | 29.532 | 3,691 |
| | | 5 ml | 15,535 | 17,362 | 9,229 |
| Stainless Steel Plate in Cavity | 2.4914 | Dry-Empty | 1,176 | 7.558 | 1,089 |
| | | 5 ml | 2,446 | 7,128 | 1,652 |
| 30x30 Mesh Stainless Steel Screen in Cavity | 2.73761 | Dry-Empty | 752 | 8,051 | 752 |
| | | 5 ml | 2,914 | 4,892 | 1,943 |
| 50x250 Mesh Stainless Steel Screen in Cavity | 2.07623 | Dry-Empty | 171 | 388 | 120 |
| | | 5 ml | 530 | 322 | 184 |
| | 2.53119 | Dry-Empty | 1,488 | 6,841 | 1,211 |
| | | 5 ml | 3,123 | 10,541 | 2,608 |
| | 2.7355 | Dry-Empty | 606 | 4,144 | 572 |
| | | 5 ml | 870 | 4,876 | 771 |

In order to provide additional insight into the relative effects that metallic capillary screen materials have on the cavity characteristics $Q_u$, $Q_{ext}$, and $Q_L$ the unloaded, the external and the loaded Q values respectively, additional tests were conducted on a larger test cavity using the same impedance method. This test cavity is shown in Figure 2-5. The test cavity configuration is cylindrical with a hemispherically protruding top dome, and a flat bottom.

The capillary screen samples were fastened directly to the circular end plate at the bottom of the test tank.

Values for $Q_u$, $Q_{ext}$ and $Q_L$ were measured for each of eight resonant modes established between .30 GHz and .60 GHz. These measurements were taken first with a 50 x 250 mesh and then with a 200 x 1400 mesh capillary stainless steel screen test sample at the bottom of the test cavity. To provide a set of reference data from which these Q measurement results could be compared, additional measurements of $Q_u$, $Q_{ext}$, and $Q_L$ were made for the same resonant modes with a plain circular aluminum plate and also a plain circular stainless steel plate secured at the bottom of the test cavity. Table VII contains $Q_u$ $Q_{ext}$, $Q_L$ for eight resonant modes for each respective sample located at the bottom of the test cavity.

TABLE VII

EMPTY TANK Q MEASUREMENTS

TEST CAVITY VOLUME 0.119 CUBIC METERS

| Cavity Configuration | Characteristic Q Values (Averages) | | |
|---|---|---|---|
| | $Q_u$ | $Q_{ext}$ | $Q_L$ |
| Aluminum Plate | 901 | 824 | 293 |
| Stainless Steel Plate | 912 | 962 | 295 |
| 50 x 250 Mesh Screen | 949 | 993 | 394 |
| 200 x 1400 Mesh Screen | 845 | 893 | 265 |

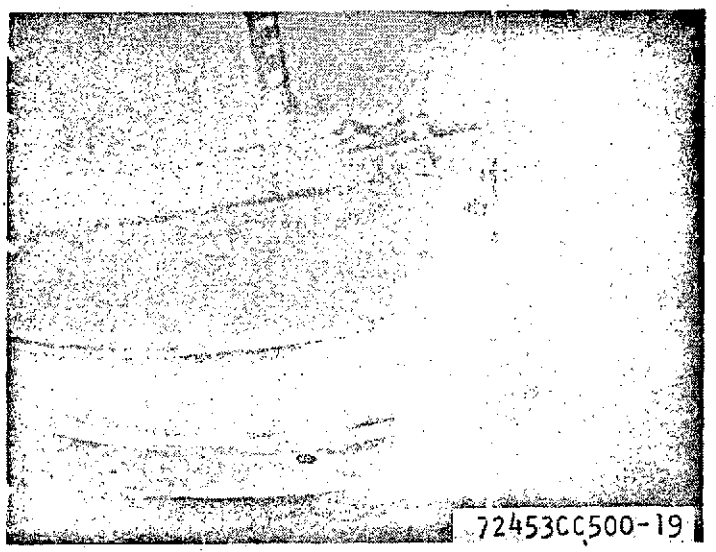


POSITION OF CAPILLARY SCREEN SAMPLE IN TEST CAVITY

Figure 2-5

These results confirm that the presence of capillary liquid retention screens in a test tank will in general lower the characteristic Q values of that tank. However, it should be noted that the presence of the capillary screen samples in the previous test cavity produced a much more dramatic reduction in the characteristic Q values for the otherwise empty test cavity. Table VIII compares the volume (V), total internal surface area (S), the V/S ratio, and the relative % of total internal surface area covered by capillary screen for each respective test cavity. It is seen that a capillary screen sample in the smaller test cavity takes up nearly 19% of the total internal surface area whereas in the larger test cavity the capillary screen sample comprised only 7.9% of the total internal surface area.

TABLE VIII

PHYSICAL CHARACTERISTICS OF TEST CAVITIES

| TEST CAVITY | VOLUME ($m^3$) | SURFACE AREA ($m^2$) | V/S (m) | PERCENT SURFACE AREA COVERED BY SCREEN |
|---|---|---|---|---|
| Echo Box | .0023 | .0973 | .0238 | 18.7 |
| Larger Test Tank | .119 | 1.435 | .0829 | 7.9 |

It should also be noted that the antenna in the smaller test cavity was a small coupling loop which contained no radome, whereas the spiral antenna in the larger test cavity was covered with a radome. Consideration of the respective V/S ratios and the relative proximity of the antennas to the screen samples suggests that in most typical cavities containing antennas with radomes, the presence of metallic capillary screen materials will not preclude the implementation of an RF Gauging system.

Tests were conducted on the small echo box in which a small quantity of test liquid (RP-1) was intentionally placed in the small opening of the capillary screen mesh samples in order to determine if that wetting action on the capillary screen would be detrimental to gauging system performance. To substantiate whether or not this conclusion could also be applied to other tank configurations,

measurements of $Q_u$, $Q_{ext}$ and $Q_L$ were made using the larger test tank configuration described above. In the otherwise empty test cavity RP-1 was placed on the screen samples in the bottom of the test cavity so as to fill the screen mesh openings. (55 ml of RP-1 was required). The same tests were also performed using the flat circular aluminum and stainless steel plates in the bottom of the test cavity, where in each case the same quantity of RP-1 was spread over the top surface of the palte. Table IX identifies the test cavity configurations and the respective average cavity parameters. Each value shown is the average for eight resonant modes.

Comparison of the results obtained in Tables VII and IX (without RP-1 film and with RP-1 film) show, on the average, the same magnitude increase in system Q as liquid is introduced into the test cavity, both for the solid metal plates and the capillary screen materials. These results, therefore, support the results obtained earlier with the small echo box cavity which also indicated that fuel wetting action on capillary screens will not be detrimental to gauging system performance.

TABLE IX

TANK Q MEASUREMENTS

Test Cavity Volume 0.119 Cubic Meters
55 ml RP-1 On Screen and Plate Samples

| Cavity Configuration | Characteristic Q Values (Averages) | | |
|---|---|---|---|
| | $Q_u$ | $Q_{ext}$ | $Q_L$ |
| Aluminum Plate | 970 | 661 | 304 |
| Stainless Steel Plate | 799 | 928 | 293 |
| 50 x 250 Mesh Screen | 806 | 821 | 284 |
| 200 x 1400 Mesh Screen | 831 | 851 | 284 |

## 3.0 ZERO GRAVITY FLIGHT TESTS

In order to further evaluate the RF gauging system, zero gravity environmental tests were performed aboard the USAF KC-135 tanker at WPAFB. Tests were performed using a 1/10 scale SIVB $LH_2$ tank fabricated under Phase A of this contract. The scale SIVB $LH_2$ tank was enclosed within a test apparatus cage that was made structurally sound for flight aboard the KC-135. The partially assembled and completed test apparatus is shown in Figures 3-1 and 3-2. The complete test apparatus consisted of : a test fluid reservoir tank, liquid transfer valves and lines, pressure regulators and gauges to effect liquid transfer, emergency dump valves and lines for both the test and reservoir tank, a capacitance liquid level gauge in the reservoir tank, a recirculation pump and a breadboard RF gauging electronics package. A fluidic system schematic is shown in Figure 3-3 and a functional gauging block diagram is shown in Figure 3-4.

As a safety precaution, the test apparatus cage was purged with gaseous nitrogen rather than cabin air, since the test fluid to be gauged was benzene which is highly volatile. Prior to flight the test apparatus was subject to a ground test where a partial vacuum in the test apparatus interior equivalent to 15,000 ft. in altitude was obtained with no structural failure or permanent deformations.

The basic maneuver performed by the KC-135 to induce a zero gravity condition is a hyperbolic flight maneuver in which the aircraft "porpoises "that is to say, dives then rapidly pulls out of the dive. Under this set of flight conditions the following environmental conditions are imposed upon the test apparatus:

1. Each zero 'G' maneuver is preceded by an acceleration of 2 G's necessitated by the aircraft approach into the maneuver.

2. The transition from 2 'G's' to a zero 'G' condition takes approximately two seconds.

3. The zero 'G' condition generally can be maintained for approximately 25-30 seconds.

4. As the zero 'G' condition terminates, the pilot must pull the aircraft out a dive necessitating a second 2 'G' condition. The transition time in this case is generally 5-10 seconds.

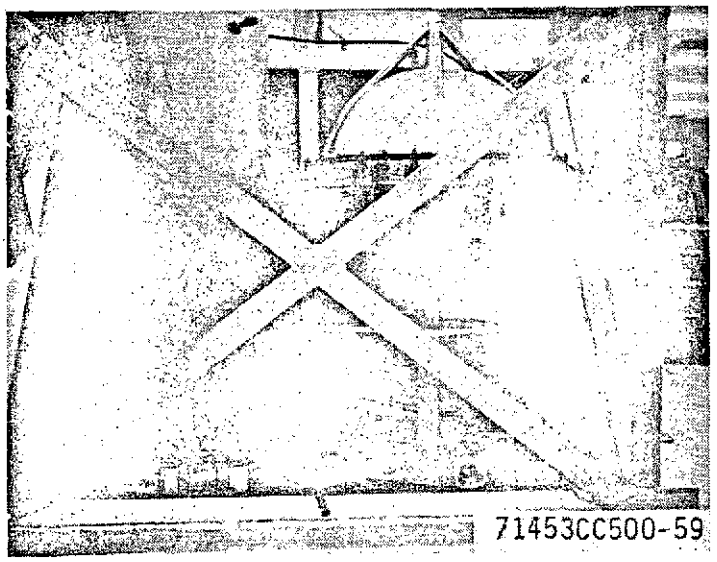


TEST APPARATUS - INTERNAL TANK POSITIONS

Figure 3-1

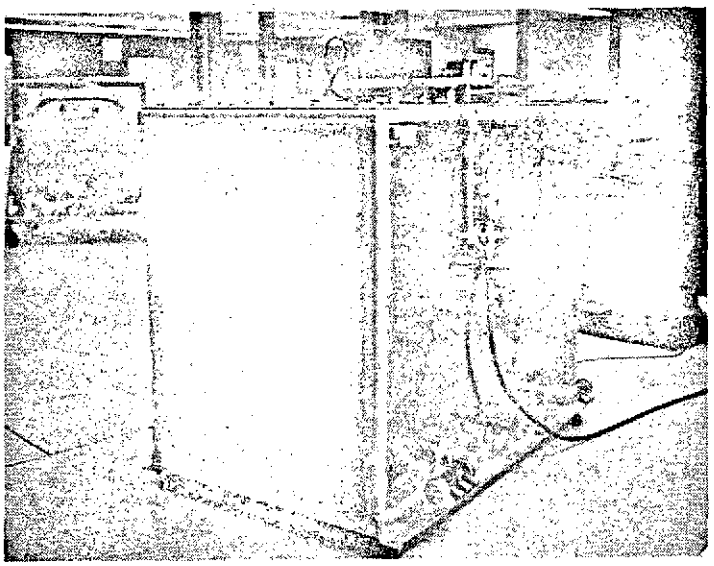

ZERO 'G' TEST APPARATUS

Figure 3-2

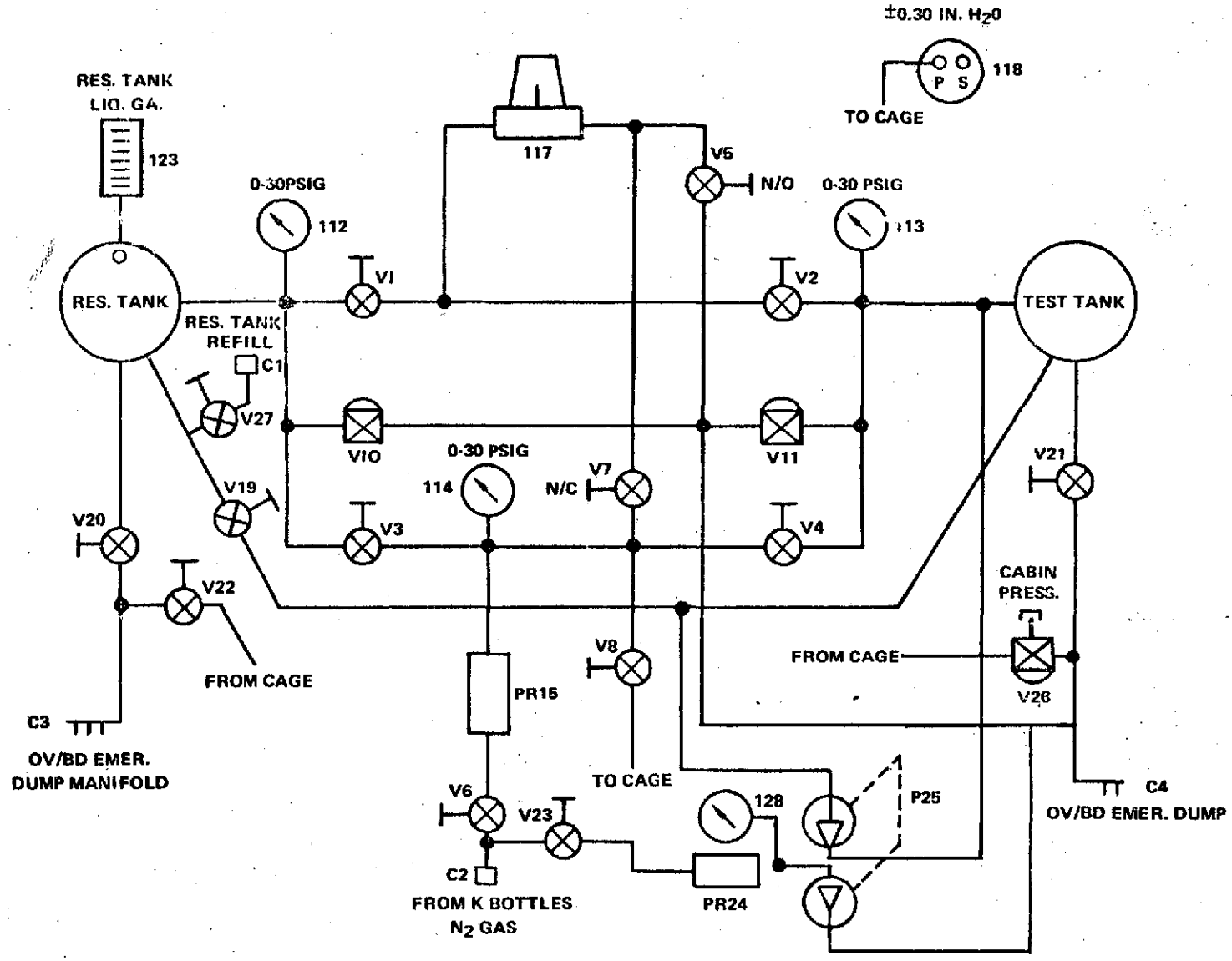


Figure 3-3

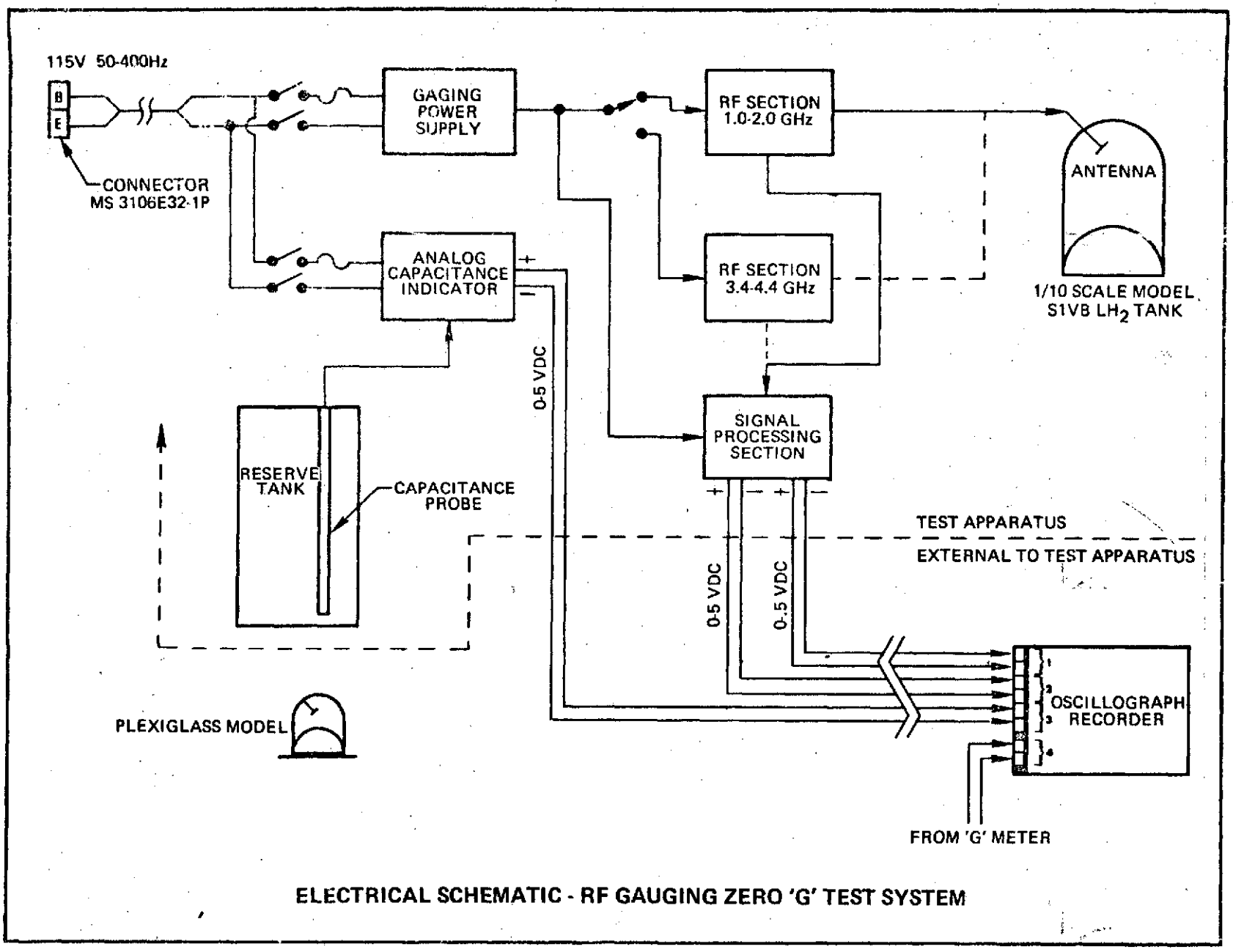


ELECTRICAL SCHEMATIC - RF GAUGING ZERO 'G' TEST SYSTEM

Figure 3-4

Three electrical outputs were recorded on an oscillograph during the zero 'G' maneuvers.

- the RF gauging systems analog output
- an accelerometer output/g-meter output
- the capacitance gauge output

## 3.1 GROUND TESTS OF THE 1/10 SIVB ZERO-G TEST APPARATUS

Preliminary ground based tests were performed in two RF frequency bands, a 1-2GHz band in order to generate an ascending characteristic response and a 3.4-4.4 GHz band in order to generate a descending characteristic response as a function of increasing mass. Figures 3-5 and 3-6 are X-Y plots of the gauging system output versus mass loading for a 1-2GHz band and a 3.4-4.4GHz band respectively. The 3.4-4.4 GHz band is the preferred gauging response for this tank and the test fluid benzene.* It should be noted that the wavelength at 1GHz is 30 centimeters and the scale tank is 63 centimeters in diameter.** As the frequency is lowered, the ratio gets smaller and the number of resonant modes that can be set up in the tank is reduced. This in turn causes liquid location in the tank to have a greater effect on mode count as a function of the liquid placement within the tank. At 3.4 GHz a wavelength is 7.15/1, consequently better RF sampling of the test fluid occurs.

Prior to flight testing system orientation testing of the 1/10 scale SIVB tank was performed. Testing was performed in a gimbal fixture that allowed the tank to be rotated a full 360°. An X-Y plot of the orientation test (3.4-4.4 GHz band) results is shown in Figure 3-7.

The orientation test data for the 3.4-4.4 GHz frequency band for the 1/10 scale system was broken down and analyzed in terms of absolute worst case percent of full mass error based on the nominal shape of the RF gauging loading response. See Figure 3-8. This error analysis provides the mass error about a point at each incremental loading quantity and is defined by:

$$\text{Mass Error} = \pm \frac{\left(\begin{array}{c}\text{Worst Case Spread} \\ \text{in Analog Output} \\ \text{At Given Incremental} \\ \text{Mass Loading}\end{array}\right)\left(\begin{array}{c}\text{Characteristic Mass} \\ \text{Sensitivity At} \\ \text{Respective Incremental} \\ \text{Mass Loading}\end{array}\right)}{2}$$

* This is evident from the smooth response characteristics.

** The ratio of tank diameter to wavelength is small, 2.1/1.

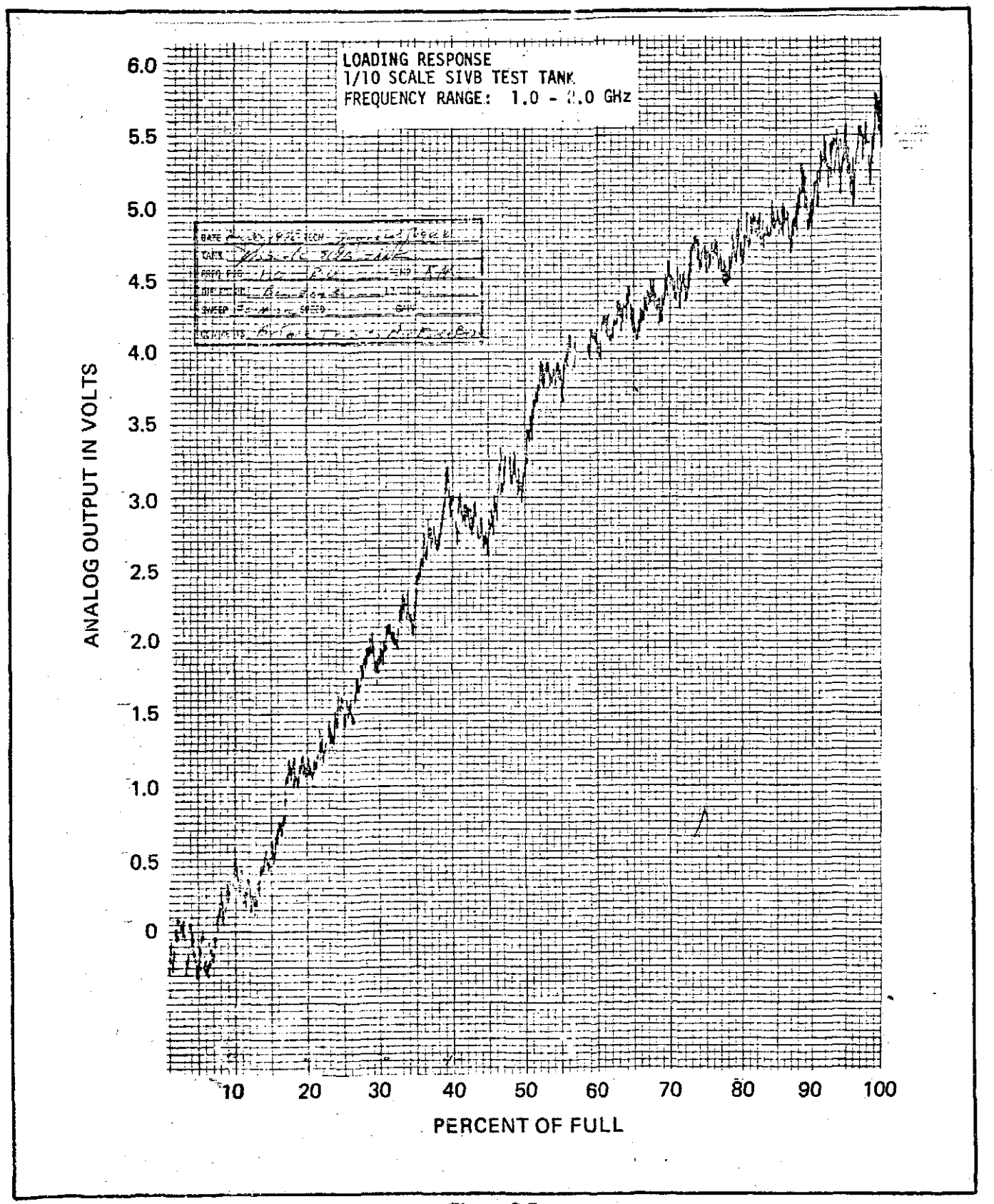
LOADING RESPONSE
1/10 SCALE SIVB TEST TANK
FREQUENCY RANGE: 1.0 - 2.0 GHz
ANALOG OUTPUT IN VOLTS
6.0
5.5
5.0
4.5
4.0
3.5
3.0
2.5
2.0
1.5
1.0
0.5
0
10
20
30
40
50
60
70
80
90
100
PERCENT OF FULL

Figure 3-5

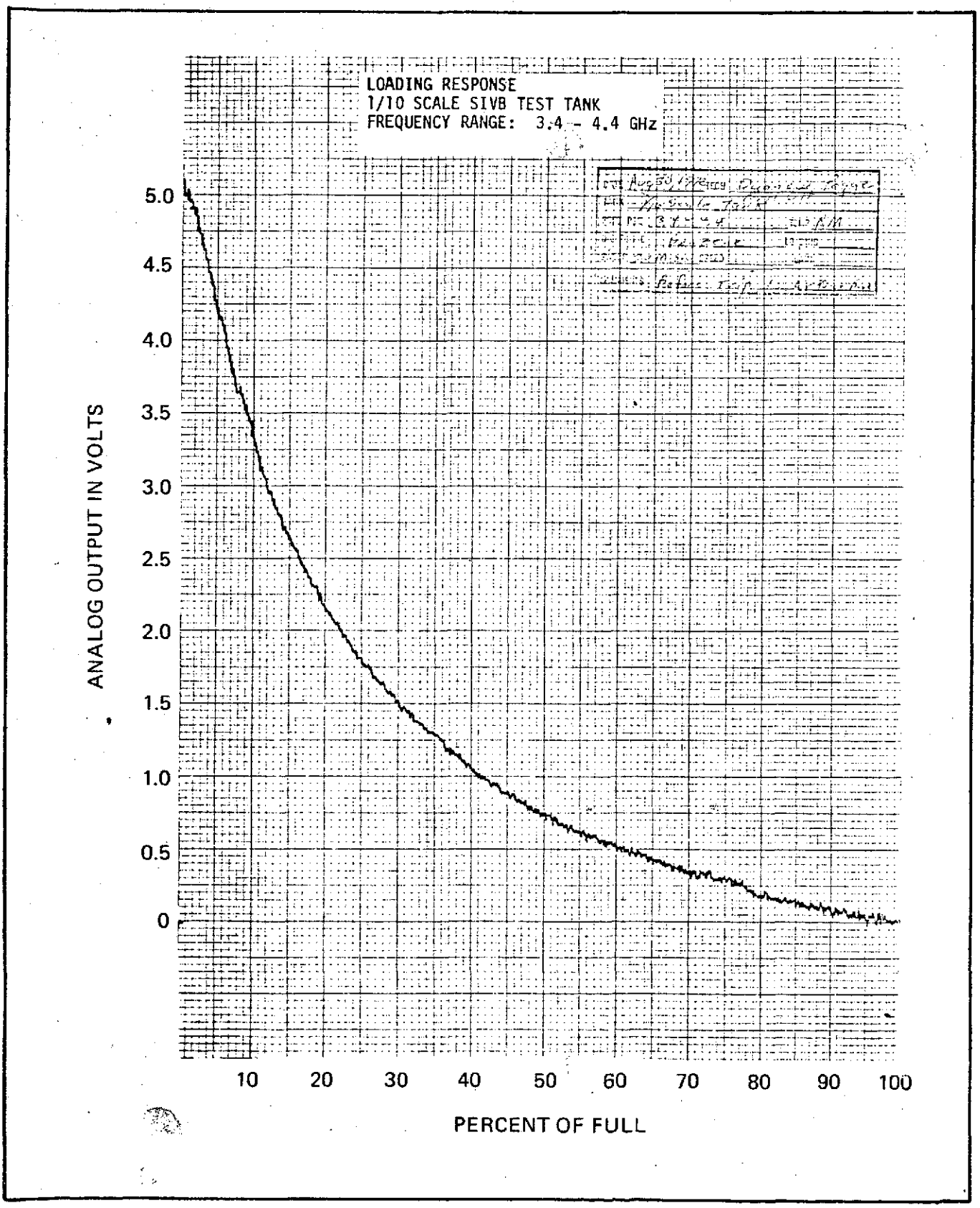


Figure 3-6

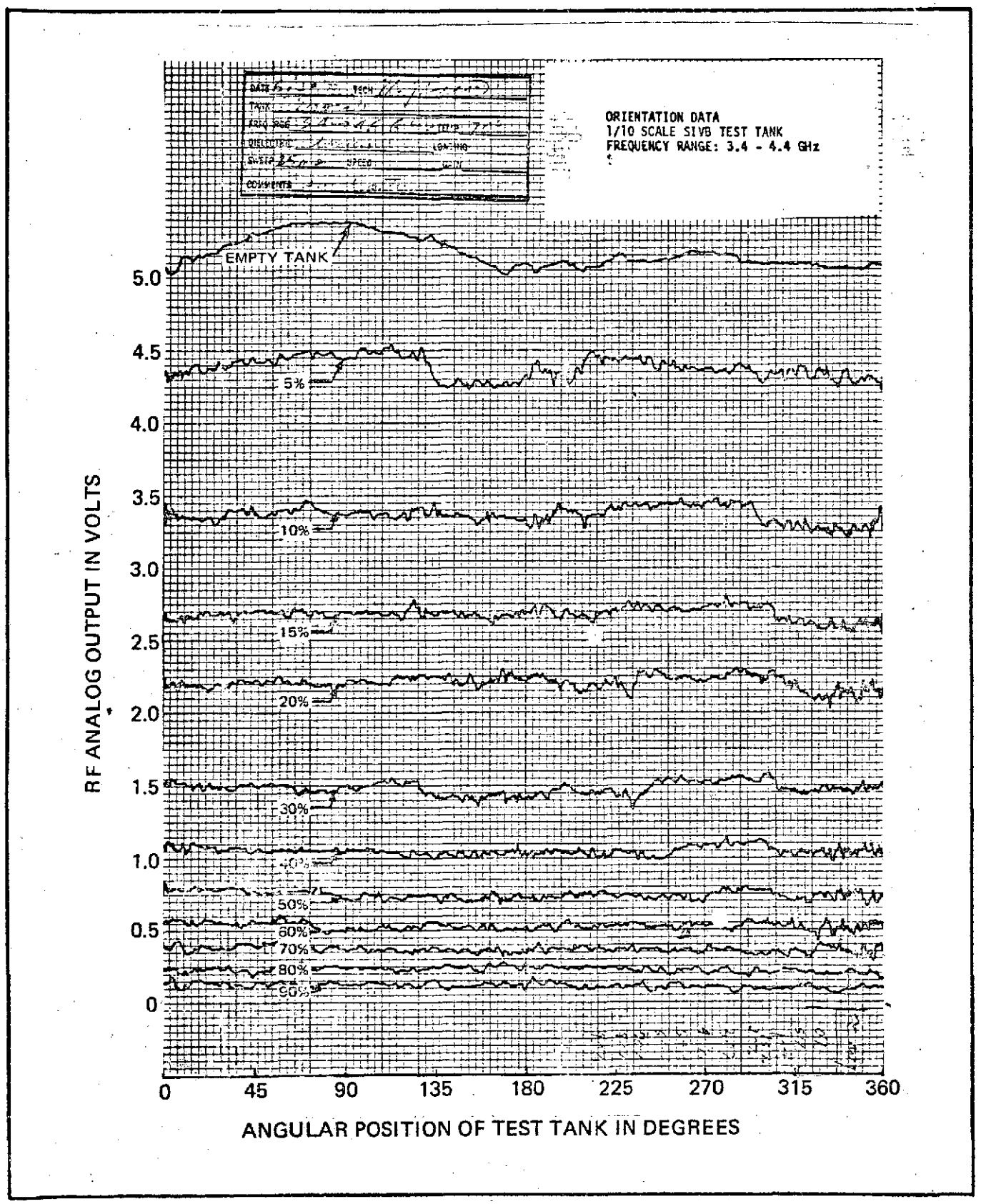


Figure 3-7

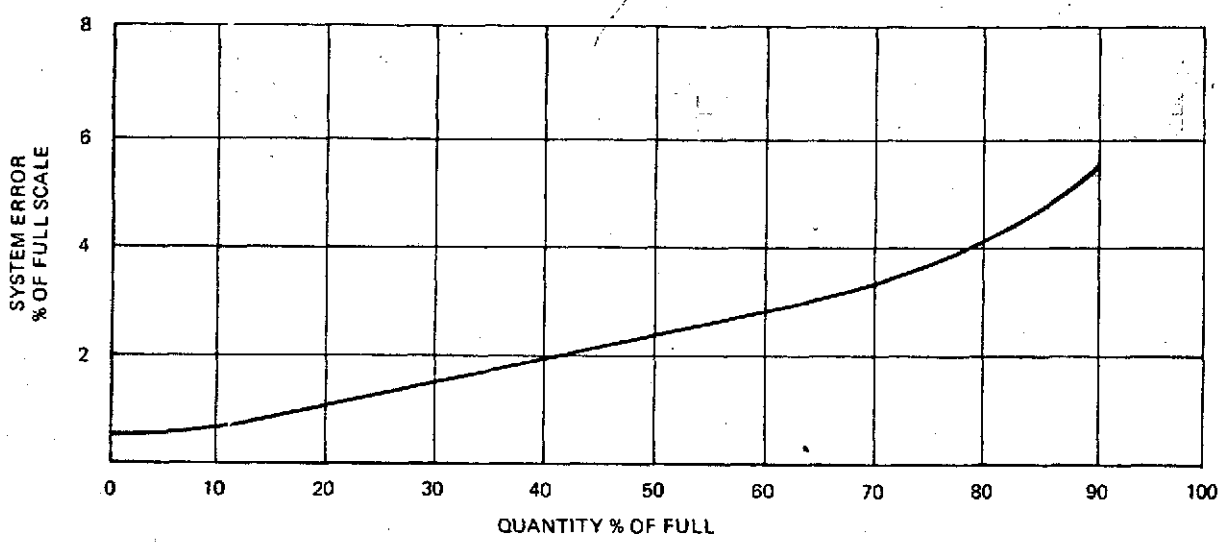


ERROR -% OF FULL SCALE
ORIENTATION TEST
3.4 - 4.4 GHz FREQUENCY RANGE

Figure 3-8

where the characteristic mass sensitivity is specified from the nominal slope of the characteristic loading curve at each respective incremental mass loading by:

$$\text{Characteristic Mass Sensitivity} = \frac{\Delta \text{ Mass}}{\Delta \text{ Analog output}}.$$

It is of particular significance to note the magnitude of the shift in the RF analog output for the empty test tank. A series of tests were performed with the test system to establish the cause for this variation in RF analog output with the empty test tank. All theoretical and applied reasoning explicitly indicate that the number of resonant modes established within a completely empty test cavity is independent of the orientation of that cavity with respect to cavity. Thus far it has been determined that these variations in output relate to changes in mechanical characteristics of the RF probe assembly located in the test tank.

Unfortunately, the 1/10 scale SIVB tank did not readily lend itself to modifications; since it is a welded assembly, the probe structure could not be removed. As a consequence the test results presented here can be assumed to contain a certain hardware-induced error, which in all probability reflects on the calculated mass error for each respective mass loading. No attempts were made to mathematically remove the hardware-induced source of error from the calculated mass errors associated with the data obtained in preflight orientation testing and the actual KC-135 tests.

## 3.2 KC-135 ZERO GRAVITY FLIGHT TESTS

On April 25, 1972 the system was flight tested through a total of 40 Zero 'G' maneuvers. The testing proceeded as follows: First with 3.4-4.4 GHz frequency band, two maneuvers were flown with the test tank empty. After these maneuvers, benzene was then transferred from the reservoir tank into the 1/10 scale SIVB test tank until it was filled to a fractional mass of .1 (10% full). At that point, two more Zero 'G' maneuvers were flown. A set of two maneuvers were then flown for each of the remaining 10% mass increments including the full test tank condition. In each set of two maneuvers, the first was flown with the recirculating benzene pump operating, and during the second maneuver of each set it was turned off. After the last set of maneuvers were performed with the 3.4-4.4 GHz frequency band, the 1-2 GHz frequency RF source was turned on and used in the remaining maneuvers in which the same test procedure was followed except that the test tank was emptied in 10% increments.

The flight testing on April 26 was a repeat of the previous day's testing wherein both operating frequency ranges were evaluated at 10% incremental loading levels, both with and without the recirculating pump. On the second day the first two maneuvers were performed with a purged empty tank.

Figure 3-9 shows the system error curve as a function of mass loading for the 1-2 GHz band and 3.4-4.4 GHz band used during the flight tests. The calculated mass errors depicted in these graphs are based on worst case, instantaneous maximum/minimum values from a medium RF analog voltage recorded at each respective mass loading during each zero 'G' period. Error is presented in terms of percent of full scale with no time average or statistical reduction of the data.

During this series of tests a high electrical noise environment was noticed. Post-flight tests indicated that some variations during the flight tests were caused by anomalies within the RF breadboard electronics. Because of these problems additional zero 'G' flight tests were performed at WPAFB.

The retesting of the 1/10 scale test apparatus in the Air Force KC-135 took place on September 7, 1972. The test plan called for the test configurations specified in Table X.

Maneuvers 1 through 28 involved the 3.4-4.4 GHz frequency band with various incremental quantities, where in each case the benzene recirculation pump was not operated during the respective maneuvers. The test tank was completely empty (dry) during the first four maneuvers. Benzene was added to the tank between every set of two consecutive maneuvers as specified in Table X. Maneuvers 29 through 44 involved the same frequency range (3.4-4.4 GHz) where benzene was removed from the test tank between every set of two consecutive maneuvers as specified in Table X. The benzene recirculation pump was operated during these maneuvers. Maneuvers 45 through 64 involved the 1.0 - 2.0 GHz frequency band. Benzene was added to the test tank between every set of two consecutive maneuvers as specified in Table X. The benzene recirculation pump was operated during the second maneuver of each remaining set of maneuvers.

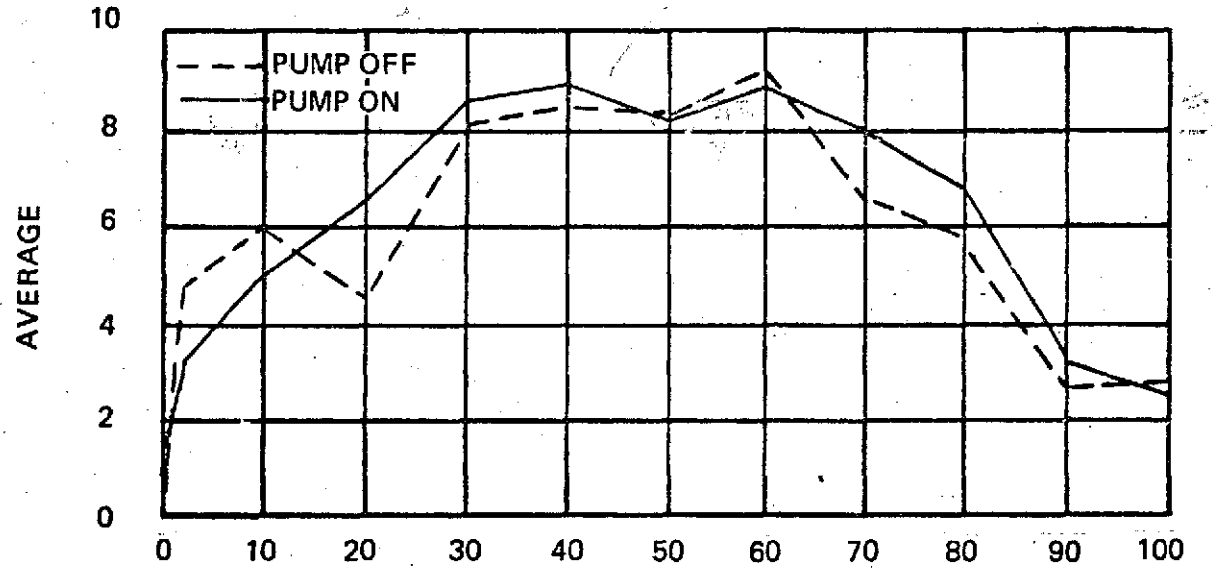


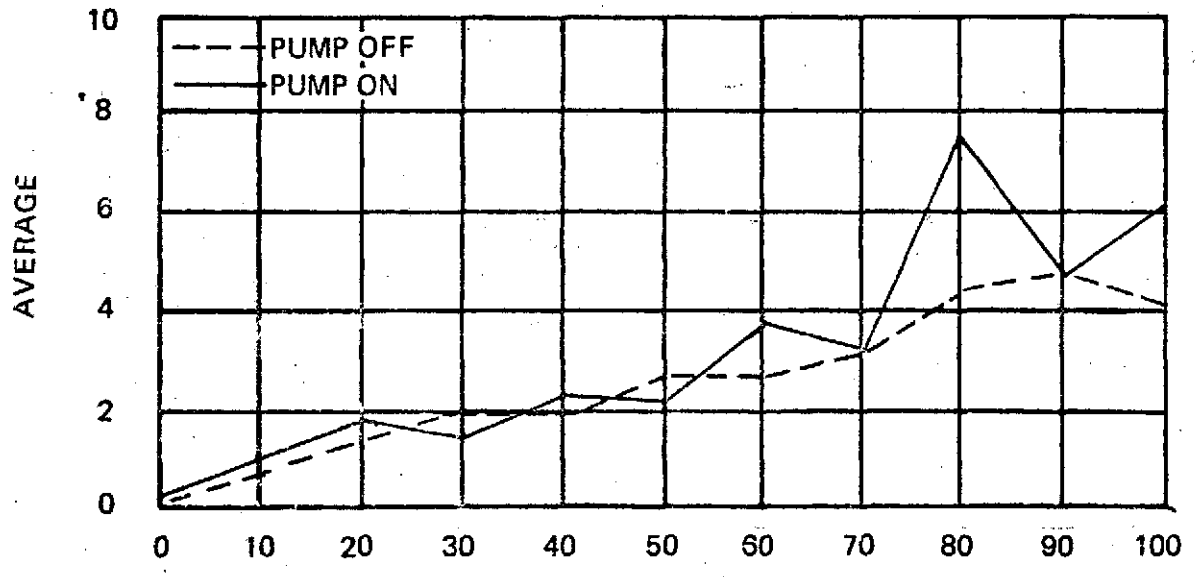


SYSTEM ERROR CURVES

A5451-520.1

Figure 3-9.

# TABLE X

## RF GAUGING TEST CONFIGURATIONS

### MODIFIED TEST PLAN - SEPTEMBER 7, 1972

| Maneuver No. | Approx. % Fill | Recirc. Pump | RF Freq. Range | Maneuver No. | Approx. % Fill | Recirc. Pump | RF Freq. Range |
|---|---|---|---|---|---|---|---|
| 1 | 0 | Off | 3.4-4.4 GHz | 33 | 40 | On | 3.4-4-4 GHz |
| 2 | 0 | " | " | 34 | 40 | " | " |
| 3 | 0 | " | " | 35 | 30 | " | " |
| 4 | 0 | " | " | 36 | 30 | " | " |
| 5 | 5 | " | " | 37 | 20 | " | " |
| 6 | 5 | " | " | 38 | 20 | " | " |
| 7 | 10 | " | " | 39 | 15 | " | " |
| 8 | 10 | " | " | 40 | 15 | " | " |
| 9 | 15 | " | " | 41 | 10 | " | " |
| 10 | 15 | " | " | 42 | 10 | " | " |
| 11 | 20 | " | " | 43 | 5 | " | " |
| 12 | 20 | " | " | 44 | 5 | " | " |
| 13 | 30 | " | " | 45 | 0 | Off | 1.0-2.0 GHz |
| 14 | 30 | " | " | 46 | 0 | On | " |
| 15 | 40 | " | " | 47 | 10 | Off | " |
| 16 | 40 | " | " | 48 | 10 | On | " |
| 17 | 50 | " | " | 44 | 20 | Off | " |
| 18 | 50 | " | " | 50 | 20 | On | " |
| 19 | 60 | " | " | 51 | 30 | Off | " |
| 20 | 60 | " | " | 52 | 30 | On | " |
| 21 | 70 | " | " | 53 | 40 | Off | " |
| 22 | 70 | " | " | 54 | 40 | On | " |
| 23 | 80 | " | " | 55 | 50 | Off | " |
| 24 | 80 | " | " | 56 | 50 | On | " |
| 25 | 90 | " | " | 57 | 60 | Off | " |
| 26 | 90 | " | " | 58 | 60 | On | " |
| 27 | 95 | " | " | 59 | 70 | Off | " |
| 28 | 95 | " | " | 60 | 70 | On | " |
| 29 | 70 | On | " | 61 | 80 | Off | " |
| 30 | 70 | " | " | 62 | 80 | On | " |
| 31 | 60 | " | " | 63 | 90 | Off | " |
| 32 | 60 | " | " | 64 | 90 | On | " |

It should be noted that this second Zero 'G' test was performed under the same conditions and the same parameters were recorded as with the first test.

For each of the first 44 test maneuvers involving the 3.4-4.4 GHz frequency range, the maximum and minimum value of the RF analog output voltage was determined for:

a. The Zero 'G' portion of the maneuver.

b. The leading 2 'G' portion of the maneuver.

c. The transition time period between 2 'G's and Zero 'G'.

Using these worst case instantaneous maximum/minimum values of the recorded RF output for each of the above gravity condition time periods, a system mass error was calculated using the characteristic loading response curve to establish mass sensitivity at each respective mass loading. (i.e., slope of curve at each respective mass loading). Table XI contains a summary of these error calculations for each respective maneuver and test condition. It is significant to note that the spread in analog voltage for each respective maneuver and incremental fill (including the empty/dry tank) is of approximately the same order of magnitude. No time average or statistical technique has been applied to the error analysis of the Zero 'G' flight test data presented herein. Figure 3-10 contains plots of the calculated mass errors versus percent mass loadings for each respective time interval of the first 28 maneuvers. Also included in the top graph of Figure 3-10 is a plot of the calculated mass error versus percent mass loading where the offset in the average analog output detected during the empty tank maneuvers was subtracted from the analog output deviation for each respective incremental loading on a prorated basis in accordance with the characteristic gauging sensitivity at that incremental loading. Figure 3-11 contains plots of the calculated mass errors for each respective time interval for maneuvers number 29 thru 44. Similar calculations were made for maneuvers 44 thru 64 involving the 1.0-2.0 GHz frequency range. The results are plotted in Figure 3-12.

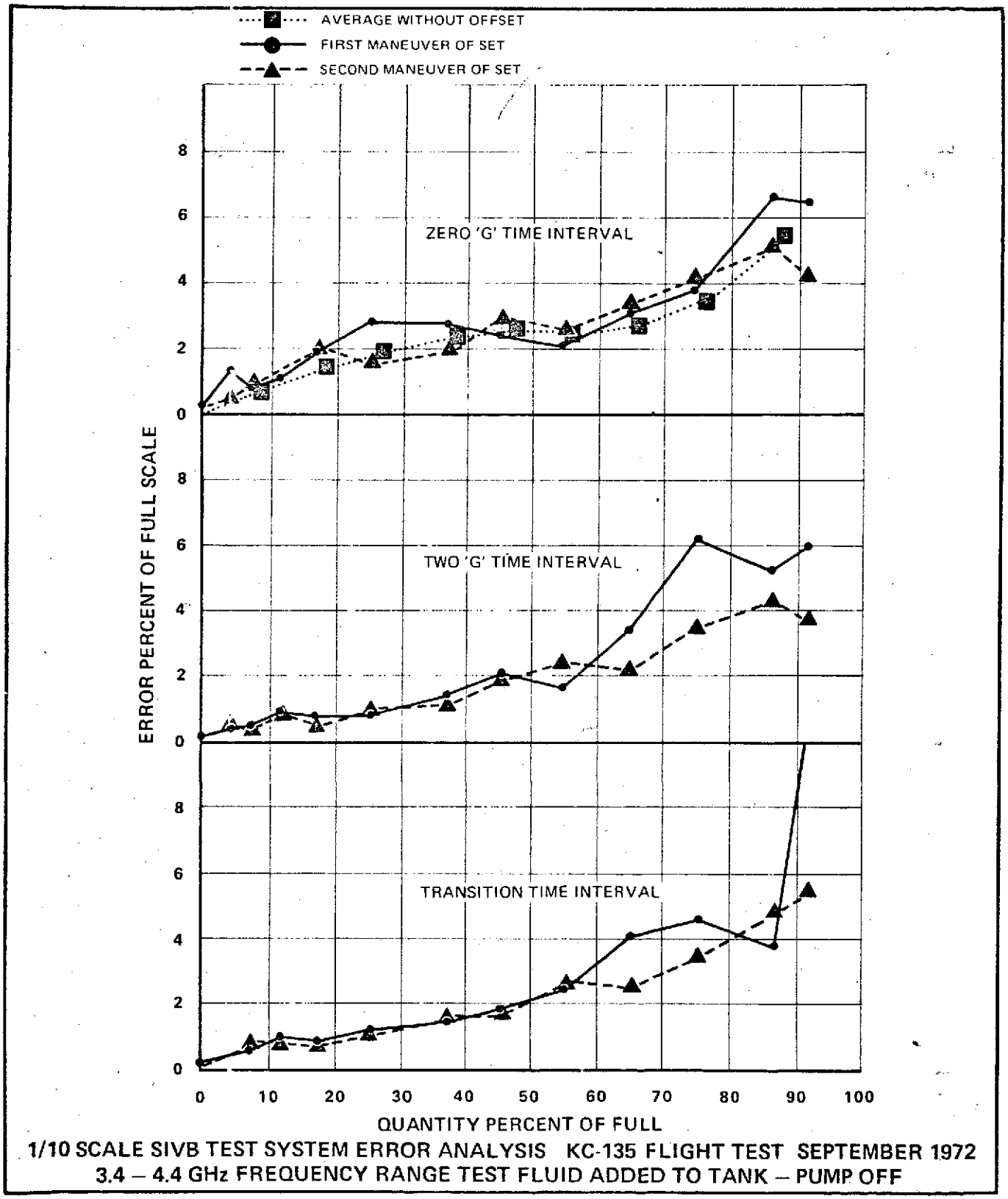


1/10 SCALE SIVB TEST SYSTEM ERROR ANALYSIS KC-135 FLIGHT TEST SEPTEMBER 1972
3.4 – 4.4 GHz FREQUENCY RANGE TEST FLUID ADDED TO TANK – PUMP OFF

Figure 3-10

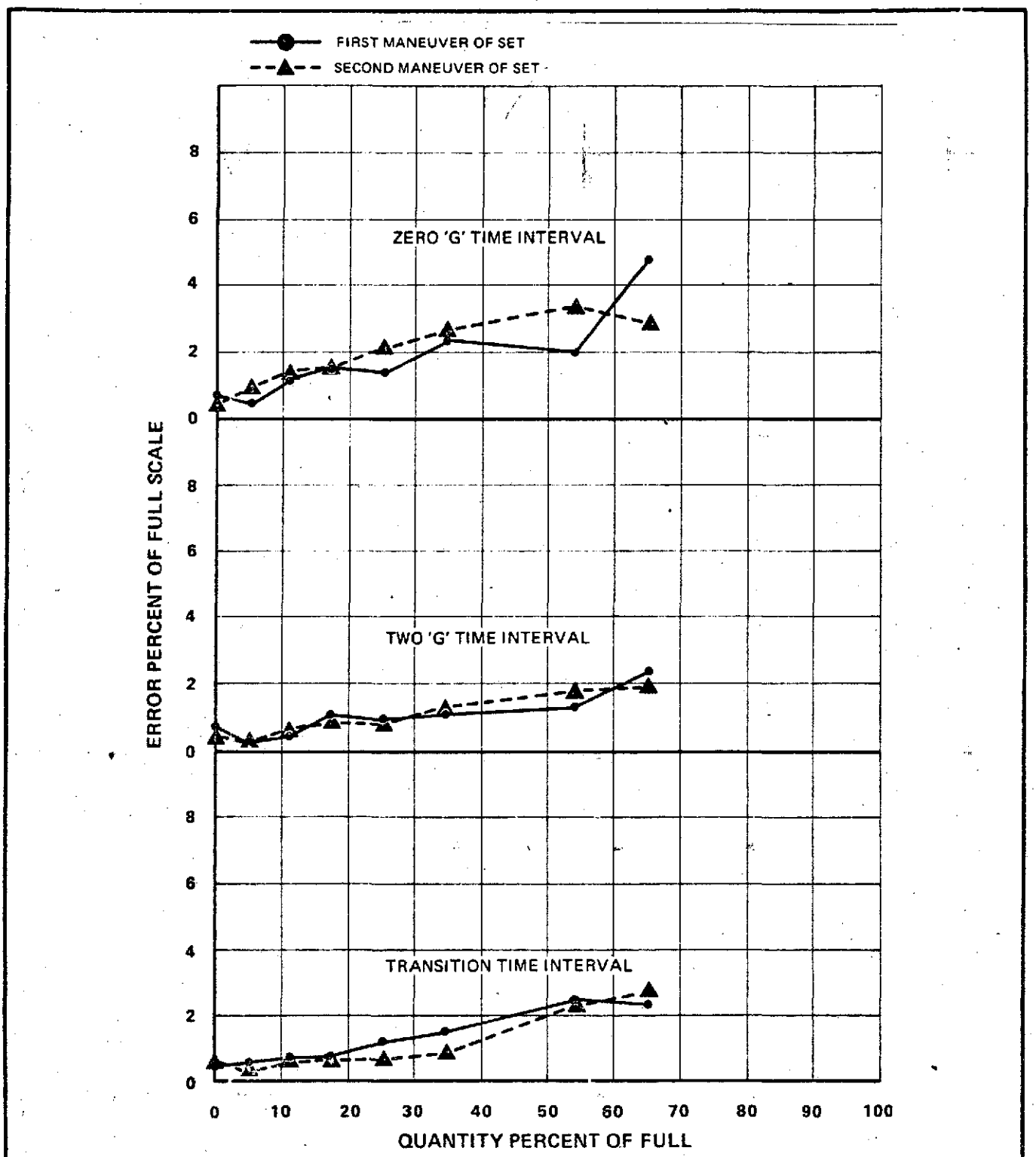


1/10 SCALE SIVB TEST SYSTEM ERROR ANALYSIS KC-135 FLIGHT TEST SEPTEMBER 1972
3.4 –4.4 GHz FREQUENCY RANGE TEST FLUID REMOVED FROM TANK – PUMP ON

Figure 3-11

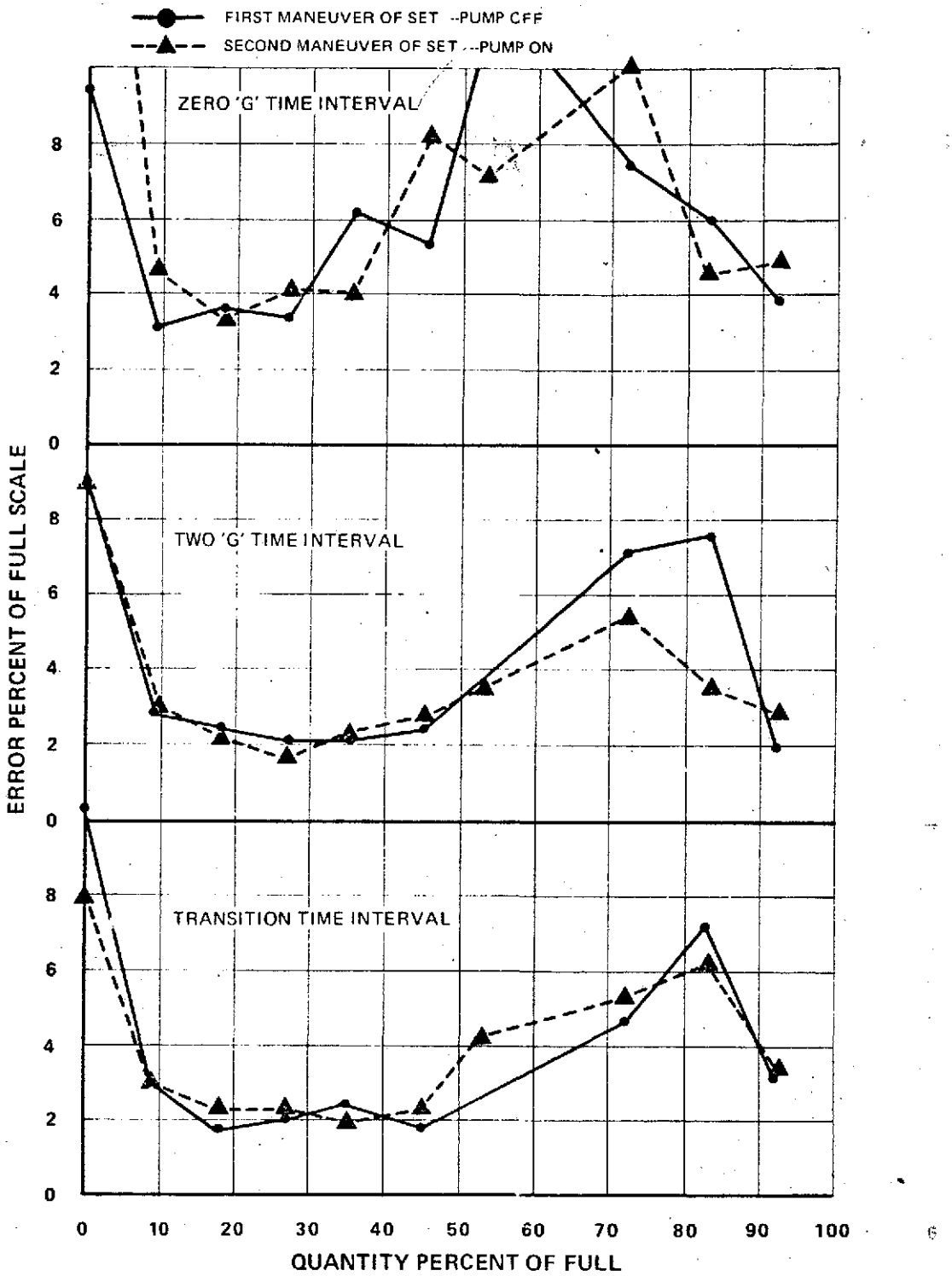


1/10 SCALE SIVB TEST SYSTEM ERROR ANALYSIS KC-135 FLIGHT TEST SEPTEMBER 1972
1.0 –2.0 GHz FREQUENCY RANGE TEST FLUID ADDED TO TANK

Figure 3-12

TABLE XI

TABULATED RESULTS FROM ERROR CALCULATIONS FOR

MANEUVERS NO. 1-44 (3.4 - 4.4 GHz)

| Maneuver No. | Approx. % Fill | Recirc. Pump | Zero 'G' Portion of Maneuver | | Two 'G' Portion of Maneuver | | Transition Portion of Maneuver | |
|---|---|---|---|---|---|---|---|---|
| | | | Worst Case Spread In Analog Output (Volts) | Calculated Mass Error In % | Worst Case Spread In Analog Output (Volts) | Calculated Mass Error In % | Worst Case Spread In Analog Output (Volts) | Calculated Mass Error In % |
| 1 | 0 | Off | .13 | 0.309 | .07 | .166 | .11 | .26 |
| 2 | 0 | " | .10 | 0.38 | .04 | .095 | .09 | .21 |
| 3 | 0 | " | N.A. | N.A. | N.A. | N.A. | N.A. | N.A. |
| 4 | 0 | " | N.A. | N.A. | N.A. | N.A. | N.A. | N.A. |
| 5 | 5 | " | .49 | 1.41 | .16 | .46 | .13 | .37 |
| 6 | 5 | " | .19 | 0.546 | .19 | .55 | .13 | .37 |
| 7 | 10 | " | .25 | 0.906 | .13 | .47 | .15 | .54 |
| 8 | 10 | " | .26 | 0.943 | .12 | .43 | .20 | .72 |
| 9 | 15 | " | .21 | 1.14 | .20 | .99 | .19 | .94 |
| 10 | 15 | " | .23 | 1.14 | .18 | .89 | .17 | .84 |
| 11 | 20 | " | .30 | 2.00 | .12 | .80 | .13 | .87 |
| 12 | 20 | " | .32 | 2.13 | .09 | .60 | .11 | .73 |
| 13 | 30 | " | .32 | 2.94 | .09 | .83 | .13 | 1.19 |
| 14 | 39 | " | .18 | 1.65 | .10 | .92 | .12 | 1.10 |
| 15 | 40 | " | .20 | 2.93 | .10 | 1.47 | .10 | 1.47 |
| 16 | 40 | " | .14 | 2.05 | .08 | 1.17 | .11 | 1.61 |
| 17 | 50 | " | .13 | 2.53 | .11 | 2.15 | .10 | 1.95 |
| 18 | 50 | " | .16 | 3.12 | .10 | 1.95 | .09 | 1.76 |
| 19 | 60 | " | .09 | 2.21 | .07 | 1.72 | .10 | 2.45 |
| 20 | 60 | " | .11 | 2.70 | .10 | 2.45 | .11 | 2.70 |
| 21 | 70 | " | .10 | 3.19 | .11 | 3.51 | .13 | 4.15 |
| 22 | 70 | " | .11 | 3.51 | .07 | 2.23 | .08 | 2.55 |
| 23 | 80 | " | .10 | 3.91 | .16 | 6.26 | .12 | 4.69 |
| 24 | 80 | " | .11 | 4.30 | .09 | 3.52 | .09 | 3.52 |
| 25 | 90 | " | .14 | 6.79 | .11 | 5.34 | .08 | 3.88 |
| 26 | 90 | " | .11 | 5.34 | .09 | 4.37 | .10 | 4.85 |
| 27 | 95 | " | .12 | 6.56 | .11 | 6.02 | .20 | 0.94 |
| 28 | 95 | " | .08 | 4.38 | .07 | 3.83 | .10 | 5.47 |
| 29 | 70 | On | .16 | 4.80 | .08 | 2.40 | .08 | 2.40 |
| 30 | 70 | " | .10 | 3.00 | .07 | 2.10 | .09 | 2.70 |
| 31 | 60 | " | .09 | 2.05 | .06 | 1.37 | .11 | 2.51 |
| 32 | 60 | " | .15 | 3.43 | .08 | 1.83 | .10 | 2.29 |
| 33 | 40 | " | .19 | 2.49 | .09 | 1.18 | .12 | 1.57 |
| 34 | 40 | " | .21 | 2.75 | .10 | 1.31 | .07 | .92 |
| 35 | 30 | " | .16 | 1.49 | .10 | .93 | .13 | 1.21 |
| 36 | 30 | " | .23 | 2.14 | .09 | .84 | .07 | .65 |
| 37 | 20 | " | .21 | 1.59 | .14 | 1.06 | .10 | .76 |
| 38 | 21 | " | .20 | 1.51 | .12 | .91 | .09 | .68 |
| 39 | 15 | " | .27 | 1.28 | .10 | .48 | .15 | .71 |
| 40 | 15 | " | .31 | 1.47 | .13 | .62 | .13 | .62 |
| 41 | 10 | " | .18 | 0.55 | .09 | .28 | .19 | .58 |
| 42 | 10 | " | .33 | 1.01 | .11 | .34 | .12 | .37 |
| 43 | 5 | " | .32 | 0.77 | .32 | .77 | .20 | .48 |
| 44 | 5 | " | .19 | 0.46 | .22 | .53 | .25 | .60 |

## 4.0 LARGE SCALE LOX TESTING

To substantiate the suitability of the RF mode counting technique in gauging liquid oxygen in very large tanks, tests were performed with a large tank at the NASA, MSFC, test facilities. (Test Cell 100, Building no. 4583). The following paragraphs detail the hardware and results of those tests.

## 4.1 SYSTEM DESCRIPTION

### 4.1.1 TANK CONFIGURATION

The tank in which the gauging tests were performed was a large stainless steel un-insulated tank with a fluid capacity of 69.26 $m^3$ (18,300 gallons). This tank as shown in Figure 4-1 stands upright to a height of approximately 11.6 meters (42.5 feet). The diameter of the tank is approximately 2.67 meters (8.75 feet).

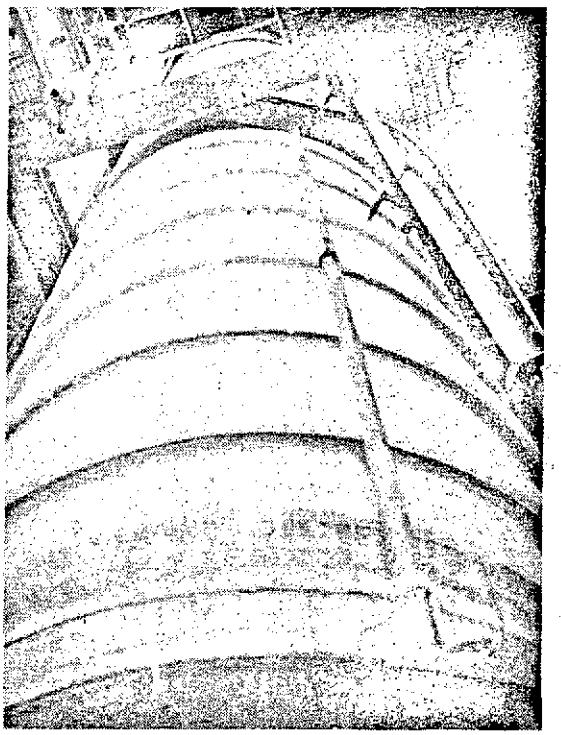

TEST CELL 100 LOX TANK
**Figure 4-1**

Figure 4-2 shows an inside view of the tank illustrating the presence of a large ladder-like structure running the full length of the tank.

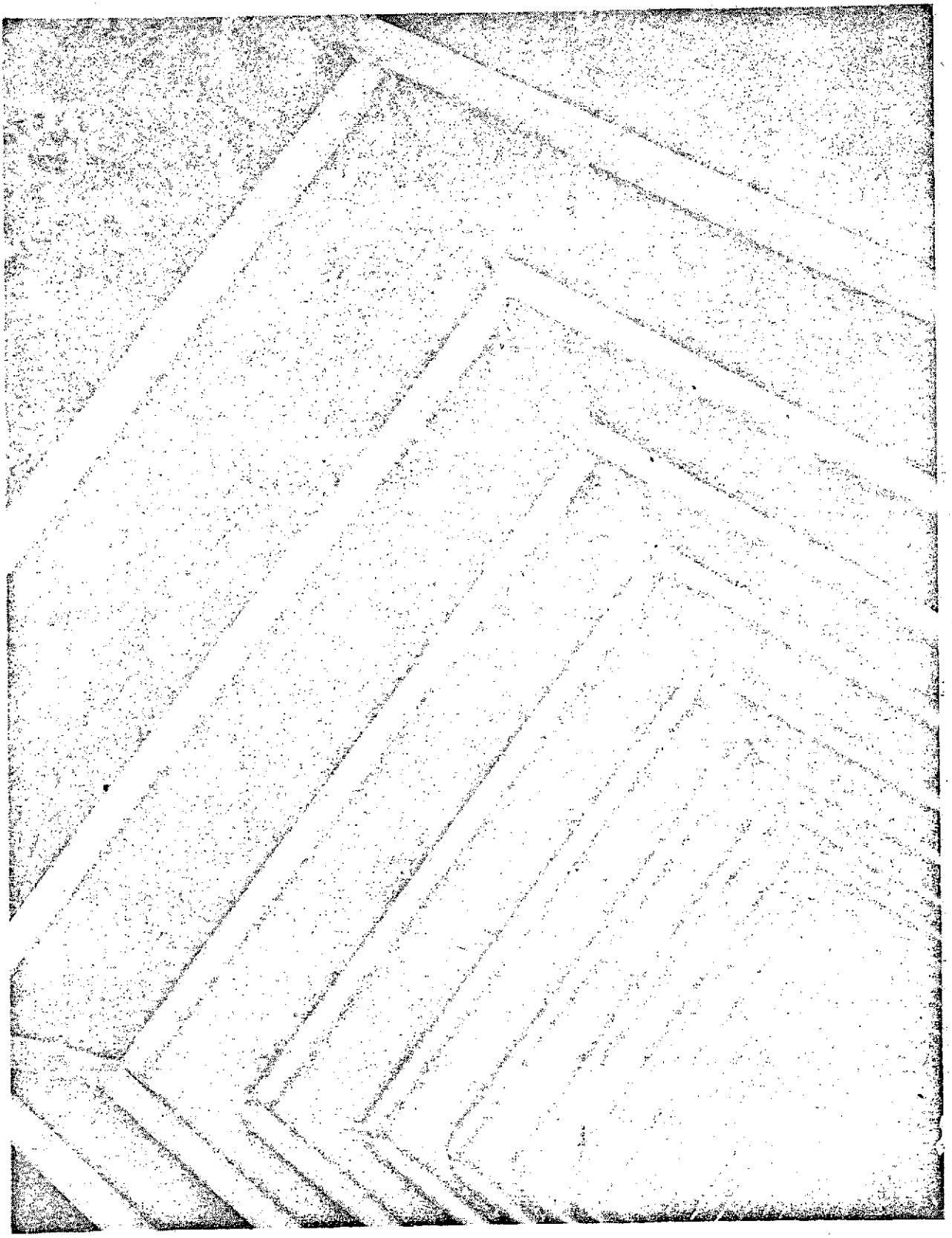

TANK INSIDE VIEW

Figure 4-2.

### 4.1.2 RF PROBE ASSEMBLY

The RF probe assembly is a multi-element structure which is used as a means of coupling RF energy into the tank in such a manner as to illuminate the entire volume of the tank with electromagnetic waves. This structure was secured to the larger access hatch flange located on the top of the tank. Each element (antenna) of the probe assembly contains a single RF radiation element consisting of a slender copper wire surrounded by a teflon cover (radome) as shown in Figure 4-3.

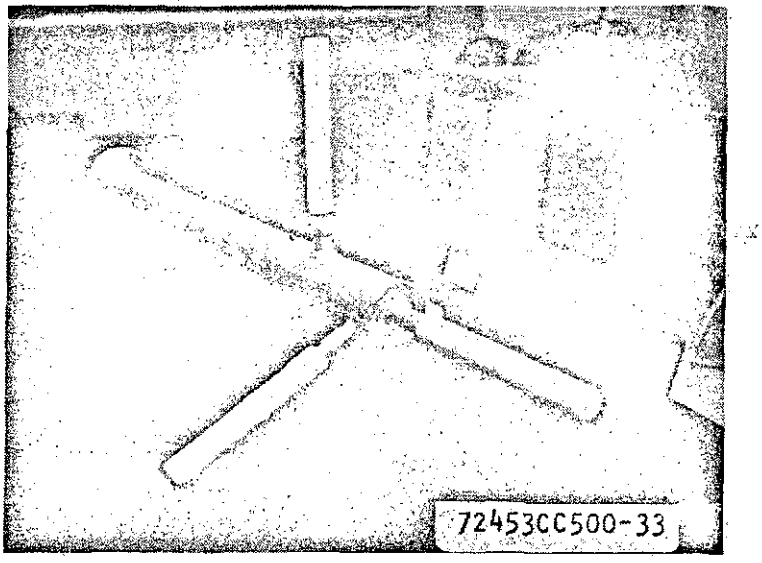


**RF PROBE ASSEMBLY FOR TEST CELL 100 TESTS**

**Figure 4-3**

SEMI-RIGID COAXIAL CABLES
FROM RF PROBE ASSEMBLY

**Figure 4-4**

Figure 4-4 shows the semirigid coaxial cables leading from the RF probe assembly after it was placed in the top of the test tank in an available access hatch.

### 4.1.3 TEST SYSTEM GAUGING ELECTRONICS

An RF lab type signal generator was used to establish the required RF energy for illumination of the tank interior. This generator was mounted in an enclosed nitrogen gas purged metallic container which was positioned at the top level of the test stand near the large access hatch and RF probe assembly.

The gauging system electronics used for detecting and processing the RF energy reflected from the tank was contained in a second enclosed metallic container. This enclosure contained an RF isolator, crystal detector, mode detector circuit, A solid-state SP4T pin-diode RF switch, a switch driver, a programmer, a mode count processor, and a digital-to-analog converter. The programmer, and switch driver are used in conjunction with the RF switch to multiplex sequentially between the four separate antenna elements located in the RF probe assembly. The mode count processor provides a digital (BCD) output indication of the number of detected resonant modes which is converted to an analog signal in a D/A converter. This analog signal was the primary system output.

Figure 4-5 shows both enclosures positioned on a I-beam immediately above the test tank.

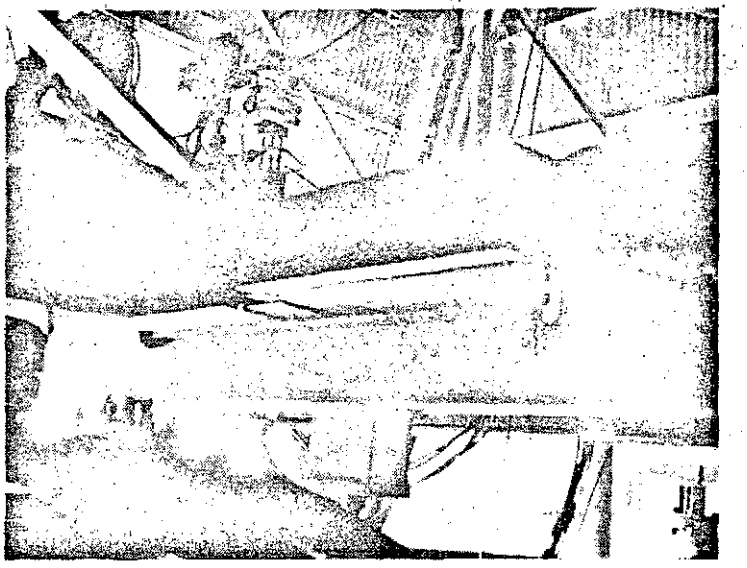

RF SIGNAL SOURCE AND PROCESSING ELECTRONICS ENCLOSURES

**Figure 4-5.**

### 4.1.4 TEST INSTRUMENTATION

To permit required correlation of actual LOX loading to that indicated by the RF system analog output a number of test parameter measurements were recorded during the tests. The instrumentation interface was arranged as illustrated in Figure 4-6. Blocks No. 1 and 2 designate NASA test monitoring and data recording which was utilized during the testing.

The NASA Analog/Digital Computer Data System was used to record the following parameters.

- RF system analog output (0-5 VDC).
- Tank ullage pressure.
- Propellant head pressure.
- Discrete-point propellant level indications (thermocouple sensors) at a minimum of 5 discrete points up the side of the tank.
- Temperatures in tank at both upper and lower ends of tank.
- Temperature in the Bendix gauging system electronics enclosure and also in the Bendix RF signal source enclosure.
- Also within the NASA computer data system an estimate of the liquid level from a $\Delta P$ type propellant utilization relationship was continuously calculated based on the propellant head pressure and tank ullage pressure information inputs.

## 4.2 PREDICTED GAUGING RESPONSE

The mathematical model which defines the number of resonant modes as a function of tank filling and other system variables was used to make a prediction of the gauging response shown in Figure 4-7. (See the November, 1972 Monthly Progress Report No. 43 for details of the gauging performance prediction for LOX in the Test Cell 100 tank). Superimposed over this graph is a plot of actual test data from the first test runs.

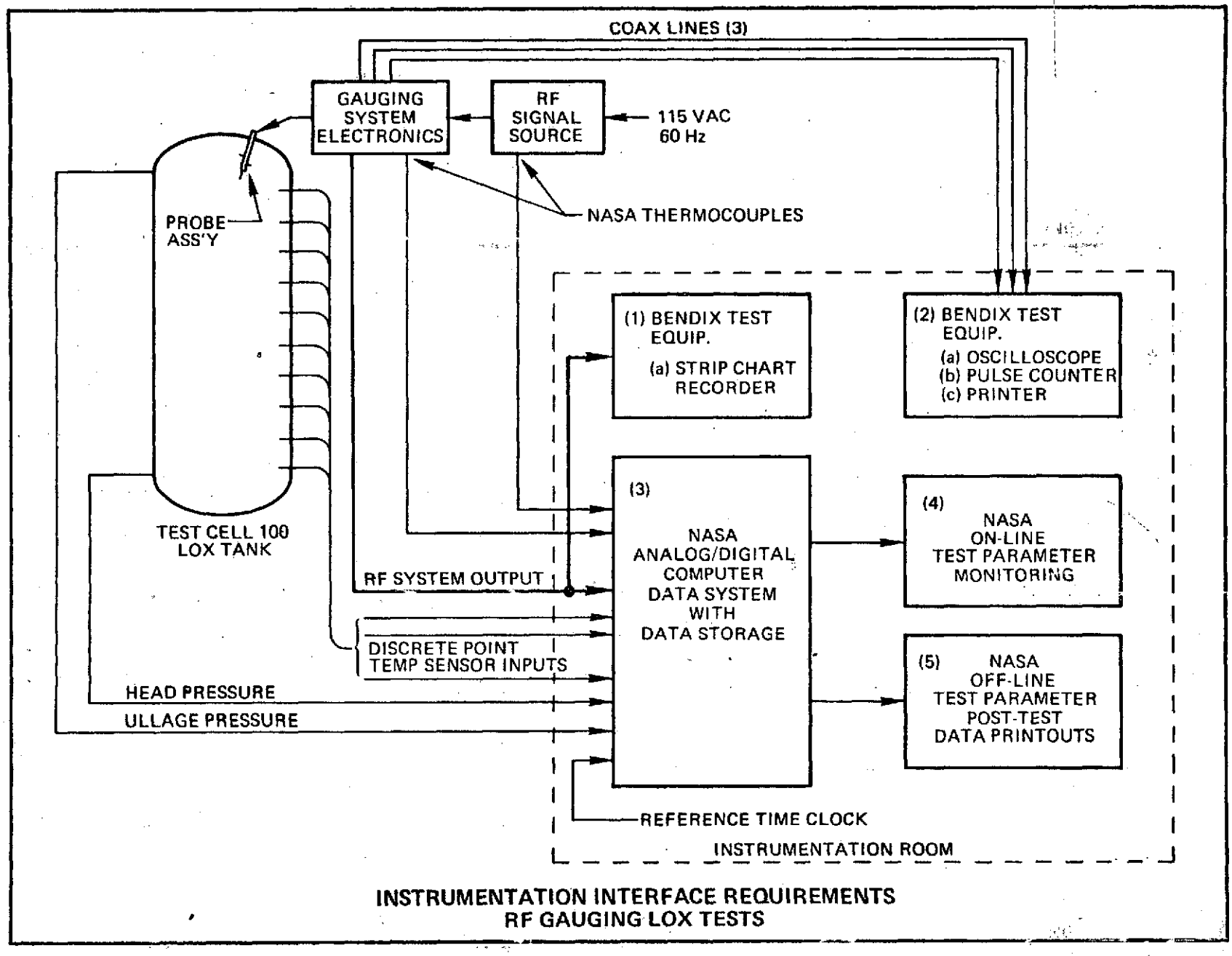
COAX LINES (3)
GAUGING SYSTEM ELECTRONICS
RF SIGNAL SOURCE
115 VAC 60 Hz
NASA THERMOCOUPLES
PROBE ASS'Y
TEST CELL 100 LOX TANK
(1) BENDIX TEST EQUIP.
(a) STRIP CHART RECORDER
(2) BENDIX TEST EQUIP.
(a) OSCILLOSCOPE
(b) PULSE COUNTER
(c) PRINTER
(3)
NASA ANALOG/DIGITAL COMPUTER DATA SYSTEM WITH DATA STORAGE
(4)
NASA ON-LINE TEST PARAMETER MONITORING
(5) NASA OFF-LINE TEST PARAMETER POST-TEST DATA PRINTOUTS
RF SYSTEM OUTPUT
DISCRETE POINT TEMP SENSOR INPUTS
HEAD PRESSURE
ULLAGE PRESSURE
REFERENCE TIME CLOCK
INSTRUMENTATION ROOM
INSTRUMENTATION INTERFACE REQUIREMENTS
RF GAUGING LOX TESTS

Figure 4-6

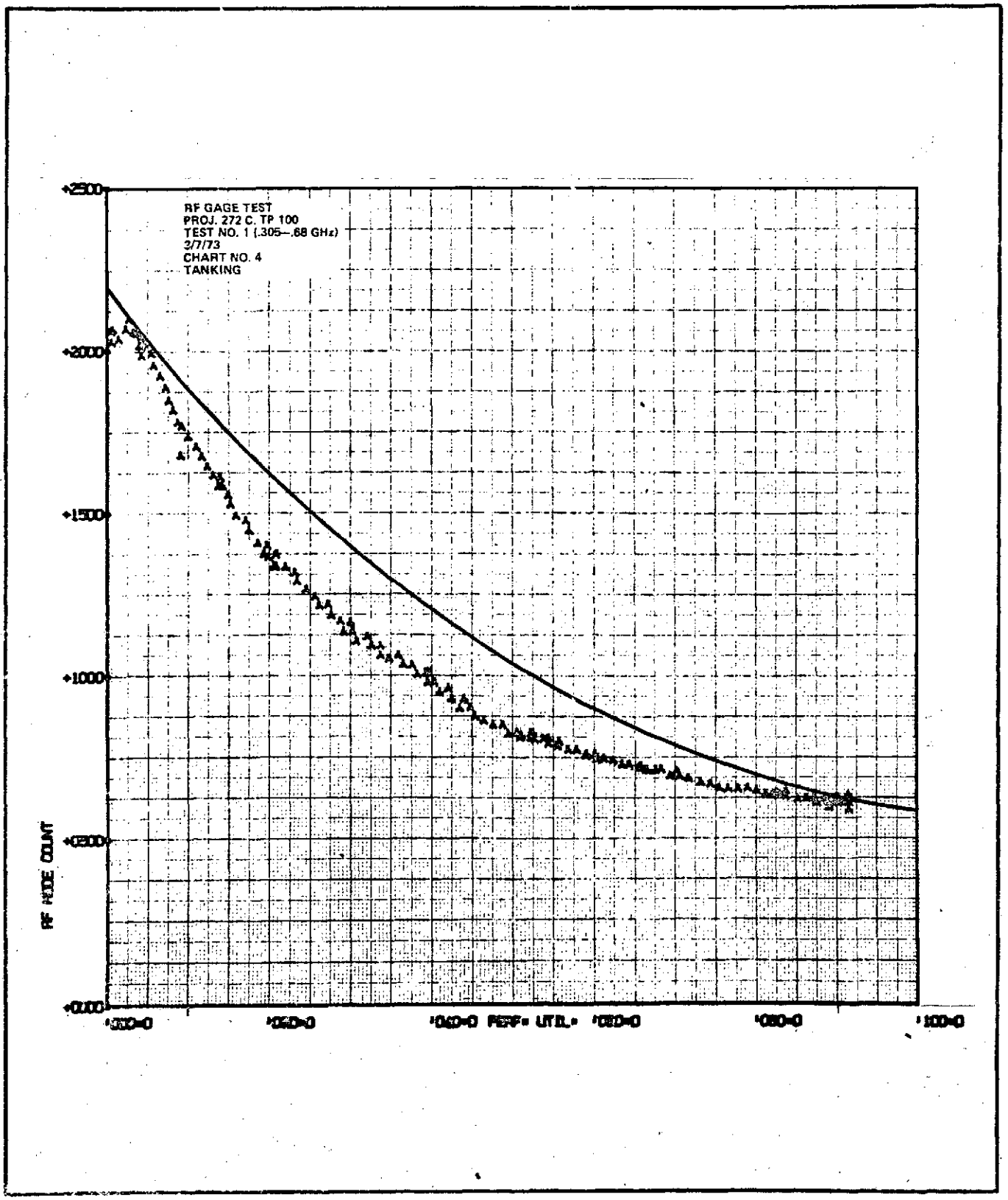
RF GAGE TEST
PROJ. 272 C. TP 100
TEST NO. 1 (.305—.68 GHz)
3/7/73
CHART NO. 4
TANKING
+2500
+2000
+1500
+1000
+0000
RF MODE COUNT
PERF. UTIL.

Figure 4-7

## 4.3 SYSTEM PERFORMANCE

The LOX testing consisted of three separate test runs where during each test run the tank was filled to approximately 90% of its capacity and then emptied. The RF gauging system's operating frequency band was adjusted between test runs permitting testing with three RF frequency bands. During the first test run the predicted optimum frequency band of .305 - .68 GHz was used. During the second and third respective test runs, the RF frequency bands were shifted to cover .25 - .55 GHz and .305 - .68 GHz.

Plots of the more significant data as compiled and plotted off-line by the Test Cell 100 computing facility are presented in Volume II of this report. (Bendix Publication No. 7247).

Table XII contains a summary of the off-line data plots and significant identifying information for each plot.

Examination of these data plots reveals the following:

1. The RF gauging technique can provide a gaugable loading response with liquid oxygen in a large tank.

2. The predicted RF frequency band (.305 - .68 GHz) in Test No. 1 provided the better overall characteristic gauging curve.

# TABLE XII

## CHART IDENTIFICATION SUMMARY - LOX TESTS

## TEST CELL 100 RF GAUGING TESTS

| Test No. | Freq. Range in GHz | Chart No. | Page No. | Test Event | Data Plotted | Time Frame In Seconds | |
|---|---|---|---|---|---|---|---|
| 1. | .305 - .68 | 1 | A-1 | Pre-Test Data | RF Output vs. Time | TI=58 | T2=728 |
| | | 2 | A-2 | Tanking with LOX | RF Output vs. Time | TI=940 | T2=4900 |
| | | 3 | A-3 | Tanking with LOX | PU Output vs. Time | TI=840 | T2=4900 |
| | | 4 | A-4 | Tanking with LOX | RF Output vs. PU Output | TI=840 | T2=4900 |
| | | 8 | A-5 | Tanking approx. 90% full | RF Output vs. Ullage Pressure | TI=6052 | T2=6378 |
| | | 9 | A-6 | De-tanking | RF Output vs. Time | TI=6378 | T2=9678 |
| | | 10 | A-7 | De-tanking | RF Output vs. Time | TI=6378 | T2=9678 |
| | | 11 | A-8 | De-tanking | RF Output vs. PU Output | TI=6378 | T2=9678 |
| 2. | .25 - .55 | 2 | A-9 | Tanking with LOX | RF Output vs. Time | TI-450 | T2=4606 |
| | | 3 | A-10 | Tanking with LOX | RF Output vs. Time | TI=450 | T2=4606 |
| | | 4 | A-11 | Tanking with LOX | RF Output vs. PU Output | TI=450 | T2=4606 |
| | | 6 | A-12 | De-tanking | RF Output vs. Time | TI=5546 | T2=8772 |
| | | 7 | A-13 | De-tanking | RF Output vs. Time | TI=5546 | T2=8772 |
| | | 8 | A-14 | De-tanking | RF Output vs. PU Output | TI=5546 | T2=8772 |
| 3. | .305 - .68 | 2 | A-15 | Tanking with LOX | RF Output vs. Time | TI=378 | T2=4198 |
| | | 3 | A-16 | Tanking with LOX | PU Output vs. Time | TI=378 | T2=4198 |
| | | 4 | A-17 | Tanking with LOX | RF Output vs. PU Output | TI=378 | T2=4198 |
| | | 6 | A-18 | De-tanking | RF Output vs. Time | TI=5356 | T2=8640 |
| | | 7 | A-19 | De-tanking | RF Output vs. Time | TI=5356 | T2=8640 |
| | | 9 | A-20 | De-tanking | RF Output vs. PU Output | TI=5356 | T2=8640 |

## 5.0 CRYOGENIC TESTING UTILIZING A SCALE SPACE SHUTTLE TANK

To evaluate the RF gauging system with the cryogens LOX and $LH_2$, a dual walled vacuum insulated vessel was fabricated. The vessel was modeled after a space shuttle cryogenic storage tank. Testing of the RF Gauge was accomplished by placing the cryo tank in a gimbaling fixture and performing both static and dynamic orientation tests at various fill levels with both LOX and $LH_2$.

## 5.1 DESIGN FABRICATION AND ASSEMBLY OF THE CRYOGENIC TANK

The test tank fabricated in Phase B consists of an inner pressure vessel and an outer vacuum shield vessel which was mounted to a gimbal mechanism. The inner pressure vessel included two end hemispheres, a cylindrical center section, an access hatch and the hatch cover. These components are shown in Figures 5-1, 2, 3 and 4 respectively. The assembled pressure vessel is shown in Figure 5-5 and 5-6. Upon assembly of the pressure vessel it was filled with water and subjected to and passed a 100 psig proof pressure test. The pressure vessel was then evacuated to a pressure of $8 \times 10^{-6}$ torr with no detectable leaks.

The outer vessel includes a cylindrical section, end hemispheres and an access hatch. These components are shown in Figures 5-7, -8 and -9 respectively.

The cylindrical section of the outer shell was supported by the orientation test fixture as shown in Figure 5-7. The assembling of the pressure vessel to the outer shell was done in the following steps: The pressure vessel was first wrapped with sheets of aluminized mylar and suspended in the outer shell cylinder, then it was filled with water to check the suspension system. No appreciable movement in the inner pressure vessel related to the outer vessel cylinder shell was noted. The pressure vessel was dried out and the outer vessel hemispheres were welded in place.

The space between the inner pressure and the outer vacuum shield was evacuated for leak testing. After the leak test was performed, several small leaks in the vacuum jacket were detected and subsequently repaired. The test tank was then connected back to the vacuum pump and hot nitrogen gas was forced in the pressure vessel fill line and vented out of the pressure vessel vent line to heat up the tank assembly during the evacuation process. Additional heating was provided by external heat lamps where the tank and lamps were covered by sheets of aluminized mylar. The internal temperatures in the test tank during this evacuation process were maintained at approximately 200° F. To assure that all gases and vapors were driven from the internal surfaces, the vacuum bake-out process was utilized. The pressure reading in the evacuated region was indicated as $8 \times 10^{-6}$ torr.

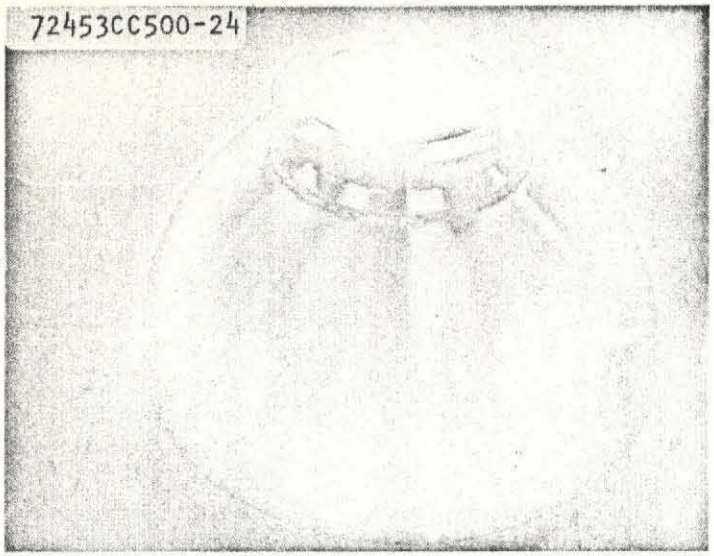


Figure 5-1. END HEMISPHERE

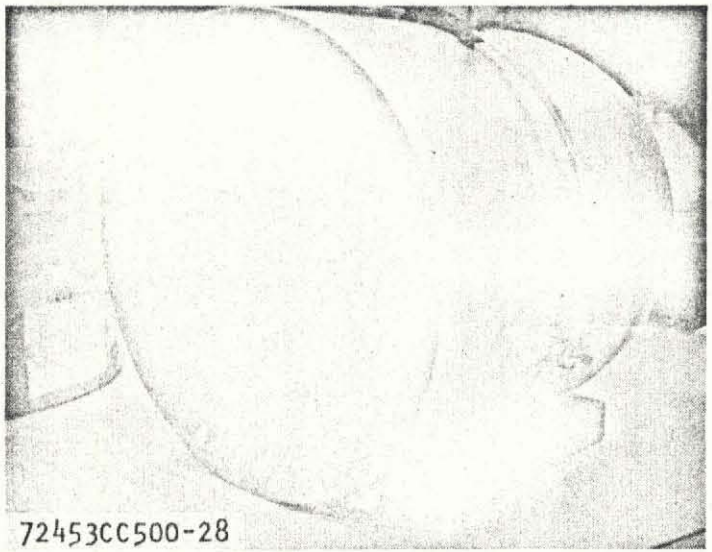


Figure 5-2. CYLINDRICAL CENTER SECTION

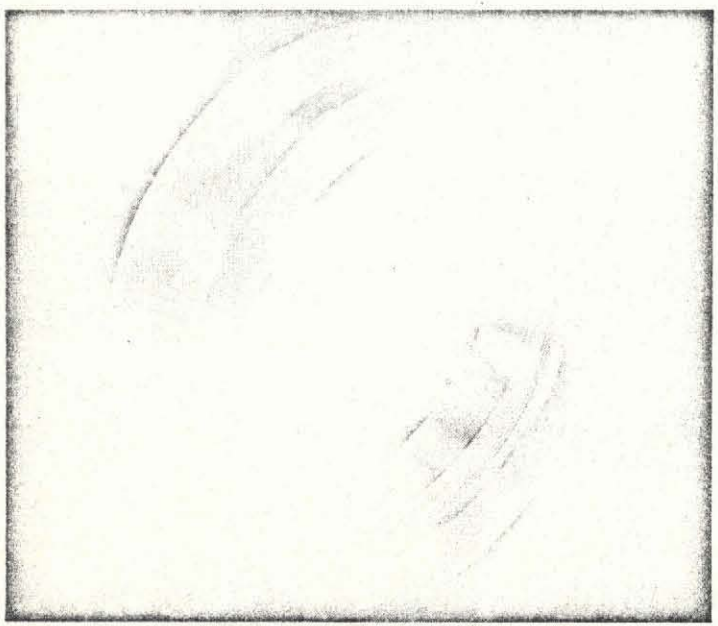

Figure 5-3. ACCESS HATCH FLANGE

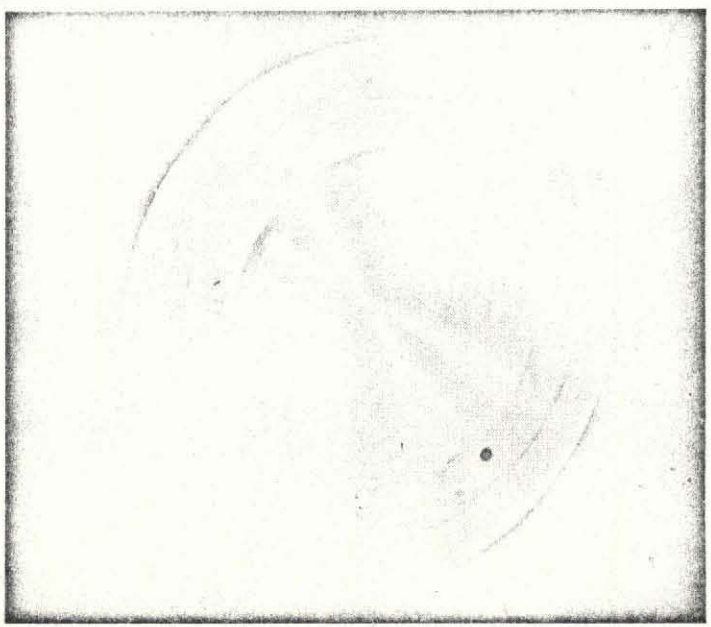

Figure 5-4. ACCESS HATCH COVER

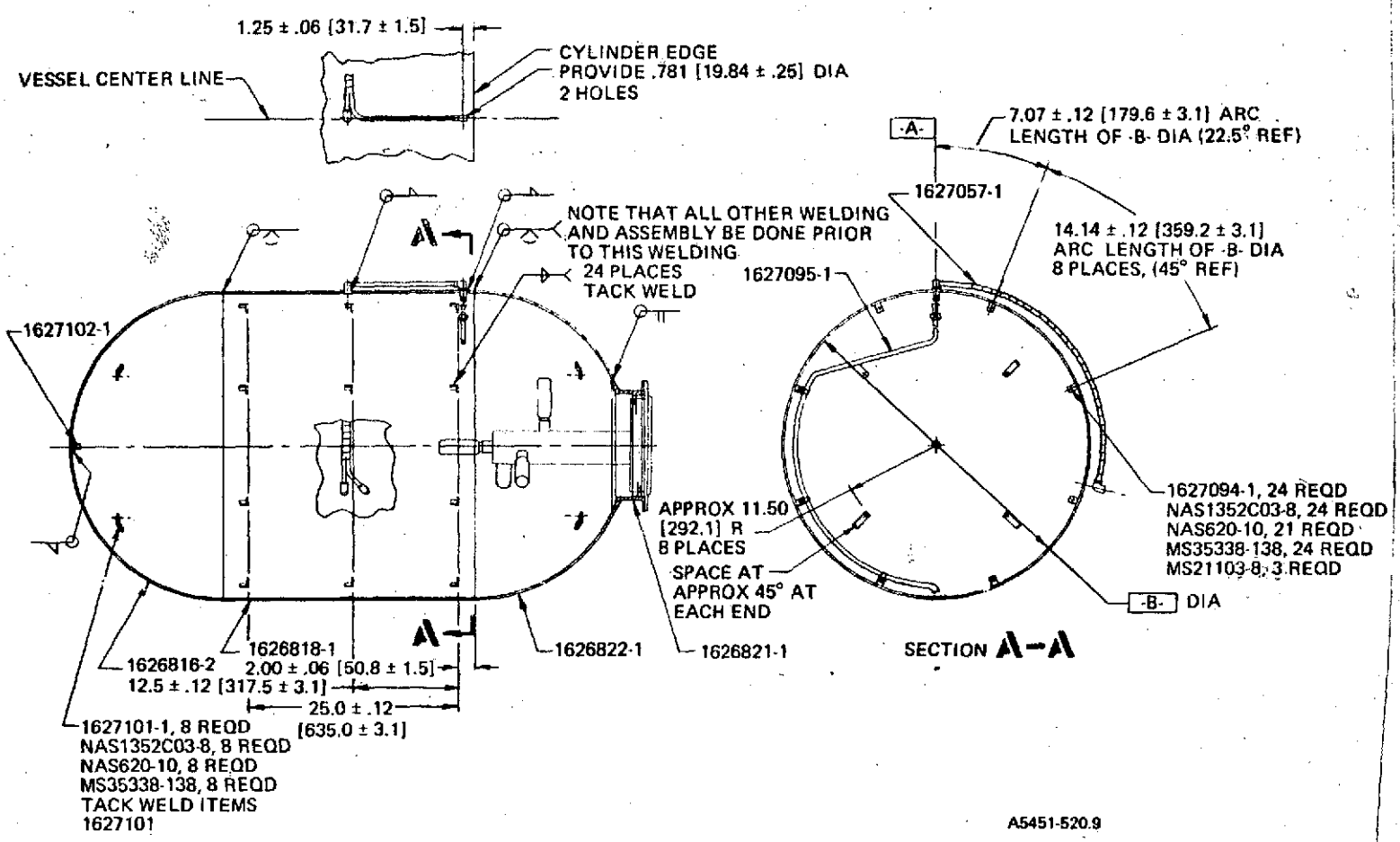


**PRESSURE VESSEL ASSEMBLY**

Figure 5-5

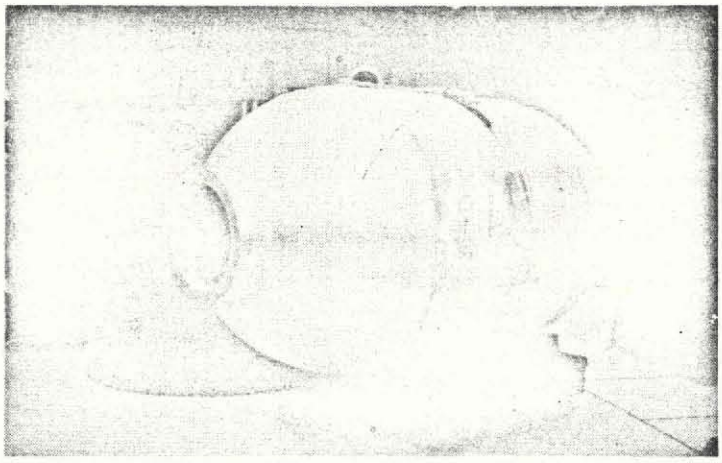

COMPLETED PRESSURE VESSEL

Figure 5-6.

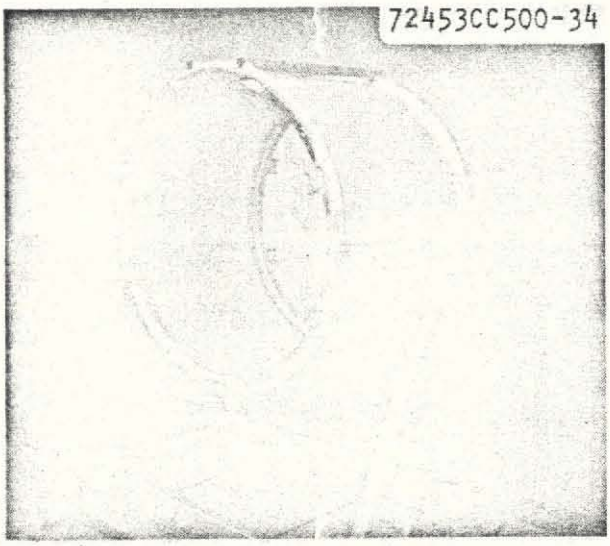


Figure 5-7. CYLINDRICAL SECTION

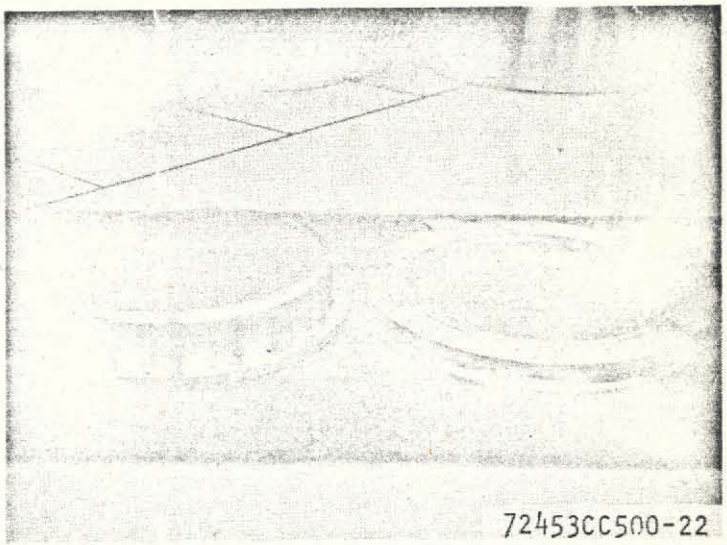


Figure 5-8. OUTER VESSEL ACCESS HATCH COVER AND FLANGE

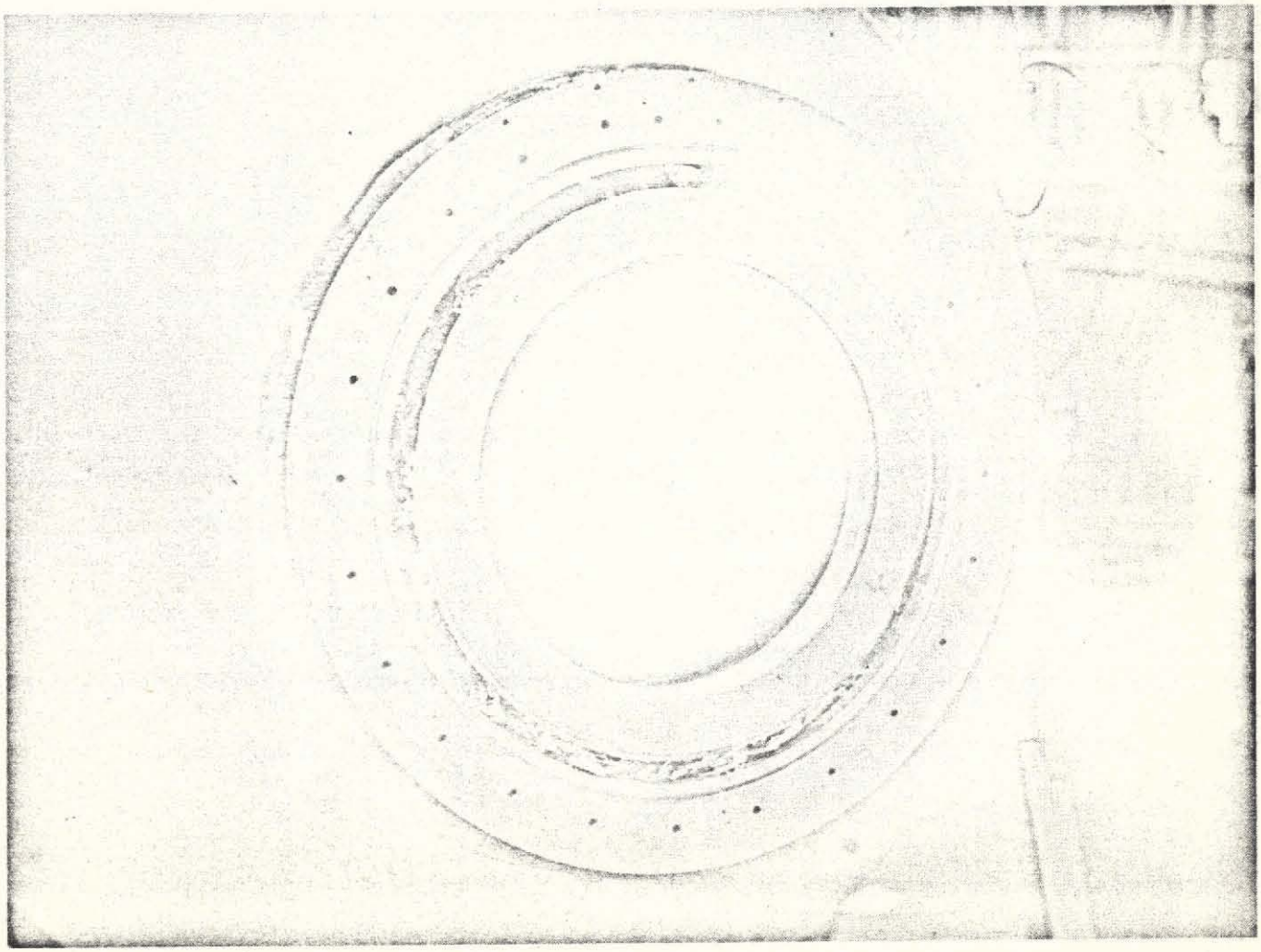

Figure 5-9. ACCESS HATCH-INNER AND OUTER VESSEL

## 5.2 RF ANTENNA ASSEMBLY

The antenna used in the cryogenic test tank is a multi-element RF probe. (See Appendix A for discussion of multi-element RF probe.) This probe design incorporates four radiation elements attached to a support tube that is mounted directly to the inner side of the pressure vessel access hatch cover. Figure 5-10 shows the RF probe assembly.

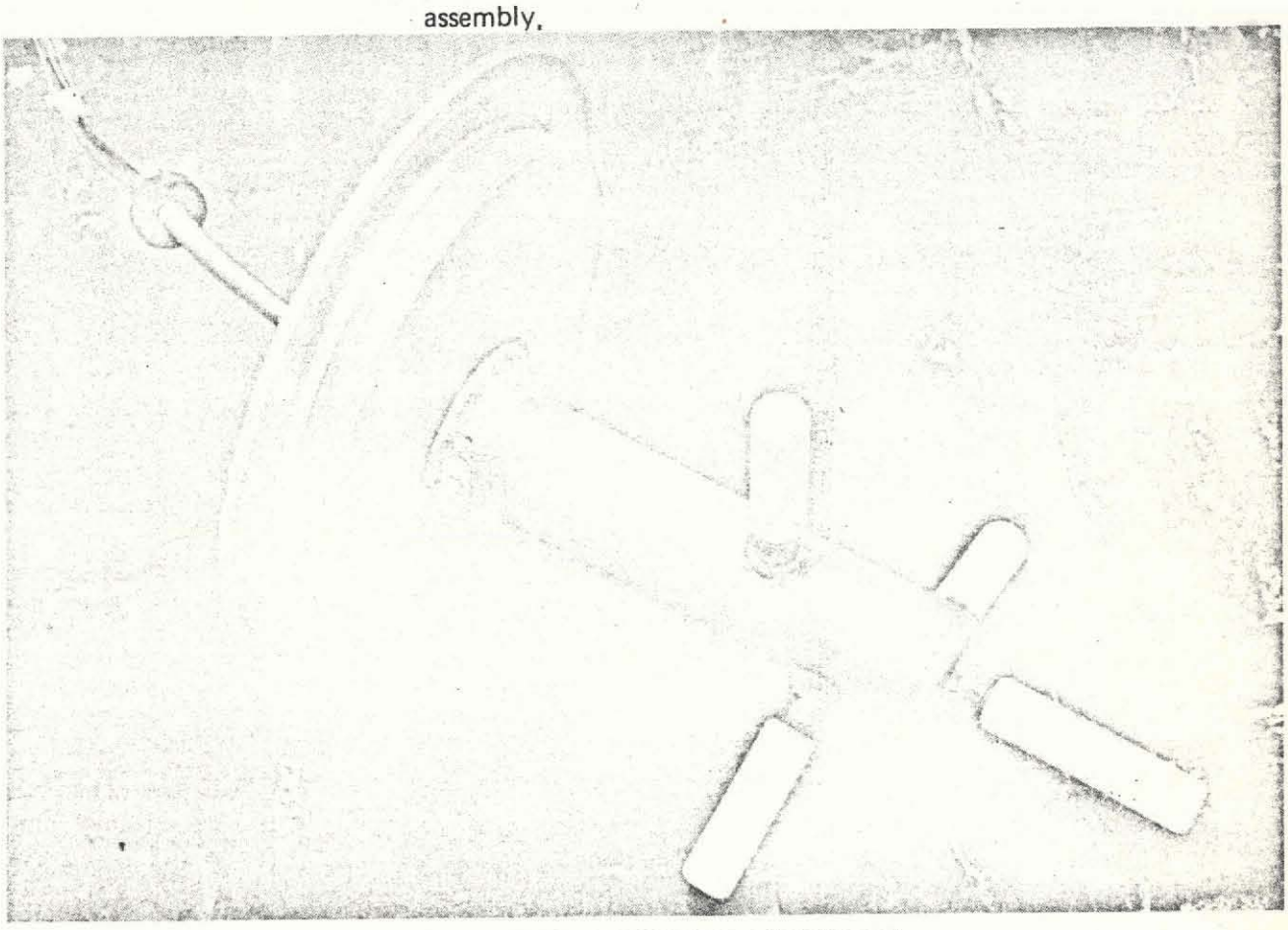

Figure 5-10. RF PROBE ASSEMBLY

## 5.3 GIMBALING MECHANISM

The cryogenic tank was mounted in a gimbaling fixture as shown in Figure 5-11. This fixture contains a remotely controlled gimbaling mechanism which is capable of rotating the dewar when filled with either test cryogen, 180° in either direction from a horizontal position about the minor axis of the dewar. When stopped in any position, the dewar remains in that position without any creep or measurable back- lash. Rotation of the test tank is accomplished by means of a reversible electric motor with a chain and sprocket drive. A remote indication of the angular position of the test tank is provided by means of a potentiometer, the voltage established at the potentiometer wiper contact is directly proportional to the angular position of the test tank.

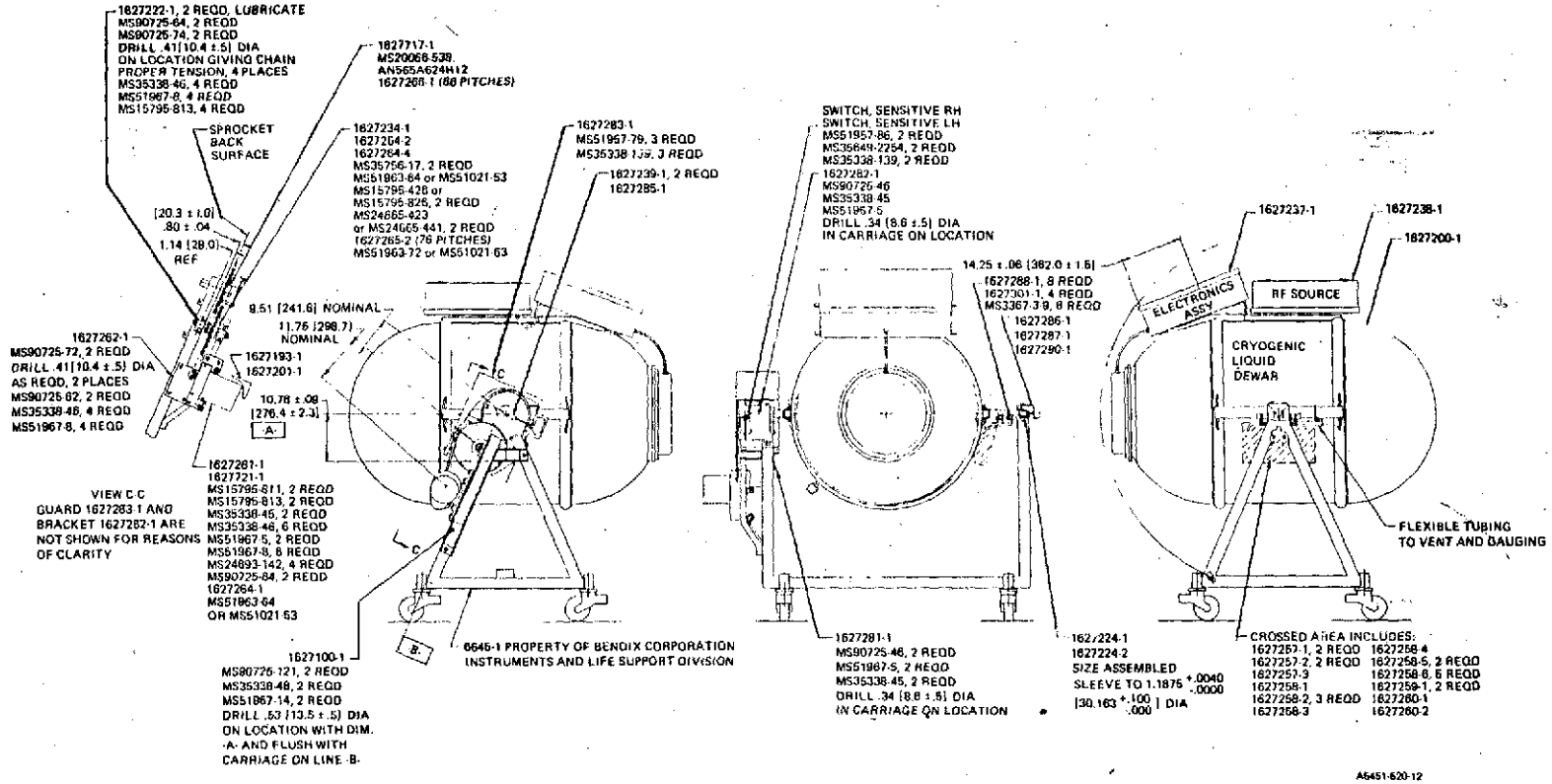


**TANK AND GIMBALING FIXTURE**

**Figure 5-11**

An additional component was added to prevent any appreciable creep or movement in the tank gimbaling mechanism; this is a pneumatically actuated brake system.

## 5.4 CRYOGENIC FLUID TRANSFER SYSTEM

Due to the inherent hazards associated with the test fluids, liquid oxygen and liquid hydrogen, the cryogenic test tank and support fixture were positioned in a concrete hazard test cell. To assure safe handling of the cryogenic test fluids, liquid transfers and tank orientation were remotely controlled from an instrumentation building that contained all control and monitoring equipment. Figure 5-12 shows the test system fluid transfer schematic. This configuration for a test fluid transfer setup provided a safe means to both fill and empty cryogenic liquid dewar.

Valves V4, V5, V6 and V7 are electrically operated solenoid valves. Pressure relief valve RV1 relieves at $10.334 \times 10^5$ newton/$m^2$ where the pressure relief valves RV2 and RV3 relieve at 3.447 newton/$m^2$. The pressure in both the storage tank and the dewar will be sensed with pressure transducers PT1 and PT2, respectively. The vacuum pump is used to pull any residual gases out of the test tank.

## 5.5 RF GAUGING SYSTEM ELECTRONICS

The electronic functions required to establish and detect the presence of resonant modes and to provide a digital mode count output are as shown in the block diagram of Figure 5-13. The RF energy source used was a standard laboratory RF generator mounted on the test tank in an enclosure which was continuously purged with nitrogen gas. The RF signal processing electronics were packaged within a second nitrogen gas purged enclosure which also was mounted on the test tank as shown in Figure 5-14.

In addition to an RF isolator, crystal detector, and a mode detector circuit, the breadboard processing electronics package contained a solid- state SP4T pin-diode RF switch, a programmer and switch driver and a mode count processor. The programmer and switch driver are used in conjunction with the RF switch to multiplex sequentially between four separate antenna elements located in the RF probe assembly. The mode count processor provides a digital (BCD) output indication of the number of detected resonant modes.

## 5.6 TEST INSTRUMENTATION

For the LOX and $LH_2$ tests performed, the test article, the test control functions, and the instrumentation hardware were physically arranged as illustrated in Figure 5-14. The test tank, the gauging system electronics and an RF energy source were positioned

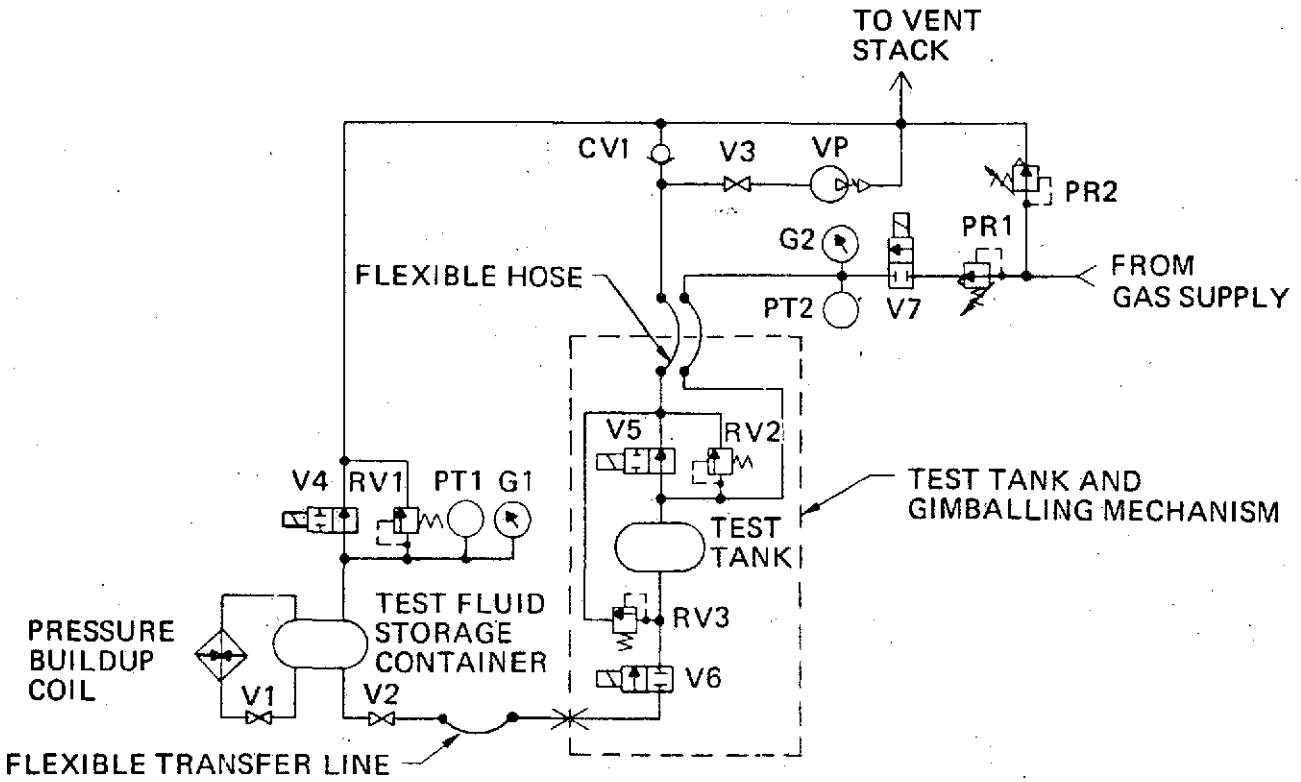


FLUID TRANSFER SCHEMATIC

5451-520.3

Figure 5-12

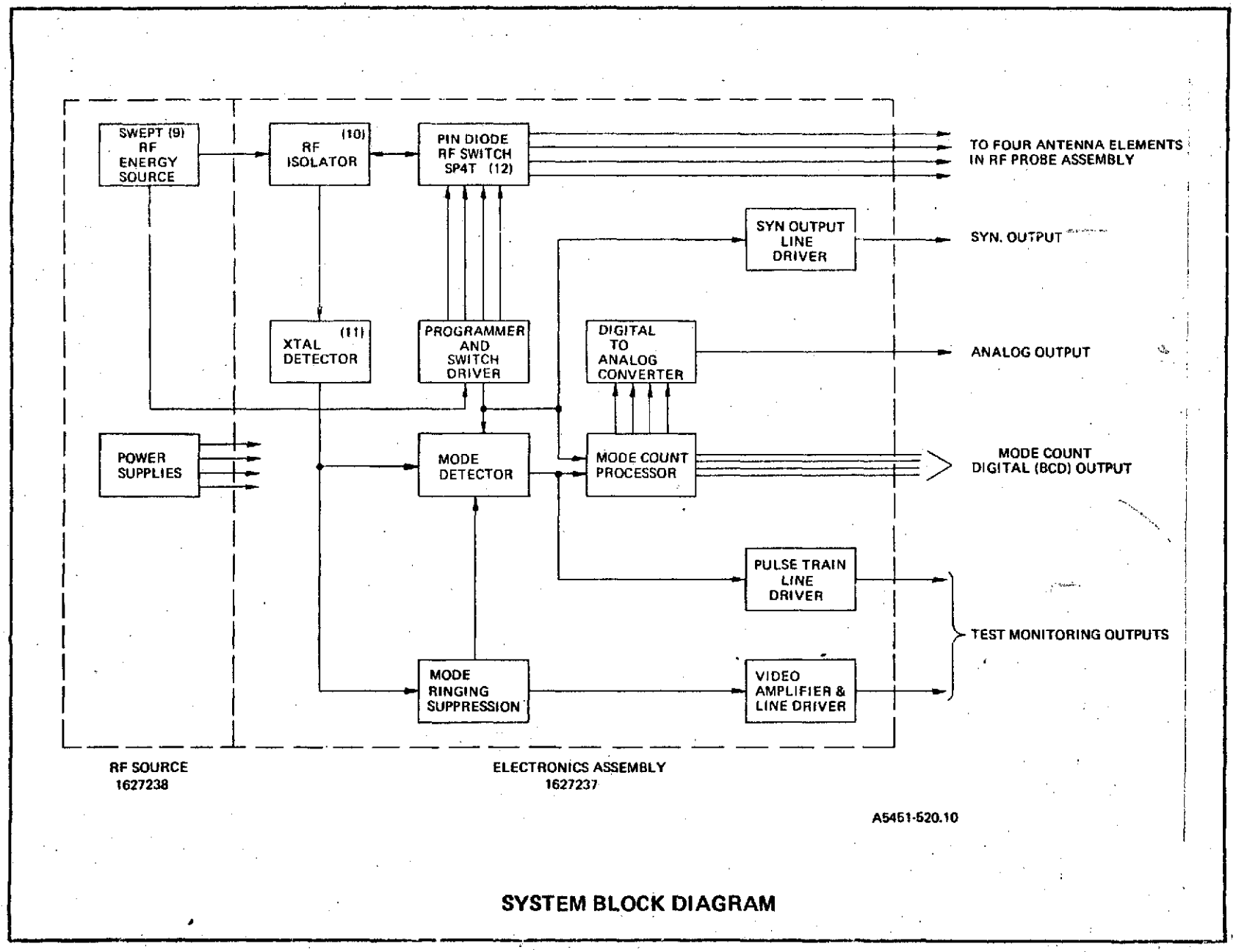


**SYSTEM BLOCK DIAGRAM**

**Figure 5-13**

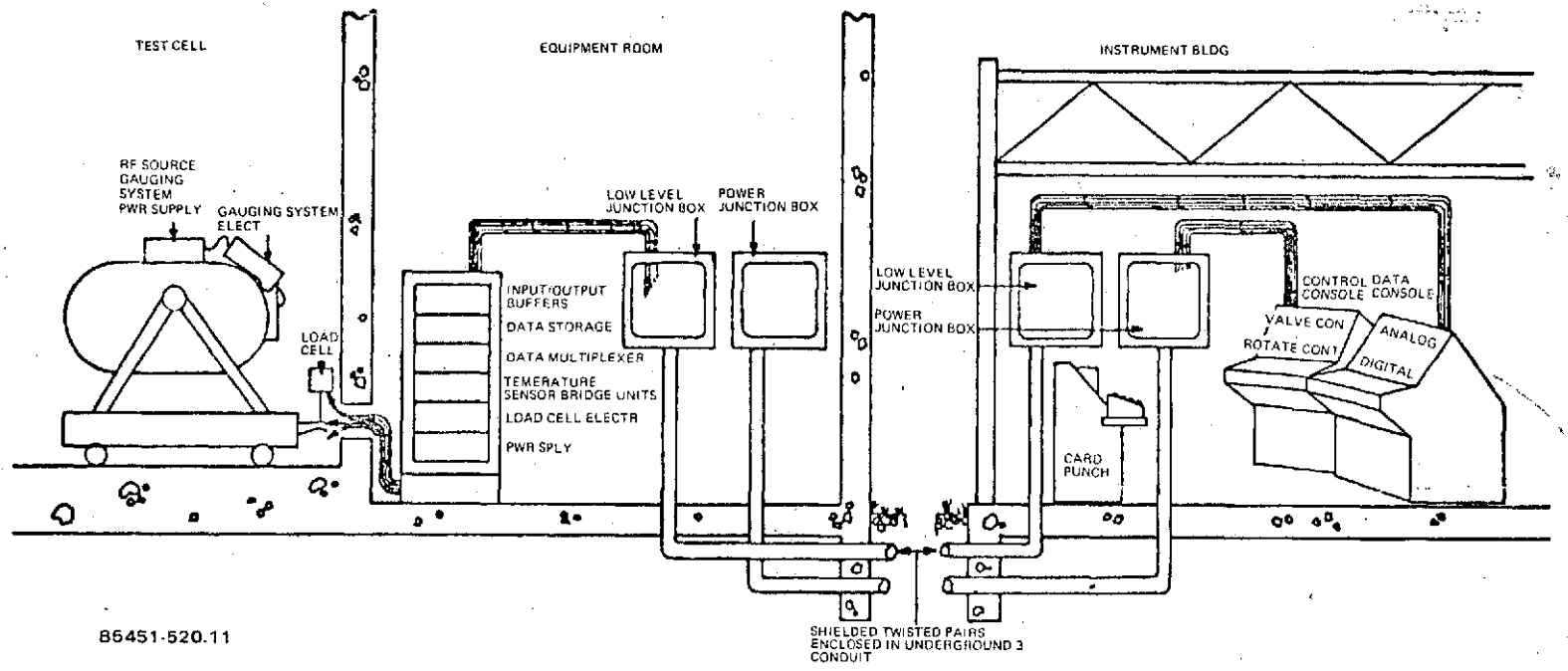


**INSTRUMENTATION TEST SETUP**

**Figure 5-14**

on a scale platform located in the test cell. An equipment room adjacent to the test cell served to link together electrically the test control mechanisms in the test cell with the test control panels in the remote instrumentation building. The equipment room contained signal conditioning equipment for the scale load cell, the tank temperature transducers, and the tank pressure transducers. The equipment room also contained multiplexing equipment to sample and transmit data from the test site to the instrumentation building. Control and data monitoring consoles were located in the remote instrumentation building. To facilitate the rapid acquisition of a large quantity of data, an automatic data acquisition system provided the appropriate interface between data outputs and an IBM Model 026 modified keypunch. Figure 5-15 shows a block diagram of the basic test instrumentation setup which was used to record all test data.

## 5.7 LOX ORIENTATION TESTS

The LOX tests were performed in a scale space shuttle cryo test tank. The test tank positioned on the gimbaling fixture located in the hazard test cell is shown in Figure 5-16. The raw data parameters of mode count, mass, tank pressure, rotational angle, and temperature of the test were recorded utilizing a data acquisition system which automatically punched the data on IBM cards. This included data taken over several days of testing giving 6000 IBM cards and 42,000 data points. During the orientation tests, some modifications to the RF Gauging system were necessary. Some of the problems which occurred during the orientation tests were the effects of the loose wires in the vessel and the PRT's acting as antennas causing ringing in the output data. However, these problems were solved and the LOX tests were continued. The test tank was initially filled and drained with LOX to achieve tank cooldown followed by orientation tests. The orientation tests consisted of continuous rotation of the test tank from -180° to 180° at a rate of 6 degrees/second. Orientation tests were performed at 5% fill increments with data recorded continuously during rotation of the test tank. The mode count and LOX mass relation obtained from the orientation tests gives a nonlinear curve shown in Figure 5-17. Figure 5-18 shows this test data superimposed over a graph of the predicted loading response.

### 5.7.1 LOX DATA ANALYSIS

The data was first analyzed to obtain a nonlinear regression curve of mean mass and mean mode count. At each fill level the raw data was used to generate:

- Mean mode count and variance
- Mean mass and variance

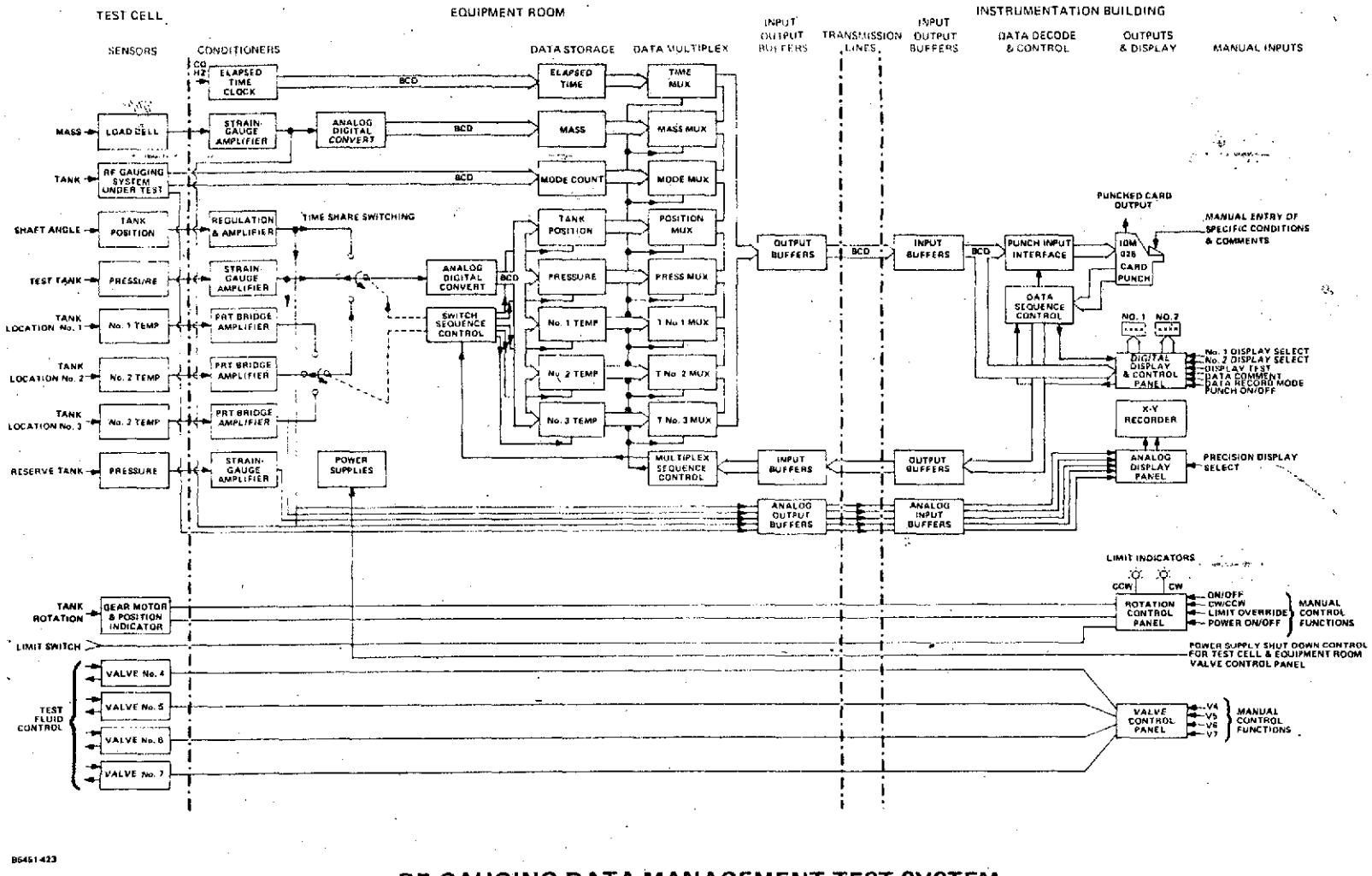


**RF GAUGING DATA MANAGEMENT TEST SYSTEM**

**Figure 5-15**

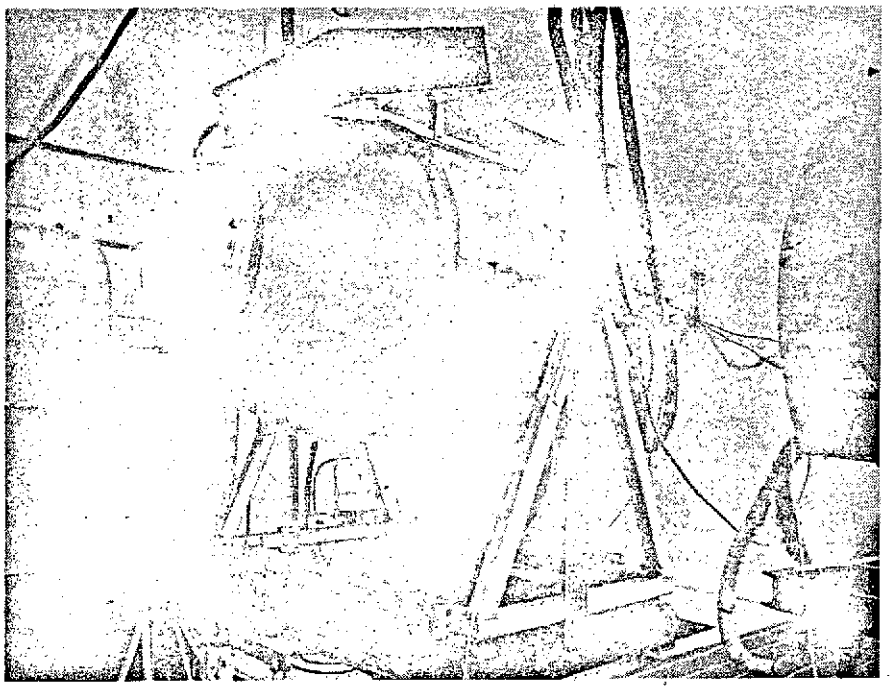

TEST CAVITY IN GIMBALING FIXTURE

**Figure 5-16**

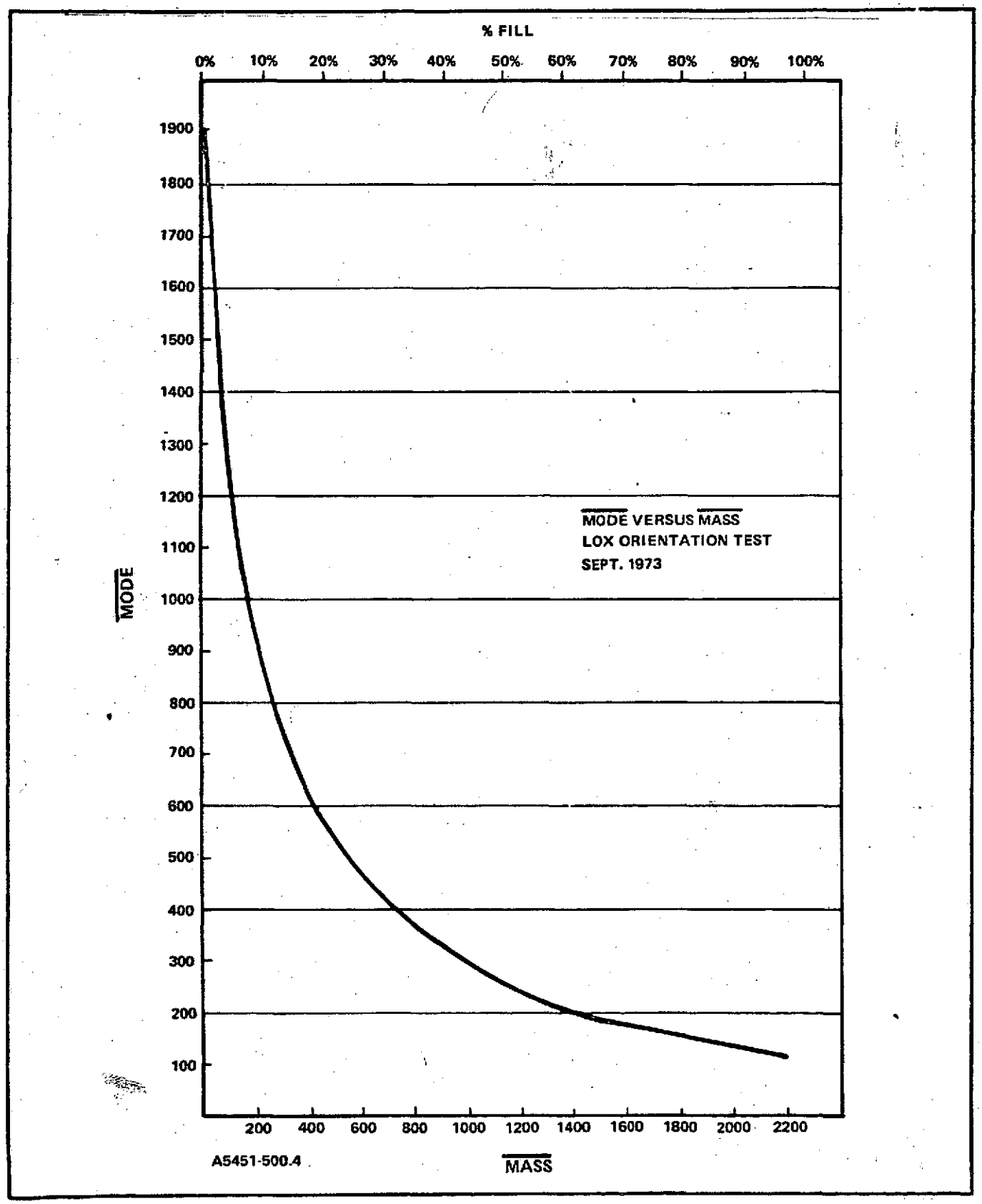
% FILL
0%
10%
20%
30%
40%
50%
60%
70%
80%
90%
100%
1900
1800
1700
1600
1500
1400
1300
1200
1100
1000
900
800
700
600
500
400
300
200
100
MODE
MODE VERSUS MASS
LOX ORIENTATION TEST
SEPT. 1973
200
400
600
800
1000
1200
1400
1600
1800
2000
2200
MASS
A5451-500.4

Figure 5-17

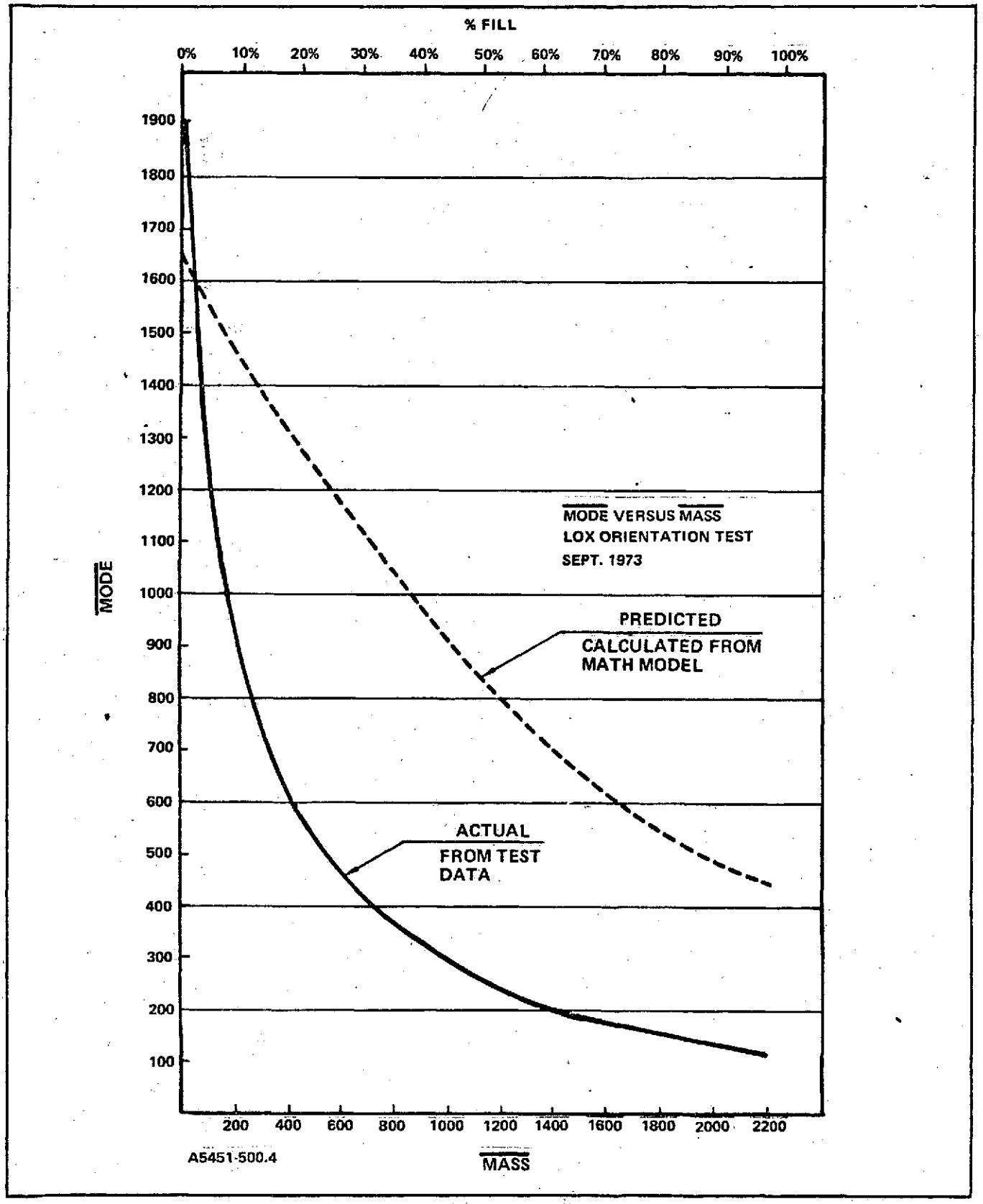
% FILL
0%
10%
20%
30%
40%
50%
60%
70%
80%
90%
100%
1900
1800
1700
1600
1500
1400
1300
1200
1100
1000
900
800
700
600
500
400
300
200
100
MODE
MODE VERSUS MASS
LOX ORIENTATION TEST
SEPT. 1973
PREDICTED
CALCULATED FROM
MATH MODEL
ACTUAL
FROM TEST
DATA
200
400
600
800
1000
1200
1400
1600
1800
2000
2200
MASS
A5451-500.4

Figure 5-18

- Mode count frequency distribution.

Determination of the goodness of fit of the mode count to a normal/uniform distribution was accomplished by applying a $\chi^2$ test and a Kolmogorov-Smirnov Test. The mode distribution was found to be neither uniform nor normal. The distribution approaches an exponential type distribution yet does not quite fit this mode.

A polynominal fit of the LOX loading curve was attempted. In order to make the fit as close as possible (thereby minimizing the residuals) the LOX loading response curve was divided into three polynomial segments. The curves for each segment are of the form

$$Y = \beta_0 + \beta_1 X + \beta_2 X^2 + \beta_3 X^3 + \beta_4 X^4$$

where Y = mass
X = mode count
$\beta_0 \ldots \beta_4$ are the coefficients of the regression polynomial.

Table XIII lists the parameters for the three segments.

TABLE XIII

REGRESSION EQUATIONS FOR LOX DATA

| SEGMENT | MASS RANGE | $\beta_0$ | $\beta_1$ | $\beta_2$ | $\beta_3$ | $\beta_4$ |
|---|---|---|---|---|---|---|
| I | 0 - 655 | 1006.41 | -2.46574 | 0.256244E-02 | -0.125232E-05 | 0.231544E-09 |
| II | 655 - 1306 | 1987.45 | -11.3526 | 0.305777E-01 | -0.305935E-04 | 0.0 |
| III | 1306 - 2182 | 203.240 | 22.7105 | 0.175369 | 0.369973E-03 | 0.0 |

A summary for each polynomial fit is given in Tables XIV, XV and XVI respectively

TABLE XIV

SUMMARY OF POLYNOMIAL FIT - SEGMENT I

| MODES | ACTUAL MASS | CALCULATED MASS | % ERROR |
|---|---|---|---|
| 1904.15 | 0.01 | 0.177 | 13.8 |
| 1198.77 | 107.3046 | 107.4136 | -0.102 |
| 874.029 | 216.448 | 215.508 | 0.436 |
| 696.110 | 324.448 | 327.210 | -0.844 |
| 586.163 | 435.402 | 433.248 | 0.497 |
| 498.018 | 547.840 | 547.050 | 0.145 |
| 430.261 | 655.088 | 656.108 | -0.156 |

Mean Error for estimate of mass = 0.6576
Coefficient of Correlation = 0.999978

TABLE XV

SUMMARY OF POLYNOMIAL FIT - SEGMENT II

| MODES | ACTUAL MASS | CALCULATED MASS | % ERROR |
|---|---|---|---|
| 430.261 | 655.088 | 653.456 | 0.250 |
| 399.355 | 762.002 | 763.816 | -0.237 |
| 358.360 | 871.460 | 876.064 | -0.526 |
| 318.551 | 978.276 | 970.012 | 0.852 |
| 272.220 | 1090.114 | 1091.650 | -0.141 |
| 239.746 | 1197.958 | 1203.364 | -0.449 |
| 217.088 | 1305.440 | 1301.980 | 0.266 |

Mean Error for estimate of mass = 2.25766
Coefficient of correlation = 0.999790

TABLE XVI

SUMMARY OF POLYNOMIAL FIT - SEGMENT III

| MODES | ACTUAL MASS | CALCULATED MASS | % ERROR |
|---|---|---|---|
| 217.088 | 1305.440 | 1307.718 | -0.174 |
| 196.377 | 1416.306 | 1403.930 | 0.881 |
| 178.258 | 1523.750 | 1549.380 | -1.65 |
| 170.137 | 1634.438 | 1625.738 | 0.535 |
| 159.351 | 1737.518 | 1732.236 | 0.305 |
| 147.954 | 1854.898 | 1845.412 | 0.514 |
| 135.165 | 1958.262 | 1965.196 | -0.353 |
| 122.122 | 2067.64 | 2070.20 | -0.119 |
| 100.052 | 2182.46 | 2181.00 | 0.067 |

Mean Error for estimate of mass = 4.66960
Coefficient of correlation = 0.999256

The polynomial equations for the loading curve are used as basis for the calculation of mass error. The percent mass error of the system can be arrived at for this dynamic testing by using the standard deviation of the mode count as a measure of the spread of the mode count. This gives a $\pm 1\sigma$ mode count (a high-low mode count about the mean mode count) that can be used with the nonlinear regression equations to calculate the mass error.

The percent mass error of the system is calculated as

$$\% \text{ error} = \frac{\text{Actual Mass} - \text{Calculated Mass}}{\text{Full Tank Mass}} \times 100\%$$

A mass error summary table of percent fill versus error is shown in Table XVII and a plot of the $\pm 1\sigma$ error is shown in Figure 5-19.

The distribution of the mode count was not normal so that extension to a $\pm 3\sigma$ error cannot be readily made. A typical mode count frequency distribution is shown in Figure 5-20.

The frequency distribution of the mass error is shown in Figure 5-21 with its corresponding cumulative error distribution shown in Figure 5-22. Some remarks that can be made about the LOX mass error data are:

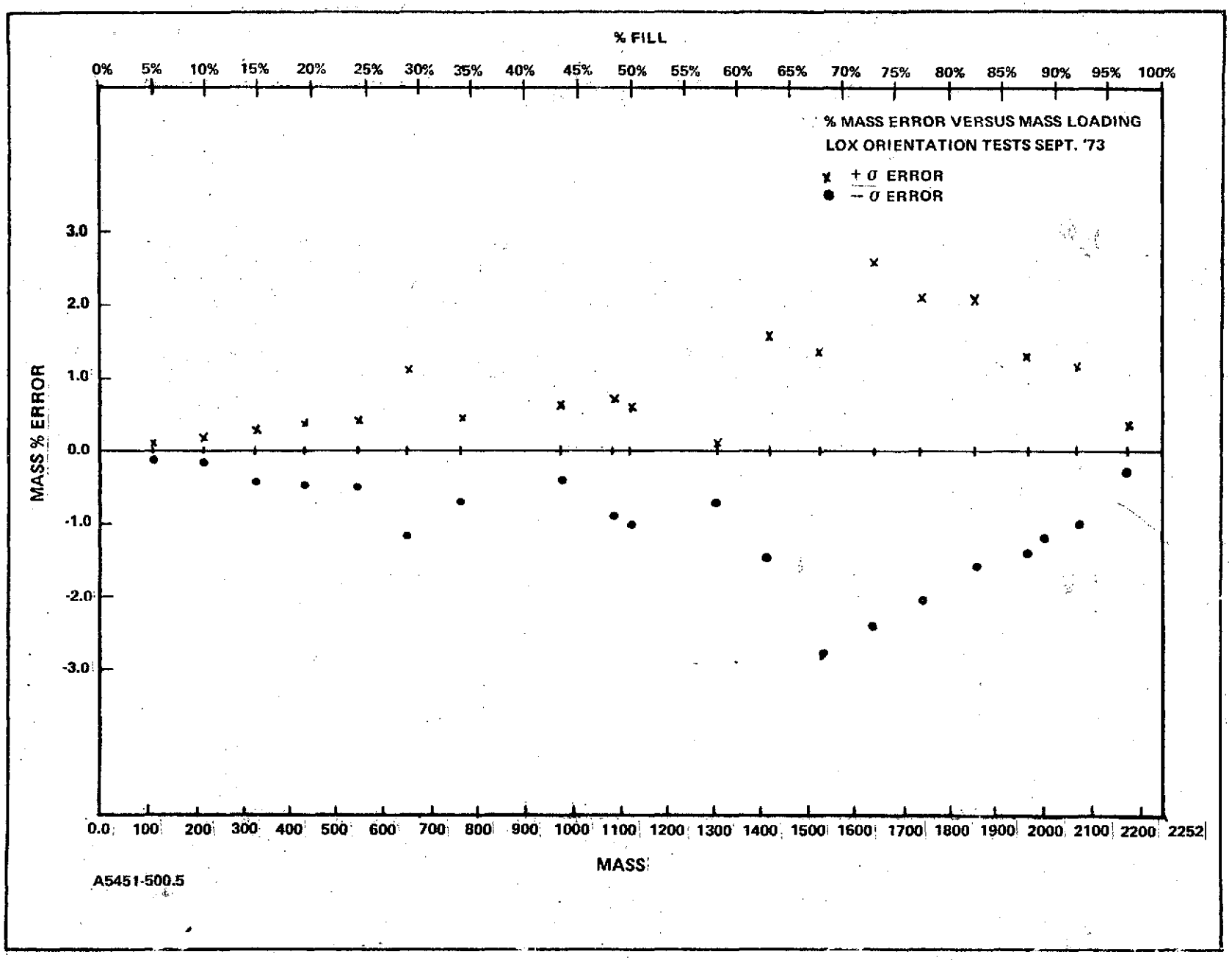
% FILL
0% 5% 10% 15% 20% 25% 30% 35% 40% 45% 50% 55% 60% 65% 70% 75% 80% 85% 90% 95% 100%
% MASS ERROR VERSUS MASS LOADING
LOX ORIENTATION TESTS SEPT. '73
+σ ERROR
-σ ERROR
MASS % ERROR
3.0
2.0
1.0
0.0
-1.0
-2.0
-3.0
0.0 100 200 300 400 500 600 700 800 900 1000 1100 1200 1300 1400 1500 1600 1700 1800 1900 2000 2100 2200 2252
MASS
A5451-500.5

Figure 5-19

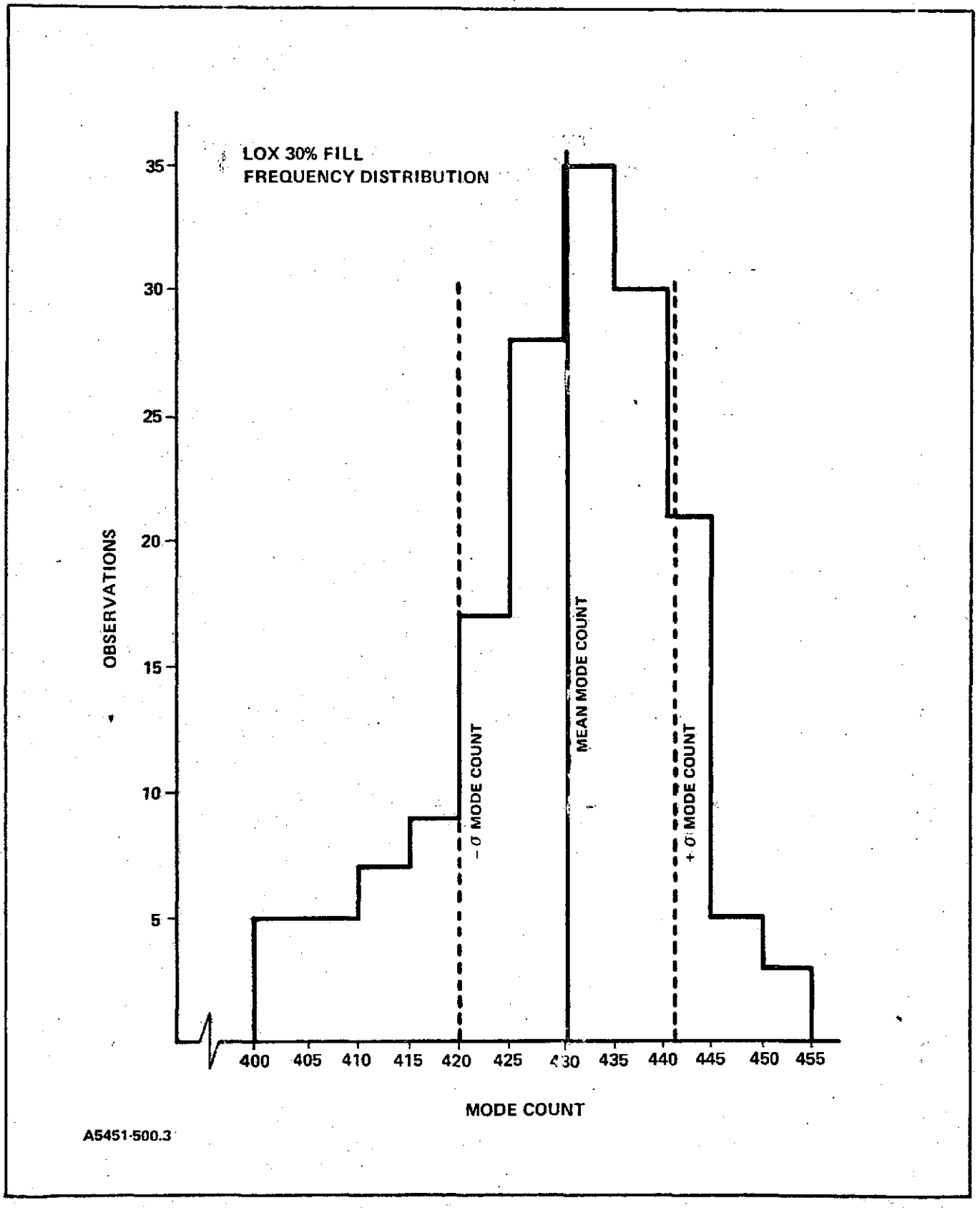
LOX 30% FILL
FREQUENCY DISTRIBUTION
OBSERVATIONS
35
30
25
20
15
10
5
400
405
410
415
420
425
430
435
440
445
450
455
MODE COUNT
– σ MODE COUNT
MEAN MODE COUNT
+ σ MODE COUNT
A5451-500.3

Figure 5-20

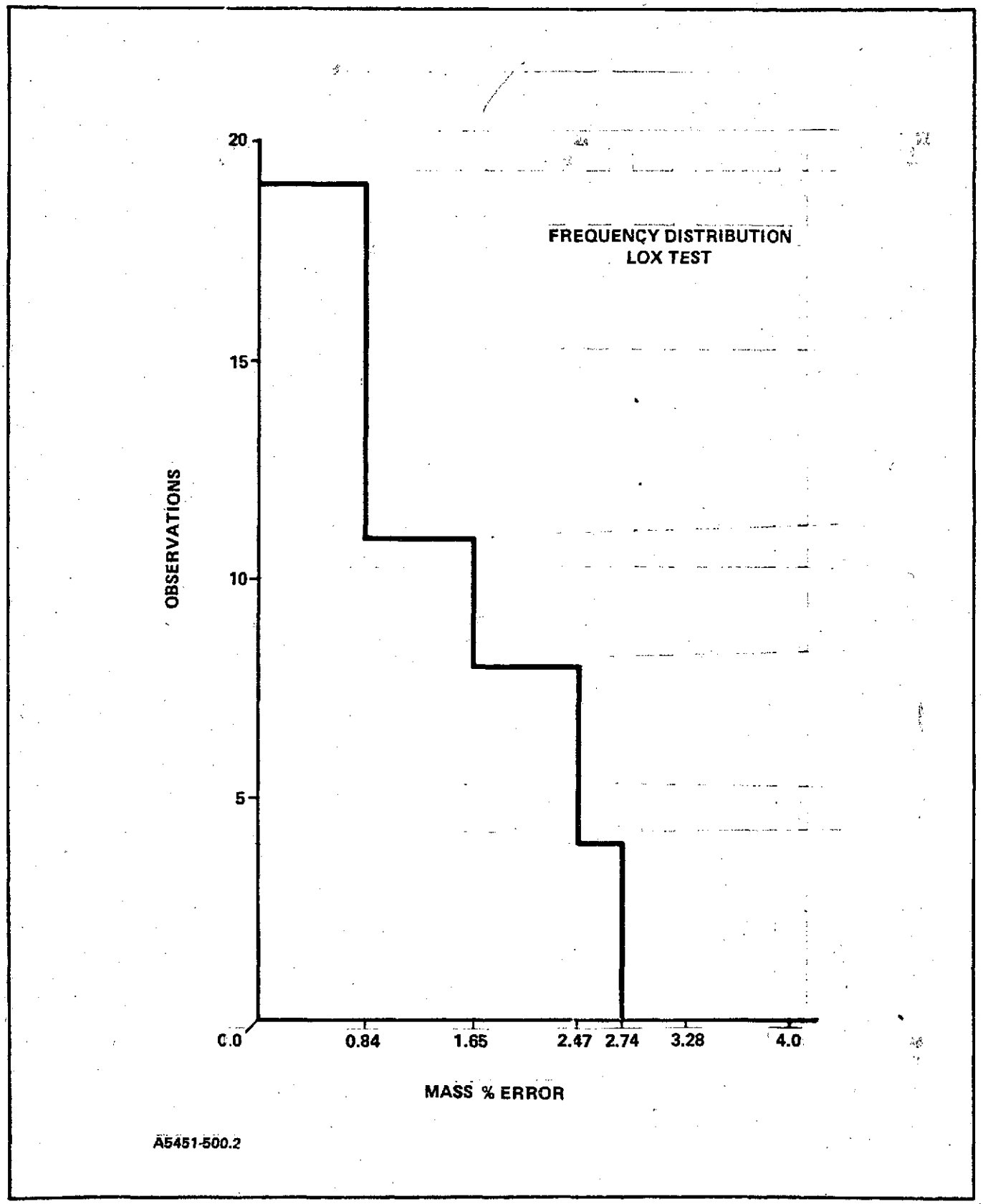
FREQUENCY DISTRIBUTION
LOX TEST
OBSERVATIONS
20
15
10
5
0.0
0.84
1.65
2.47
2.74
3.28
4.0
MASS % ERROR
A5451-500.2

Figure 5-21

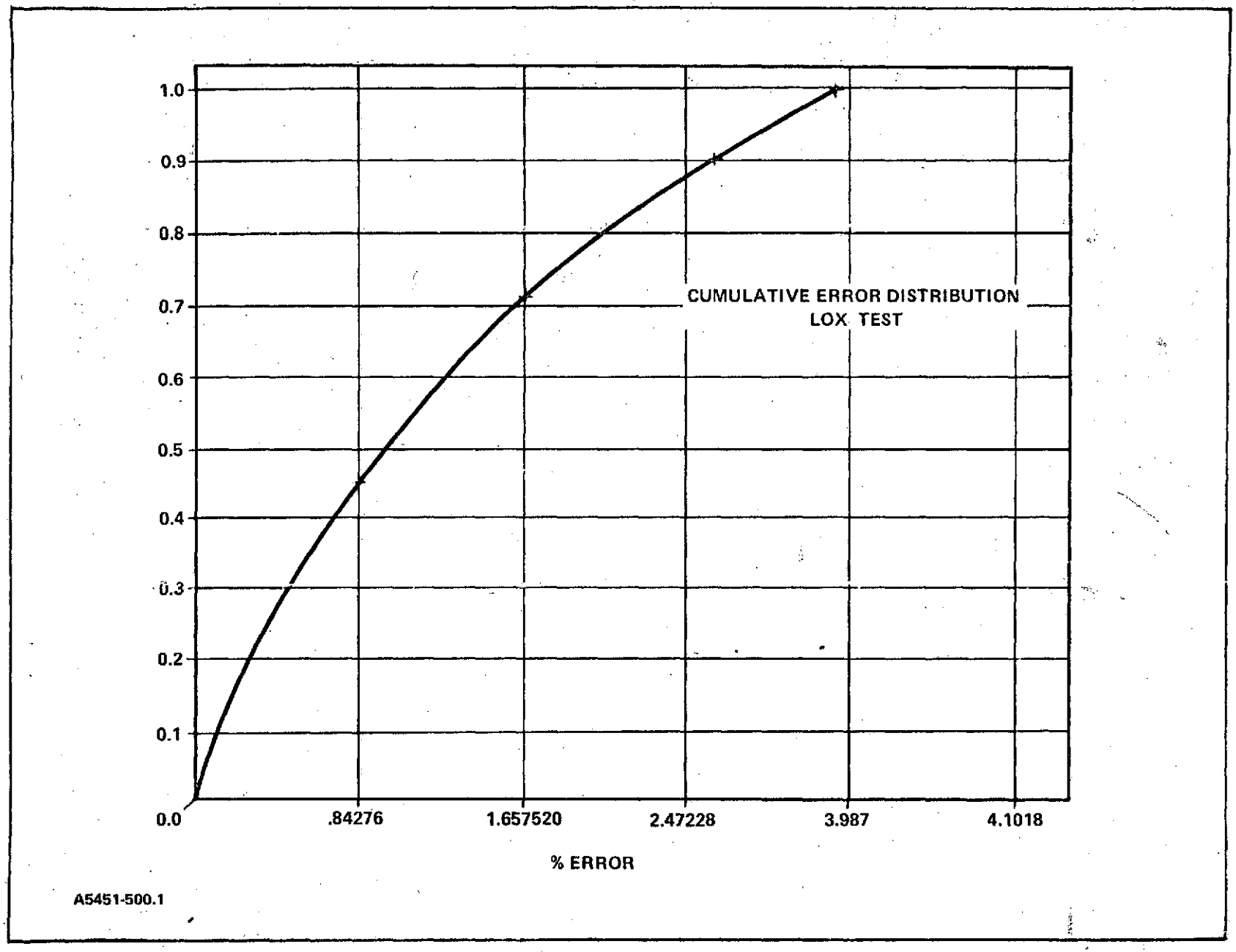
CUMULATIVE ERROR DISTRIBUTION
LOX TEST
1.0
0.9
0.8
0.7
0.6
0.5
0.4
0.3
0.2
0.1
0.0
.84276
1.657520
2.47228
3.987
4.1018
% ERROR
A5451-500.1

Figure 5-22

## TABLE XVII

## LOX MASS ERROR SUMMARY

| % FILL | MEAN MODE COUNT | STANDARD DEVIATION | MODE COUNT ±σ | ACTUAL MASS (LBS) | CALCULATED MASS | MASS % ERROR |
|---|---|---|---|---|---|---|
| 97 | 100.052 | 5.0755 | 105.1275<br>94.9765 | 2182.469 | 2164.896<br>2190.502 | 0.390<br>-0.178 |
| 95 | 122.122 | 7.2697 | 129.3921<br>114.8527 | 2067.746 | 2014.394<br>2117.614 | 1.184<br>-1.107 |
| 90 | 135.165 | 7.2250 | 142.39<br>127.94 | 1958.263 | 1898.976<br>2026.134 | 1.316<br>-1.507 |
| 85 | 147.954 | 8.5200 | 156.474<br>139.434 | 1854.098 | 1761.002<br>1926.604 | 2.084<br>-1,592 |
| 80 | 159.351 | 9.1571 | 168.5081<br>150,1939 | 1737.518 | 1641.568<br>1823.43 | 2.130<br>-1.907 |
| 75 | 170.137 | 11.6931 | 181.8301<br>158.44 | 1634.439 | 1517.552<br>1741.312 | 2.595<br>-2.373 |
| 70 | 178.258 | 10.3558 | 188.6138<br>167.9022 | 1523.752 | 1460.956<br>1647.484 | 1.394<br>-2.747 |
| 65 | 196.377 | 10.2173 | 206.5943<br>186.1597 | 1416.306 | 1344.892<br>1460.782 | 1.585<br>-1.431 |
| 60 | 217.088 | 8.8217 | 225.9097<br>208.2663 | 1305.438 | 1298.632<br>1337.248 | 0.151<br>-0.706 |
| 55 | 239.746 | 9.4356 | 249.1816<br>230.3104 | 1197.958 | 1167.72<br>1242.034 | 0.671<br>-0.978 |
| 50 | 272.220 | 12.2240 | 284.444<br>259.996 | 1090.116 | 1056.374<br>1130.242 | 0.749<br>-0.891 |
| 45 | 318.551 | 10.6566 | 329.2076<br>307.8944 | 978.278 | 944.978<br>995.634 | 0.739<br>-0.385 |
| 40 | 358.360 | 10.3698 | 368.7298<br>437.9902 | 871.46 | 850.110<br>901.000 | 0.474<br>-0.656 |
| 35 | 401.762 | 13.29 | 415.052<br>382.572 | 762.003 | 711.304<br>813.222 | 1.125<br>-1.137 |
| 30 | 430.261 | 11.3556 | 441.6166<br>418.9054 | 655.088 | 636.374<br>676.462 | 0.415<br>-0.474 |

TABLE XVII - (continued)

| %FILL | MEAN MODE COUNT | STANDARD DEVIATION | MODE COUNT ±σ | ACTUAL MASS (LBS) | CALCULATED MASS | MASS & ERROR |
|---|---|---|---|---|---|---|
| 25 | 498.108 | 12.6508 | 510.6688<br>485.3672 | 547.842 | 528.888<br>565.878 | 0.421<br>-0.400 |
| 20 | 586.163 | 13.8119 | 599.9749<br>572.3511 | 435.402 | 417.93<br>449.21 | 0.388<br>-0.307 |
| 15 | 698.255 | 16.4196 | 714.6750<br>681.8350 | 324.447 | 312.544<br>339.070 | 0.264<br>-0.325 |
| 10 | 874.029 | 13.5003 | 887.5293<br>860.5287 | 216.449 | 209.206<br>222.068 | 0.161<br>-0.125 |
| 5 | 1198.77 | 19.0021 | 1217.7721<br>1179.7679 | 107.305 | 102.682<br>112.234 | 0.103<br>-0.109 |
| 0 | 1904.15 | 10.5612 | 1914.7112<br>1893.5888 | 0.0 | 1.508<br>-1.25 | -0.033<br>0.028 |

- The mean of the error data is 0.898%
- 90% of the data exhibits a mass error of less than 2%
- $\pm 1\sigma$ mode count excursions are good indications of what the probable mass error will be.

## 5.8 $LH_2$ ORIENTATION TEST

During $LH_2$ testing, the RF frequency was swept from 1 - 2 GHz at a rate of 300 milliseconds, sequencing each of the four antenna elements for 300 milliseconds. After dumping the $LN_2$ and vacuum purging the pressure vessel and lines with helium, $LH_2$ loading tests were performed. After the tank was topped off and full, orientation tests began at each 10% fill level plus 95% and 5%. These tests were performed by starting with the tank at 95% full and rotating the tank in 15° increments and recording the gauging system output at each angle. This required taking data at 25 angular positions at each of the twelve fill levels. At each position the automatic data acquisition system was allowed to punch 20 IBM cards recording the following:

- Time
- Mass From Load Cell
- Fluid Temperature
- Tank Angular Position
- Tank Pressure
- RF Mode Count

The two types of orientation tests were performed:

A. Static Orientation Tests

- Tank positioned and fluid allowed to come to rest at each position prior to taking data
- Mass held constant
- Data recorded at each 15° increment of orientation

B. Dynamic Orientation Tests

- Continuous orientation of test tank
- Rate of rotation of tank approximately 6° per second
- Mass held constant
- Data recorded continuously

The data obtained from the mode count and mass of $LH_2$ gives a linear regression curve as shown in Figure 5-23. Figure 5-24 shows this data superimposed over a plot of the predicted loading response.

### 5.8.1 $LH_2$ DATA ANALYSIS

The first step in analyzing the data was to calculate the average mode count for all orientations and the average mass indicated for each incremental loading according to the below equations:

$$\overline{Mode} = \frac{1}{N} \sum_{i=1}^{N} Mode(i) \quad (1)$$

$$\overline{Mass} = \frac{1}{N} \sum_{i=1}^{N} Mass(i) \quad (2)$$

The average mode count and average mass for all orientations are then used in the equations shown below to calculate the variance in the data.

$$\sigma^2 (Mode) = \frac{1}{N-1} \sum_{i=1}^{N} Mode(i)^2 - \overline{Mode}^2 \quad (3)$$

$$\sigma^2 (Mass) = \frac{1}{N-1} \sum_{i=1}^{N} Mass(i)^2 - \overline{Mass}^2 \quad (4)$$

Determination of the goodness of fit to the normal/uniform distribution of mode count was accomplished by applying the $\chi^2$ test or the Kolmogorov-Smirnov Test. Again the mode count data did not exhibit either a normal or uniform distribution.

In addition, the data was utilized to establish a series of computer generated plots listed below:

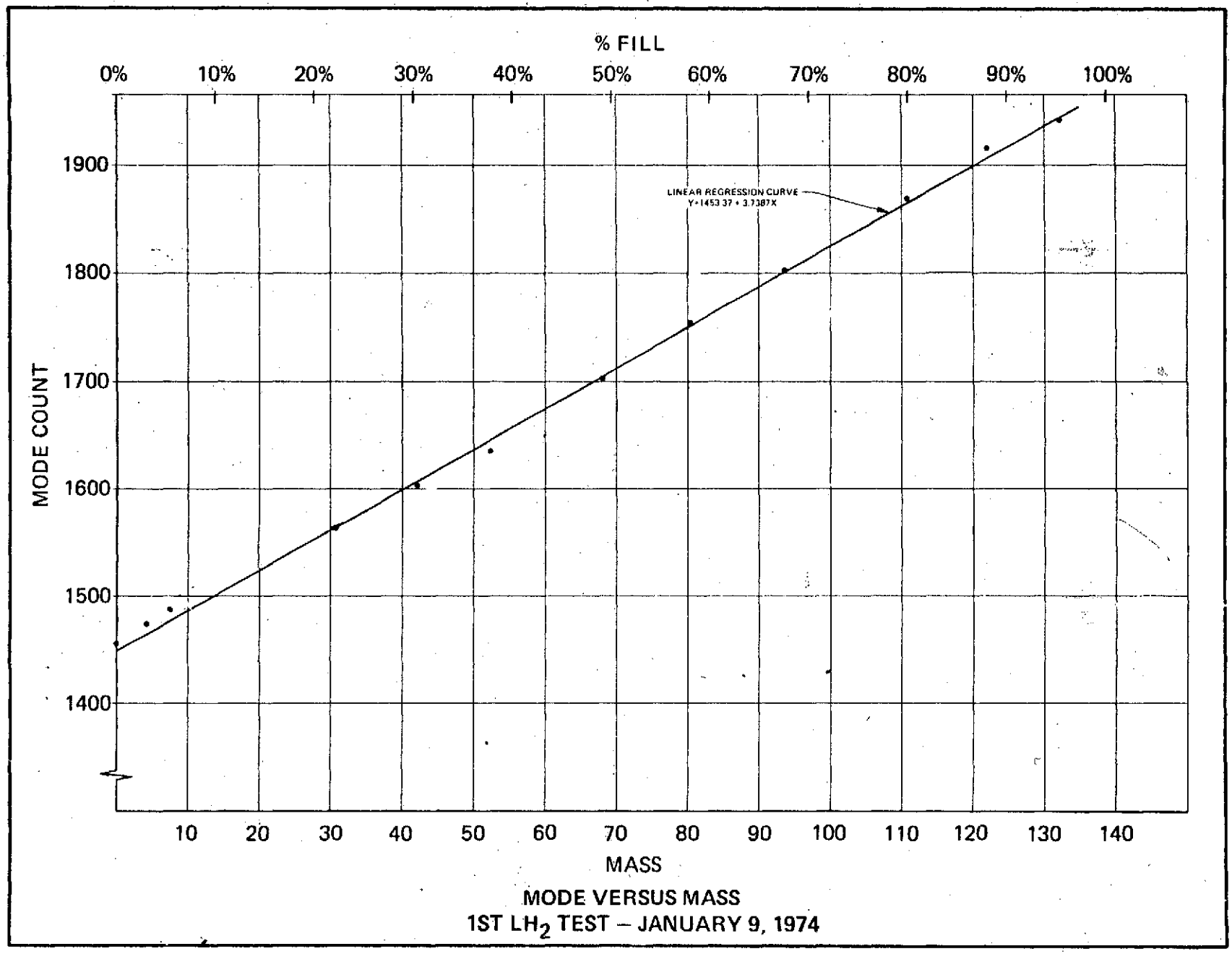


MODE VERSUS MASS
1ST $LH_2$ TEST – JANUARY 9, 1974

Figure 5-23

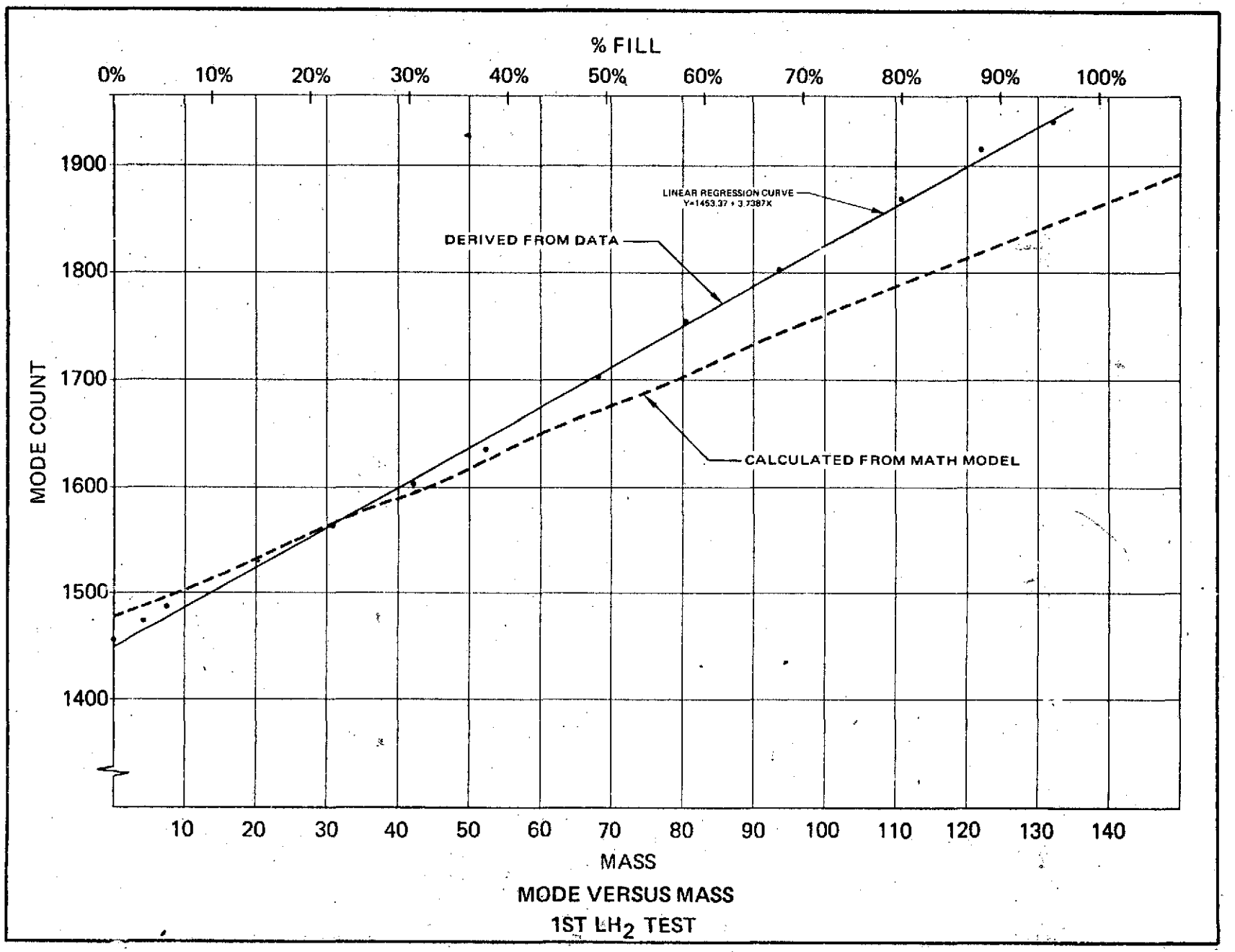
% FILL
0%
10%
20%
30%
40%
50%
60%
70%
80%
90%
100%
1900
1800
1700
1600
1500
1400
MODE COUNT
LINEAR REGRESSION CURVE
Y=1453.37 + 3.7387X
DERIVED FROM DATA
CALCULATED FROM MATH MODEL
10
20
30
40
50
60
70
80
90
100
110
120
130
140
MASS
MODE VERSUS MASS
1ST LH2 TEST

Figure 5-24

- Mode count versus static orientation angle
- Mass versus orientation angle
- Mode count versus mass
- Mode count versus dynamic orientation angle
- Mode count versus mass under dynamic orientation
- Mass versus orientation angle under dynamic orientation
- Mode count frequency distribution

Using the mean mass and the average mode count for all orientations for each respective mass loading, a linear regression curve of the form

$$Y = \beta_0 + \beta_1 X \tag{5}$$

was generated, where

$Y$ = Mode count
$X$ = Mass
$\beta_0$ = the Y intercept
$\beta_1$ = the slope of the line

The coefficients $\beta_0$ and $\beta_1$ can be determined from the simultaneous solution of the following equations:

$$\beta_0 = \frac{1}{N} \sum_{i=1}^{N} Y_i - \beta_1 \sum_{i=1}^{N} X_i \tag{6}$$

$$\beta_1 = \frac{\sum^{N} X \sum^{N} Y - N \sum^{N} XY}{(\sum^{N} X)^2 - N \sum^{N} X^2} \tag{7}$$

The regression curve is used as the basis for all error calculations.

Solutions of equations 6 and 7 using the data from the $LH_2$ tests provide the values for $\beta_0$ and $\beta_1$ of the linear regression curve. They are:

$\beta_0$ = 1453.37 (Empty tank mode count)

$\beta_1$ = 3.7487 (Sensitivity modes/lbs)

The regression curve then becomes

$$Y = 1453.37 + 3.7487\ X \qquad (8)$$

This curve is shown in Figure 5-23 along with the mean mode count for all orientations for each mass loading. The residuals of the measured mean mode count relative to the mode count calculated from the least squares regression curve are shown in Table XVIII. These residuals are calculated from:

% mode count error =

$$\frac{(\text{mean mode count})_{\text{actual}} - (\text{mode count})_{\text{calculated}}}{(\text{mode count})\ \text{calculated}} \times 100\% \qquad (9)$$

TABLE XVIII

RESIDUAL ERRORS

| % FILL | MASS LBS | THEORETICAL MODE COUNT | ACTUAL MODE COUNT | % ERROR MODE COUNT (POINT) |
|---|---|---|---|---|
| 0% | 0.0 | 1453.37 | 1456.10 | 0.188% |
| 2.5% | 3.72 | 1467.29 | 1473.7 | 0.437% |
| 5.0% | 7.19 | 1480.25 | 1487.2 | 0.469% |
| 20% | 30.41 | 1567.07 | 1564.4 | 0.170% |
| 30% | 42.09 | 1610.75 | 1603.5 | 0.450% |
| 40% | 52.21 | 1648.58 | 1637.0 | 0.702% |
| 50% | 68.17 | 1708.25 | 1703.6 | 0.272% |
| 60% | 80.68 | 1755.02 | 1756.4 | 0.078% |
| 70% | 93.77 | 1803.93 | 1801.5 | 0.135% |
| 80% | 110.94 | 1868.14 | 1869.0 | 0.046% |
| 90% | 122.19 | 1910.20 | 1920.1 | 0.518% |
| 95% | 132.07 | 1947.16 | 1947.5 | 0.018% |

It is noted that the residuals are very small.

### 5.8.1.1 $LH_2$ STATIC ORIENTATION CALCULATIONS

For each fill level and static orientation point the mean mass was calculated using the mean mode count for the orientation. The calculated mass for each orientation is arrived at by means of the equation

$$X = \frac{Y-1453.37}{3.7387}$$

The % mass error of the system is then calculated as

$$\text{Percent Error} = \frac{\text{actual mass - calculated mass}}{\text{full tank mass}} \times 100\%$$

A mass error matrix of percent fill and orientation angle can be constructed so as to present a summary of all system errors. This matrix is shown in Figure 5-25.

The error matrix can be analyzed to yield further insight into the behavior of the RF Gauging. One type of analysis available is to group the data so that its frequency distribution is apparent and the cumulative error distribution is calculated. Having the cumulative distribution, the probability function for the data can be arrived at by simply differentiating the cumulative distribution function.

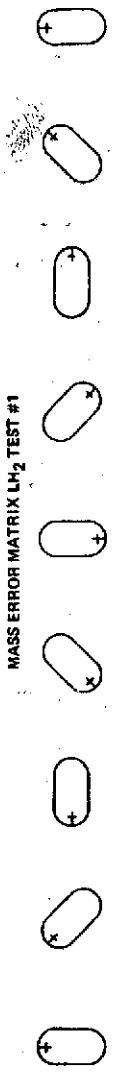


| % / DEGREE | 0 | 2.5 | 5.2 | 20 | 30 | 40 | 50 | 60 | 70 | 80 | 90 | 100 |
|---|---|---|---|---|---|---|---|---|---|---|---|---|
| 180 | -1.091 | 3.41 | -0.514 | -6.814 | -2.98 | -0.385 | -4.53 | -2.10 | -2.64 | 1.15 | -4.97 | 2.204 |
| 165 | -0.7878 | 2.46 | 2.69 | 2.10 | -1.70 | -1.844 | -1.22 | -0.43 | -2.1 | -4.41 | -0.90 | -0.857 |
| 150 | -0.2521 | 4.45 | -0.1973 | 0.951 | -0.163 | 0.980 | 0.66 | 1.20 | -0.66 | 2.66 | -2.73 | -1.059 |
| 135 | 0.99 | 6.47 | 1.01 | 1.76 | 2.59 | 4.40 | 2.35 | 4.20 | -1.33 | 2.53 | -2.20 | 1.58 |
| 120 | 2.10 | 3.52 | 0.74 | 0.76 | -2.56 | 5.04 | -0.12 | 2.20 | -2.6 | 1.22 | -1.988 | 4.796 |
| 105 | 1.524 | 1.93 | -0.896 | 3.83 | 1.74 | 5.27 | 5.69 | -0.065 | 1.77 | 5.11 | -2.01 | -1.145 |
| 90 | -2.67 | -6.90 | 1.315 | 2.41 | 3.025 | 6.20 | -0.713 | 0.81 | 1.82 | 4.23 | -1.99 | -4.82 |
| 75 | -1.968 | -3.85 | -2.61 | 3.10 | 1.12 | 3.67 | -2.72 | 3.23 | 1.015 | -1.17 | 0.461 | 1.569 |
| 60 | -2.52 | 1.33 | -2.83 | 3.334 | 4.03 | 0.480 | -4.20 | -0.698 | -0.684 | -0.81 | 1.39 | 1.764 |
| 45 | -2.47 | 1.65 | -0.370 | -1.65 | 2.85 | 0.580 | 2.54 | 0.420 | -0.072 | -0.37 | -3.514 | -3.02 |
| 30 | -2.37 | -2.48 | -3.33 | -3.601 | -0.31 | 0.058 | 0.69 | -1.24 | 0.31 | -0.41 | -3.565 | 1.714 |
| 15 | -1.88 | -6.12 | -1.46 | 0.0072 | -2.20 | -0.38 | -5.01 | -3.47 | 1.45 | -2.60 | -0.202 | -3.205 |
| 0 | -0.826 | -0.37 | 4.10 | -0.99 | 2.83 | 1.001 | 2.91 | 3.97 | -0.05 | -7.10 | -1.68 | -5.75 |
| -15 | -0.056 | -1.48 | 1.10 | -0.99 | 3.97 | 1.73 | -1.497 | -0.698 | -3.11 | -3.50 | -7.83 | -1.05 |
| -30 | 0.125 | 1.89 | 0.05 | -1.63 | -0.533 | 2.24 | 0.12 | -3.010 | -3.36 | -3.54 | 1.53 | -5.36 |
| -45 | -0.892 | -2.80 | 7.40 | -0.99 | -.350 | 0.72 | -2.10 | -5.10 | 0.202 | 2.43 | 3.92 | -1.00 |
| -60 | -3.10 | -1.23 | -0.660 | 1.17 | -3.414 | 2.21 | 0.38 | -0.680 | 1.76 | 5.47 | 3.493 | 1.823 |
| -75 | 1.23 | -2.54 | -1.299 | 0.15 | 1.79 | 2.96 | 2.002 | -0.281 | 3.10 | 3.74 | 4.26 | 1.512 |
| -90 | 3.496 | -1.68 | 2.36 | 0.519 | -1.62 | -5.45 | 1.77 | 2.35 | 2.97 | 0.63 | 4.10 | 3.64 |
| -105 | 3.38 | -0.85 | -0.565 | 2.10 | 0.39 | -3.40 | 4.41 | 0.425 | 2.55 | 2.93 | 1.66 | 6.172 |
| -120 | 3.38 | 2.15 | 4.56 | -0.25 | 1.94 | -1.93 | 1.44 | 4.73 | 3.66 | 3.00 | 4.27 | 4.96 |
| -135 | 2.259 | 0.58 | 0.588 | 0.245 | -2.91 | -3.39 | 1.88 | 1.51 | -0.598 | 3.23 | 2.79 | 3.73 |
| -150 | 0.912 | -3.24 | -0.610 | 0.1152 | -1.47 | -0.53 | 1.17 | -2.35 | 0.0072 | -2.10 | 1.84 | -1.26 |
| -165 | 1.22 | 0.756 | 1.373 | -3.95 | 2.40 | -3.82 | -0.81 | -1.20 | 0.72 | -7.3 | 0.75 | 1.015 |
| -180 | 2.129 | 0.23 | -0.51 | -3.62 | -2.66 | -0.78 | -2.12 | -1.61 | -2.44 | -2.7 | 2.92 | -5.48 |

**MASS ERROR MATRIX**

Figure 5-25

Figure 5-26 and Figure 5-27 are the plots of frequency distribution and cumulative distribution respectively.

From this breakdown it is seen that

- Mean of error data is 2.18%
- 75% of the data exhibits an error of less than 3%.

### 5.8.1.2 $LH_2$ DYNAMIC TEST DATA

In the case of the dynamic test, the tank is continuously rotated from -180° to +180° with one revolution per sixty seconds transit rate. The plane of the fluid is slowly perturbed throughout the test period.

Table XIX displays some interesting results obtained when the average mode count is obtained from the dynamic test data.

TABLE XIX

DYNAMIC ROTATION MASS ERROR

| % FILL | NO. OBSERVATIONS | MODES | THEORETICAL MODES | % MASS ERROR |
|---|---|---|---|---|
| 0% | 81 | 1453.5 | 1453.7 | 0% |
| 2.5% | 64 | 1472.8 | 1468.1 | 0.898% |
| 5% | 41 | 1482.9 | 1480.3 | 0.510% |
| 20% | 54 | 1568.6 | 1567.1 | 0.295% |
| 30% | 57 | 1605.2 | 1610.8 | 1.07% |
| 40% | 58 | 1641.6 | 1648.6 | 1.44% |

From Table XIX it is noted that:

- A small number of observations is sufficient enough to obtain a good mode count average.
- From the test we observe that a slight perturbation in the liquid interface will greatly improve the mass accuracy of the gauge.
- The random motion of the fluid under Zero g conditions should result in good averages of the mean mode count, consequently low mass gauging error.

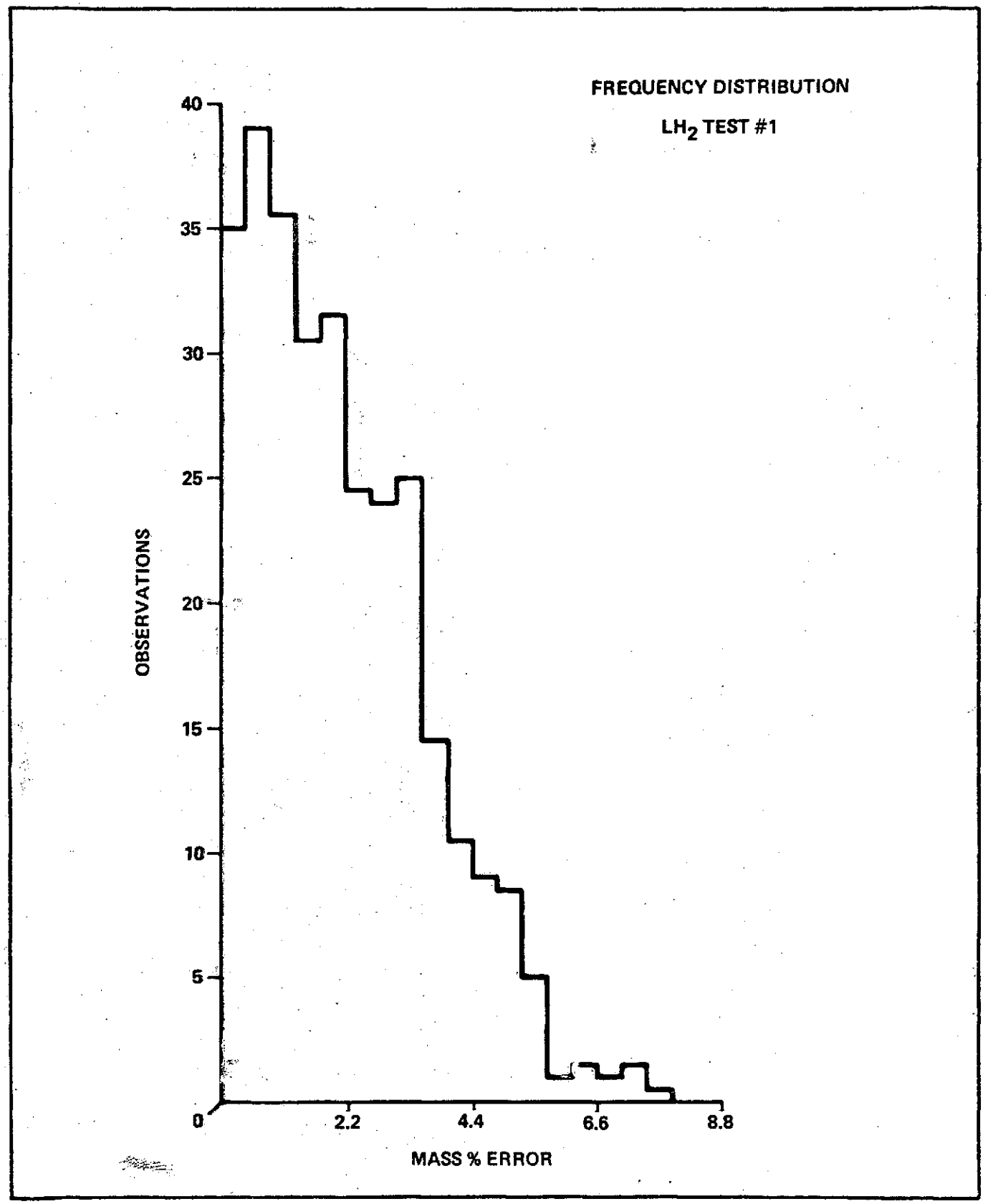
FREQUENCY DISTRIBUTION
$LH_2$ TEST #1
OBSERVATIONS
40
35
30
25
20
15
10
5
0
2.2
4.4
6.6
8.8
MASS % ERROR

Figure 5-26

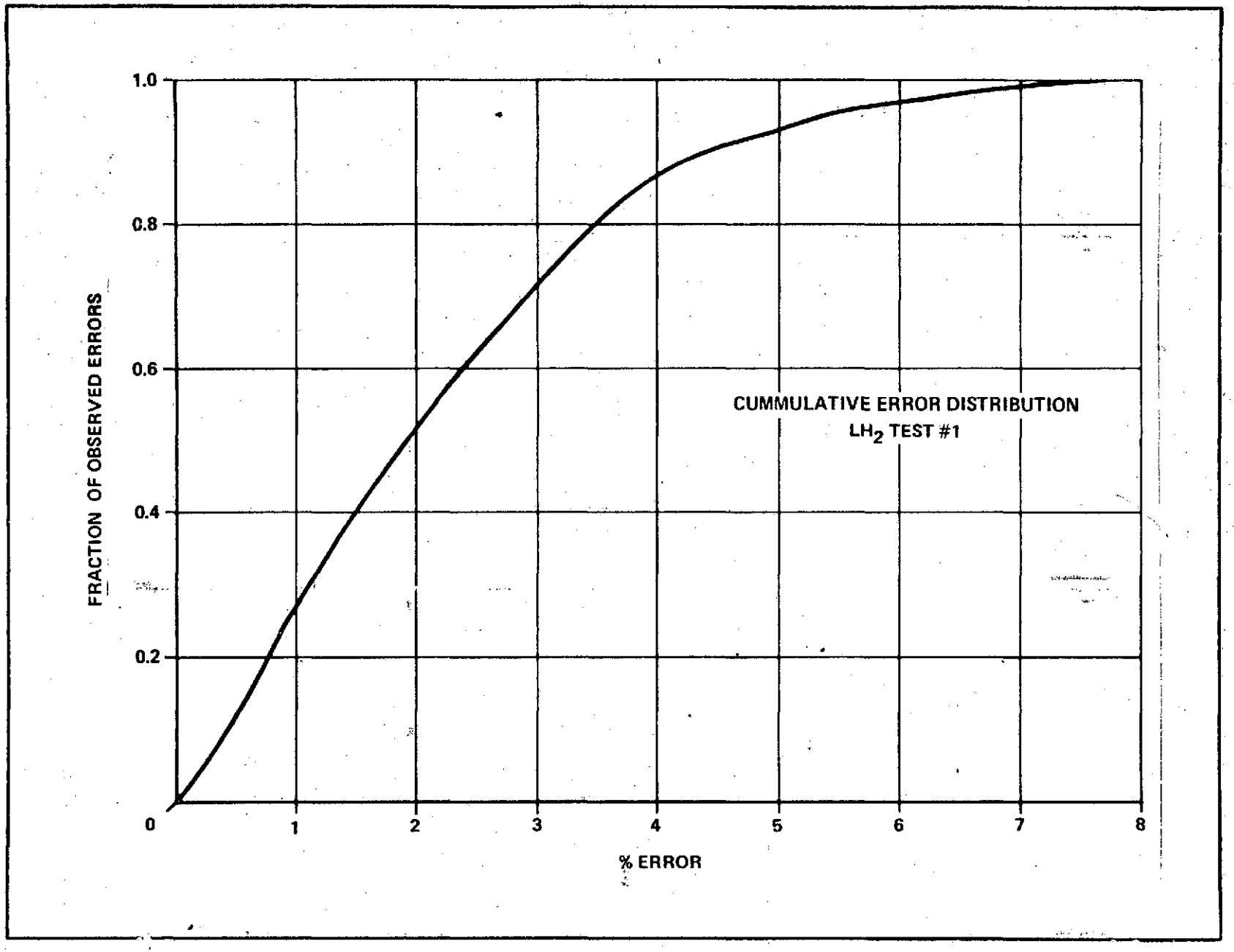
1.0
0.8
0.6
0.4
0.2
0
FRACTION OF OBSERVED ERRORS
CUMMULATIVE ERROR DISTRIBUTION
$LH_2$ TEST #1
1
2
3
4
5
6
7
8
% ERROR

Figure 5-27

## 6.0 CONCLUSIONS

From the experimental results of the tests conducted during Phase B the following conclusions may be made.

- The RF Gauging mode counting technique has demonstrated conclusively its feasibility for gauging liquid hydrogen and liquid oxygen under all attitude conditions.

- The RF Gauging mode counting technique has demonstrated conclusively its feasibility for gauging fluids in reduced and zero gravity environments.

- The RF Gauging mode counting technique has demonstrated accuracies which are rapidly approaching the test instrumentation accuracies. The liquid hydrogen orientation testing demonstrated a mean error of 2.18% with 75% of the data exhibiting an error of less than 3%. The liquid oxygen orientation testing demonstrated a mean error of 0.898% with 90% of the data exhibiting a mass error of less than 2%.

- The orientation tests have demonstrated that a small number of data observations is sufficient enough to obtain a good mode count average and subsequent indication of mass. It is also clear that the random motion of the test fluid under Zero "G" conditions should result in good averages of the mean mode count, consequently low mass gauging error.

- The use of capillary liquid retention screens in tanks utilizing an RF mass gauging system will not be detrimental to the gauging system performance provided the screen mesh is tightly woven, the area of screening within the tank is not a major portion of the total inner surface area, and that material from which the screens are made is either a good electrical conductor or a low loss material.

## APPENDIX A

The RF antenna used in this application is basically a transformer whose function is to couple energy between the external RF energy source and the interior of the tank. Its coupling to the electromagnetic fields established within the tank in part determines the characteristic system Q, and consequently contributes to the number of modes that are detected. When the dielectric assumes an arbitrary second fixed position by orientation of the test tank, the spacial positioning of the electromagnetic fields within the tank is apparently perturbed slightly. As a result, the antenna coupling factors associated with the resonant modes must be similarly altered by some small amount. These changes in coupling factors appear to modify the overall system Q, and therefore change the detected resonant mode count. This phenomena appears to account for at least part of the variation in mode count that is seen for various tank orientations with a typical given mass of dielectric, and hence contributes to the overall performance of the gauging system in terms of mass error. Figure A-1 shows the loading response obtained with benzene in the 1/10 scale SIVB tank for three angular positions of the tank. The process of emptying the tank was done slowly and in such a manner as to induce little or no sloshing of the benzene in the test tank. Figure A-2 shows the loading response obtained for the same liquid and two angular positions of the tank; however, in this case the RF electromagnetic fields within the tank were forced to fluctuate in such a manner as to permit a more optimum overall coupling to the resonant mode solutions. This was done by gently sloshing the benzene within the tank. Figure A-3 shows the loading response for the same liquid and several angular positions of the tank where the RF electromagnetic fields within the tank were forced to fluctuate by recycling a small quantity of benzene with an air driven pump. This pump removed benzene from one location in the tank and forced it back in the form of a pulsating spray. In each of the above cases where gauging error was reduced significantly, the electromagnetic fields within the tank were forced to fluctuate in some prescribed manner.

It soon becomes apparent that it would be most desirable to find an electronic means by which to accomplish the spacial movements in these electromagnetic fields. This effect could be achieved by the use of an RF probe assembly containing two or more fixed antenna elements displaced physically from one another by dimensionally less than one-quarter wavelength of the average of middle frequency of the operating frequency band. By the use of a solid-state pin diode type single-pole multi-throw switch the RF energy source would be programmed to sweep $f_1$ to $f_2$ sequentially through each antenna

element. From this the mode counts detected for each of the three respective sweeps could easily be summed and averaged electronically.

A secondary, and closely related advantage of this multi-element concept is that the physical presence of two or more antenna elements clustered at various angles on the RF probe assembly would assure that the polarization of each antenna element would in effect permit a more distributed coupling to the established electromagnetic fields, and at the same time enhance a more uniform RF illumination of the tank than can now be achieved with a single antenna element.

A cursory evaluation of a multi-antenna/pin diode switching arrangement was made using a cylindrical tank with protruding hemispherical ends. Four spiral antennas were positioned in the test tanks, and tests performed with RP-1 using first one of the antenna elements, and secondly all four antenna elements. Figure A-4 shows the RF analog output vs. test fluid mass using only one of the RF antenna elements where the test tank was positioned at three different angles. (A loading response curve acquired for each respective angle). Figure A-5 shows the loading response obtained for each of the same three tank positions where all test conditions were the same except that the four antenna elements were used.

The results definitely indicate that exploitation of a multi-element RF probe assembly would enhance potential system accuracy.

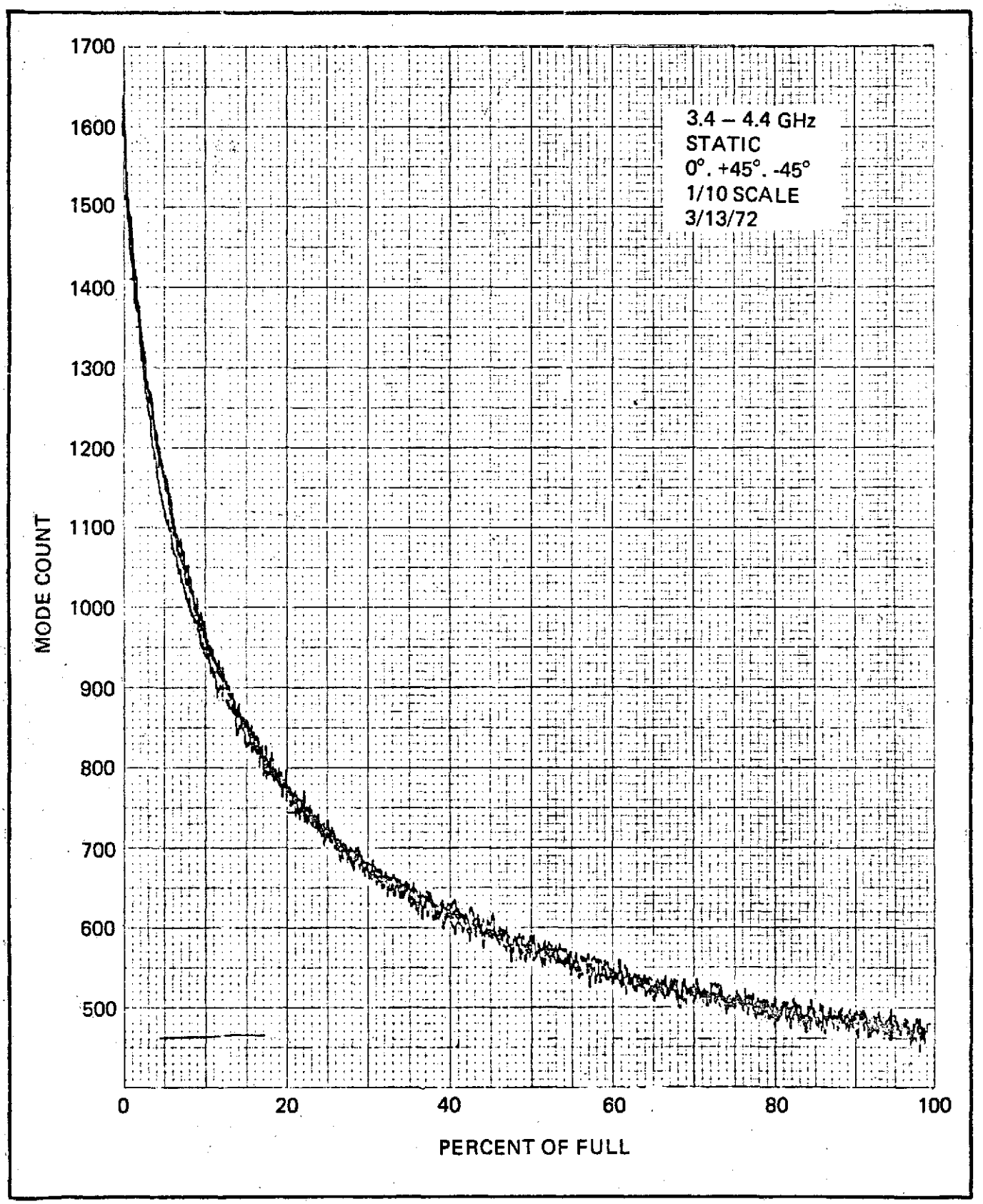
3.4 – 4.4 GHz
STATIC
0°. +45°. -45°
1/10 SCALE
3/13/72
MODE COUNT
1700
1600
1500
1400
1300
1200
1100
1000
900
800
700
600
500
0
20
40
60
80
100
PERCENT OF FULL

Figure A-1

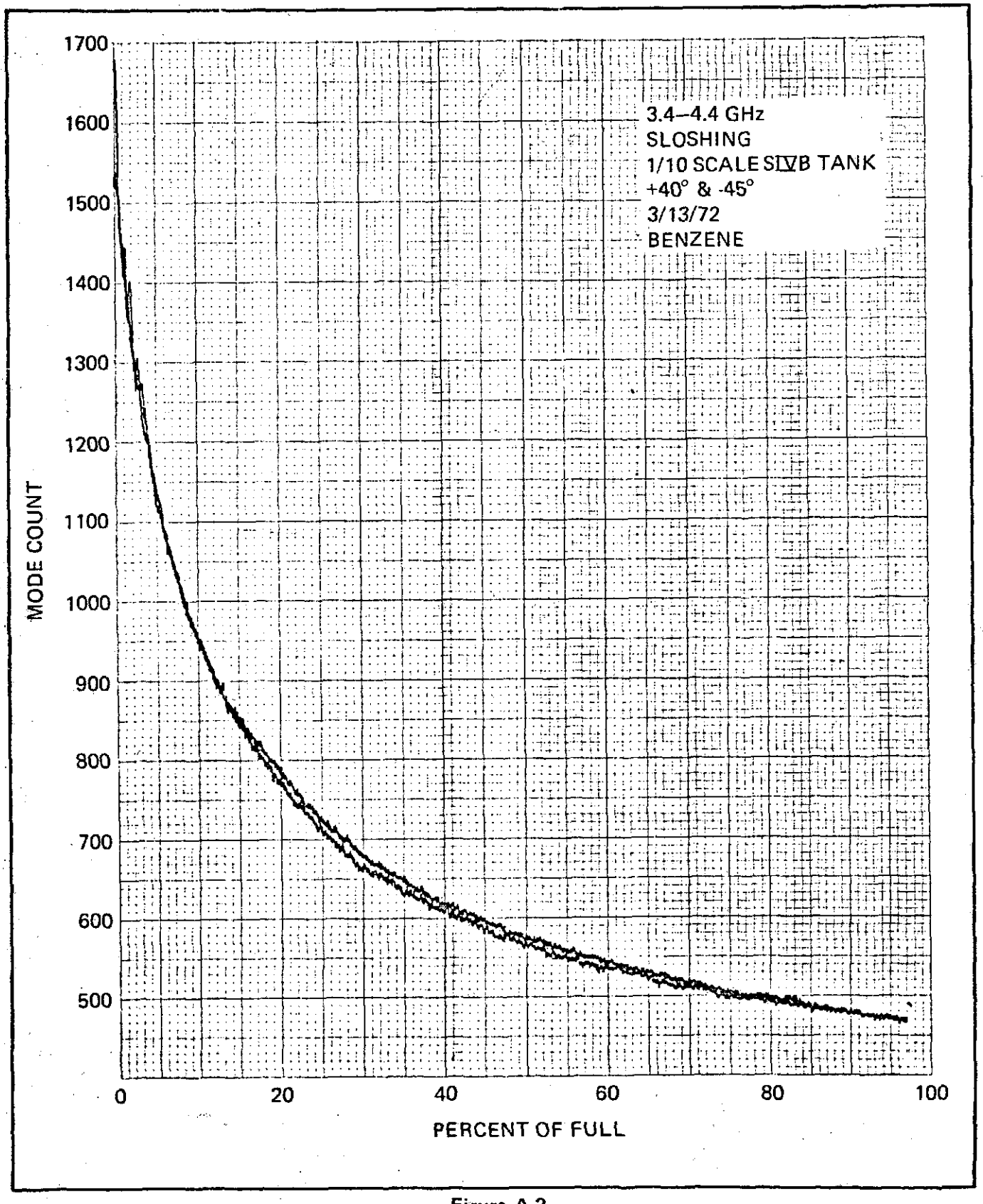
3.4–4.4 GHz
SLOSHING
1/10 SCALE SIVB TANK
+40° & -45°
3/13/72
BENZENE
MODE COUNT
1700
1600
1500
1400
1300
1200
1100
1000
900
800
700
600
500
0
20
40
60
80
100
PERCENT OF FULL

Figure A-2

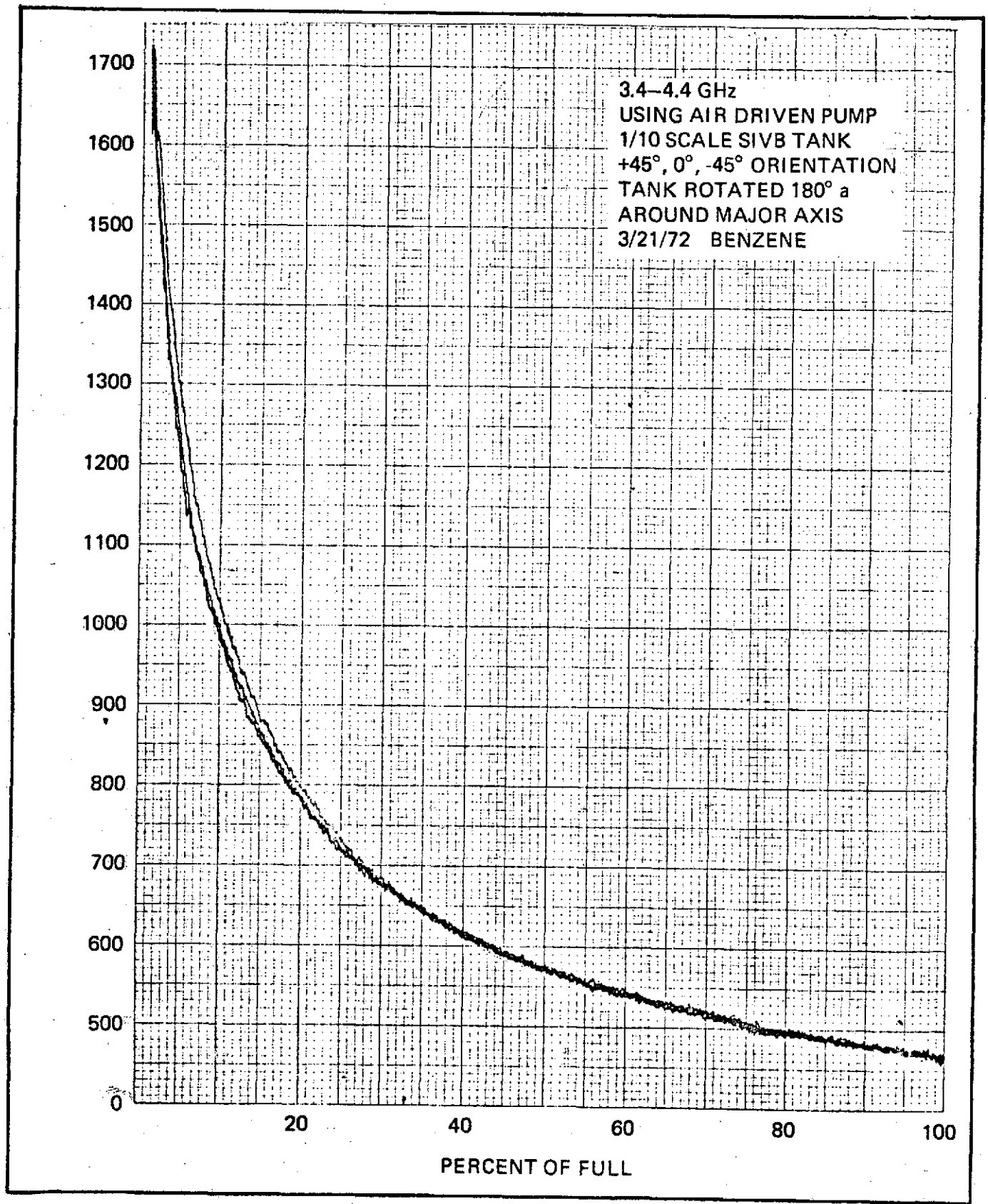
3.4–4.4 GHz
USING AIR DRIVEN PUMP
1/10 SCALE SIVB TANK
+45°, 0°, -45° ORIENTATION
TANK ROTATED 180° a
AROUND MAJOR AXIS
3/21/72 BENZENE
1700
1600
1500
1400
1300
1200
1100
1000
900
800
700
600
500
0
20
40
60
80
100
PERCENT OF FULL

Figure A-3

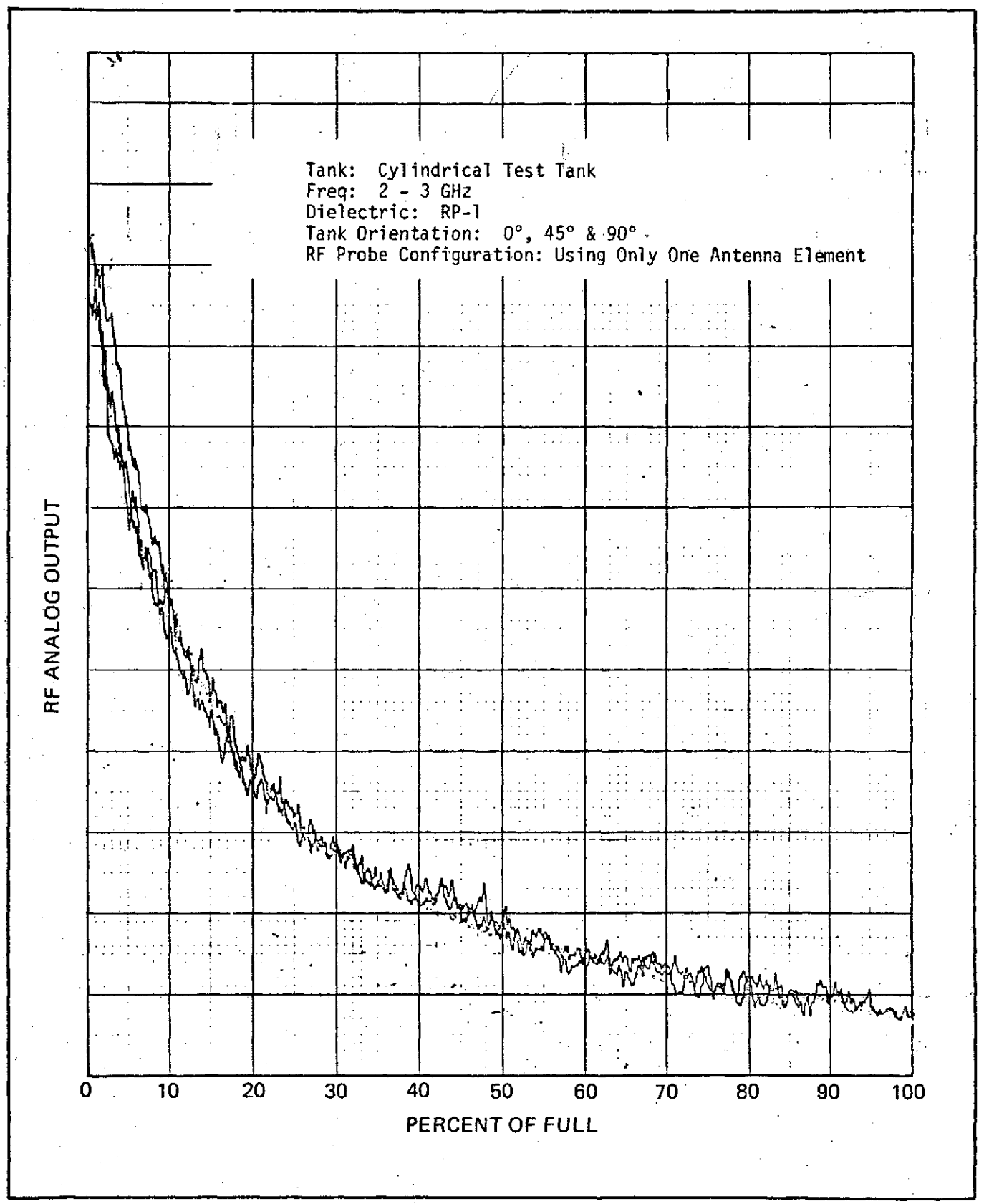
Tank: Cylindrical Test Tank
Freq: 2 - 3 GHz
Dielectric: RP-1
Tank Orientation: 0°, 45° & 90°
RF Probe Configuration: Using Only One Antenna Element
RF ANALOG OUTPUT
0
10
20
30
40
50
60
70
80
90
100
PERCENT OF FULL

Figure A-4

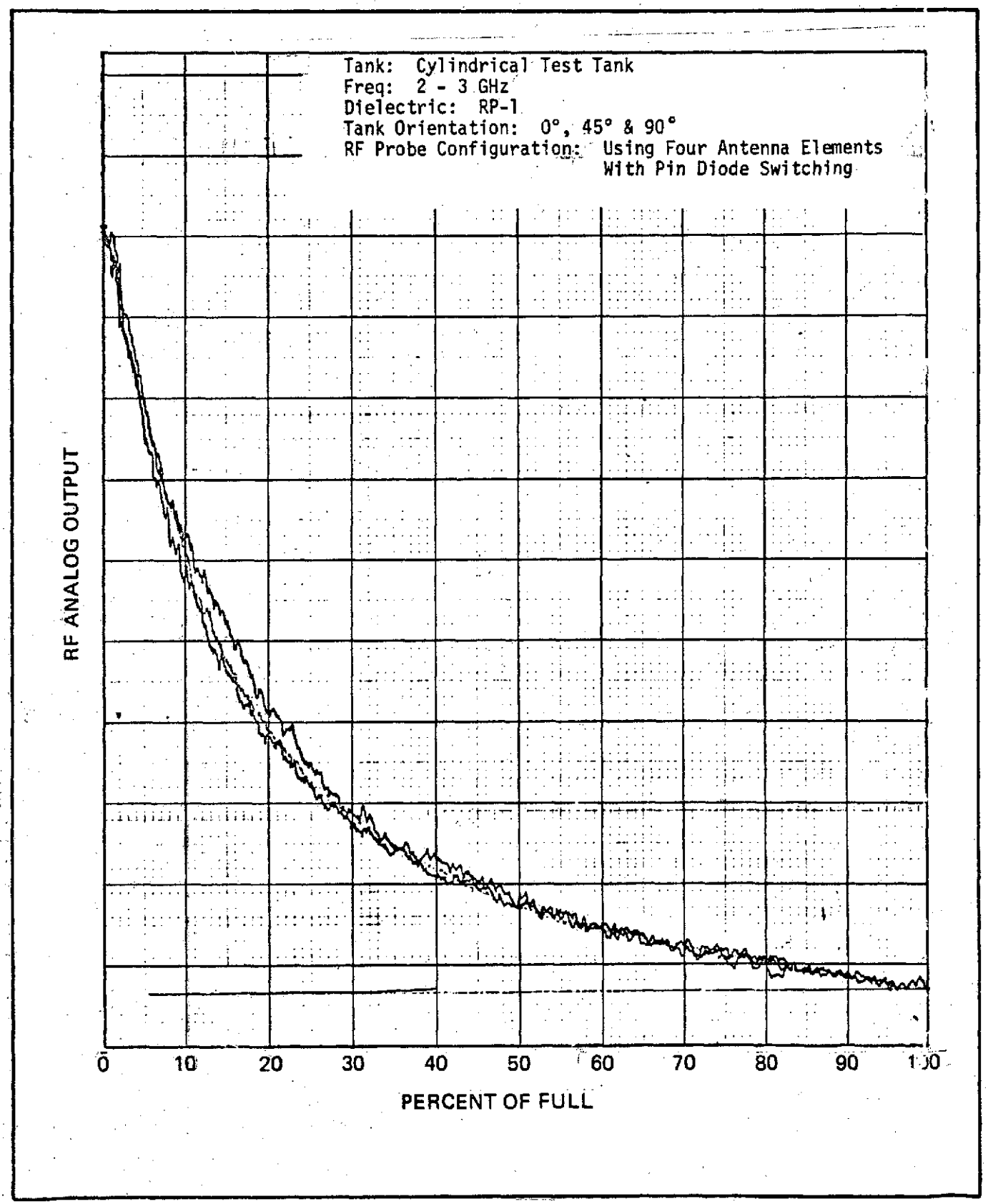
Tank: Cylindrical Test Tank
Freq: 2 - 3 GHz
Dielectric: RP-1
Tank Orientation: 0°, 45° & 90°
RF Probe Configuration: Using Four Antenna Elements With Pin Diode Switching
RF ANALOG OUTPUT
0
10
20
30
40
50
60
70
80
90
100
PERCENT OF FULL

Figure A-5

## REFERENCES


1. Otoshi, T.Y. - "A Study of Microwave Leakage Through Perforated Flat Plates", IEEE Trans. Microwave Theory Tech., pp. 235-236, March 1972

2. Mumford,W.W.- "Some Technical Aspects of Microwave Radiation Hazards", Proc. IRE, vol. 49, pp. 427-447, Feb. 1961

3. Ginzton,E.L. - "Microwave Measurements", pp. 391-434, McGraw-Hill Book Company, 1957